THE PHYSICS OF INTERFACE INTERACTIONS RELATED TO RELIABILITY OF FUTURE ELECTRONICS DEVICES

Thomas H. DiStefano, et al

IBM Thomas J. Watson Research Center

Prepared for:

Defense Advanced Research Projects Agency
Air Force Cambridge Research Laboratories

31 January 1974

AFCRL-TR- 74-0263

THE PHYSICS OF INTERFACE INTERACTIONS RELATED TO RELIABILITY OF FUTURE ELECTRONIC DEVICES

by

Thomas H. DiStefano and King-Ning Tu

IBM Thomas J. Watson Research Center
International Business Machines Corporation
P. O. Box 218
Yorktown Heights, New York 10598

Contract No. F19628-73-C-0006
Project No. 2180

FINAL REPORT

1 August 1973 - 31 January 1974

Contract Monitor: John C. Garth
Solid State Sciences Laboratory

Sponsored by
Defense Advanced Research Projects Agency
ARPA Order No. 2180
Monitored by
AIR FORCE CAMBRIDGE RESEARCH LABORATORIES
AIR FORCE SYSTEMS COMMAND
UNITED STATES AIR FORCE
BEDFORD, MASSACHUSETTS 01730

ARPA Order No. 2180

Program Code No. 2D1

Contractor: IBM Corporation

Effective Date of Contract: 1 August 1972

Contract No. F19628-73-C-0006

Co-Principal Investigator and Phone No.
Dr. Thomas H. DiStefano/914-945-2215
Dr. King-Ning Tu/914-945-1602

AFCRL Project Scientist and Phone No.
Dr. John C. Garth/617 861-4051

Contract Expiration Date: 31 January 1974

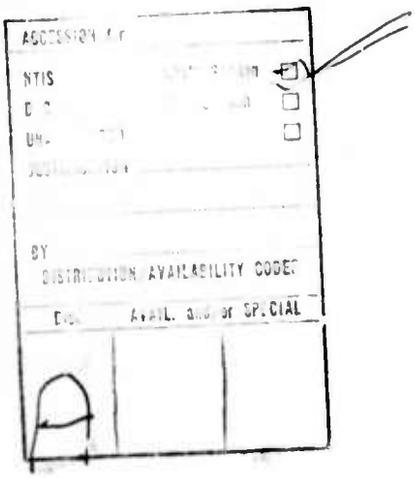

Qualified requestors may obtain additional copies from the Defense Documentation Center. All others should apply to the National Technical Information Service.

//

UNCLASSIFIED

SECURITY CLASSIFICATION OF THIS PAGE *(When Data Entered)*

REPORT DOCUMENTATION PAGE		READ INSTRUCTIONS BEFORE COMPLETING FORM
1. REPORT NUMBER AFCRL-TR-74-0263	2. GOVT ACCESSION NO.	3. RECIPIENT'S CATALOG NUMBER
4. TITLE *(and Subtitle)* THE PHYSICS OF INTERFACE INTERACTIONS RELATED TO RELIABILITY OF FUTURE ELECTRONIC DEVICES		5. TYPE OF REPORT & PERIOD COVERED Final 1 August 1973 31 January 1974 6. PERFORMING ORG. REPORT NUMBER
7. AUTHOR(s) Thomas H. DiStefano King-Ning Tu		8. CONTRACT OR GRANT NUMBER(s) F19628-73-C-0006
9. PERFORMING ORGANIZATION NAME AND ADDRESS IBM Thomas J. Watson Research Center International Business Machines Corporation P. O. Box 218, Yorktown Heights, New York 10598		10. PROGRAM ELEMENT, PROJECT, TASK AREA & WORK UNIT NUMBERS 61101D, 2180 Task & Work Unit n/a
11. CONTROLLING OFFICE NAME AND ADDRESS		12. REPORT DATE 31 January 1974 13. NUMBER OF PAGES 94
14. MONITORING AGENCY NAME & ADDRESS *(if different from Controlling Office)*		15. SECURITY CLASS. *(of this report)* Unclassified 15a. DECLASSIFICATION/DOWNGRADING SCHEDULE

16. DISTRIBUTION STATEMENT *(of this Report)*

A - Approved for public release; distribution unlimited.

17. DISTRIBUTION STATEMENT *(of the abstract entered in Block 20, if different from Report)*

18. SUPPLEMENTARY NOTES

This research was supported by the Defense Advanced Research Projects Agency.

19. KEY WORDS *(Continue on reverse side if necessary and identify by block number)*

Dielectric Breakdown
MNOS
Internal Photoemission
SiO_2
Schottky Barrier
Nb_2O_5 Switching
Interfaces
Insulators
Back Scattering

20. ABSTRACT *(Continue on reverse side if necessary and identify by block number)*

It has been found that a small amount of ionizing radiation will promote dielectric breakdown in a thin film of SiO_2. Essentially, the radiation creates hole-electron pairs which distort the distribution of charge in the insulator. The dependence of breakdown voltage upon photon flux is understood in terms of a simple impact ionization model for dielectric breakdown.

The influence of photon-assisted tunneling upon internal photoemission spectra

DD FORM 1 JAN 73 1473 EDITION OF 1 NOV 65 IS OBSOLETE

UNCLASSIFIED

SECURITY CLASSIFICATION OF THIS PAGE *(When Data Entered)*

was calculated theoretically. This extra tunneling current must be included in an accurate determination of a contact barrier by internal photoemission.

The results of our investigation of the bistable switching behavior in Nb_2O_5 capacitors is summarized, with the finding that the switching is related to structural changes. In essence, switching involves the making and breaking of metallic conductive paths through the grain boundaries of a crystallized region of Nb_2O_5. It appears that neither filament formation nor switching are related to the contact barrier at the metal-Nb_2O_5 interface.

A sensitive technqiue of photoemission spectroscopy has been developed and used to determine the trap distribution at a SiO_2:Si_3N_4 interface. The value of the technique lies in the fact that the surface of a silicon substrate is used as an electrometer to measure total charge trapped in an overlaying insulating layer. For the SiO_2:Si_3N_4 interface, a deep trap, 3.0 eV below the Si_3N_4 conduction band was found to be responsible for charge storage in an MNOS structure. No evidence was found for charge trapping in the shallow traps characteristic of bulk Si_3N_4.

Concerning the instabilities associated with glass-metal reaction, it has been found that Au can induce damaging surface reaction by decomposing SiO_2 in an MOS structure at temperatures as low as 500°C when heated in a dynamic vacuum. The SiO_2 film can be strengthened by an exposure to ion beams, after which the irradiated SiO_2 has shown an improved dielectric breakdown strength.

Contact reactions which result in the formation of silicides have been extended to include the metal Ni. We have found the solid state epitaxial growth of $NiSi_2$ on Si. This is somewhat unusual in that it is an epitaxially grown Schottky barrier.

TABLE OF CONTENTS

- We have measured a radiation induced dielectric breakdown in SiO_2 thin films. A small amount of ionizing radiation, with energy above 9.0 eV, will reduce the dielectric strength of SiO_2 by a large amount, depending upon film thickness. Quantitative results were matched by an extension of our previously reported theory.

- We have summarized our findings on switching in Nb_2O_5 capacitors, showing that the switching is not electronic in nature.[2] Rather, it involves the making and breaking of metallic conductivity paths through in grain boundaries of crystallized regions of the dielectric.

- The deep traps responsible for the memory effect in MNOS transistors have been measured for the first time. The traps are much deeper and more stable than was previously thought. Such deep traps could cause a stability problem in multi-layer dielectrics.

- We predict a problem with processing and bonding of gold metallization on integrated circuits. We have studied structural degradation of $Si:SiO_2:Au$ MOS sandwiches at moderate temperatures (500°C) and have observed an apparent decomposition of the glass film with subsequent migration of Au along the silicon surface. The migration is found to follow the crystallographic direction of the silicon surface.

- We have developed a new technique which may be applied to densify SiO_2 gate insulation and to reduce its pin hole density. The technique is to expose the glass to a low dosage, high energy ion beam. Compaction has been measured by Talystep and confirmed by the changes of density and reflective index obtained by ellipsometry. The densified glass layer has also been found to show an improved dielectric breakdown strength.

- In the area of contact reaction, new information about silicide formation has been obtained. By directly reacting Ni with Si, a sequential formation of Ni_2Si, NiSi and $NiSi_2$ has been observed. The phase $NiSi_2$ is found to grow epitaxially on Si surfaces. We note that the epitaxy is obtained by solid state reaction rather than by the well-known liquid phase or vapor phase epitaxy.

THE PHYSICS OF INTERFACE INTERACTIONS RELATED TO RELIABILITY OF FUTURE ELECTRONIC DEVICES

INTRODUCTION

The overall purpose of our work is the investigation of fundamental phenomena at material interfaces that can directly impact the performance of projected electronic device configurations. We aim to anticipate reliability problems in the newer devices which have not been fully life tested as well as to provide a scientific foundation for understanding reliability problems in present devices. Since the dielectrics involved in interfaces in integrated circuits are limited by practical considerations to SiO_2, Si_3N_4, and Al_2O_3, we are characterizing these materials themselves as well as their interface properties. The major reliability problems can be grouped into several major categories: dielectric breakdown in insulators, interface polarization and shifts in contact barriers, deep traps for charge in insulators, crystallization of insulators, and structural decomposition of interfaces.

We will concentrate on those problems which have proven to be of fundamental scientific importance and which underlie the significant degradation modes that can be foreseen. This provides the best chance for future extension of new device concepts. We anticipate a more concerted theoretical and experimental effort to describe interface polarization effects and contact barrier drift, continued expansion of the theoretical dielectric breakdown model and its implications, description of radiation-induced charge carriers in SiO_2, band structures in insulators, and reaction kinetics at metal-SiO_2 (or Si) interfaces.

I. THE RELIABILITY OF SEMICONDUCTOR-INSULATOR INTERFACES

We have completed a theoretical and experimental investigation of a dielectric breakdown in SiO_2 thin films, including a study of the influence of the adjustable parameters and a study of several important predictions. This is the first quantitative model to describe exactly what occurs during the critical initial stages of dielectric breakdown in the dielectrics used in integrated circuits. The negative resistance type of breakdown is due to a distortion of the electric field caused by positive charge left in the insulator by the small amount of impact ionization produced by hot electrons. Over a range of voltages, the current is multi-valued, with one value of current on the negative resistance instability branch of the curve. We have found experimentally that it is possible to induce a transition from the stable branch to the unstable branch of the curve by irradiating the sample with UV light at above 9.0 eV photon energy. The data from the radiation induced breakdown measurements were fit by calculations based on our impact ionization model for dielectric breakdown. As a result, we are able to estimate a maximum mobility for holes in SiO_2.

Insulator interfaces have been very successfully studied in the past by the technique of internal photoemission. It now appears that considerably more information can be obtained from photoemission than simply the barrier height at an interface contact. In order to lay the framework for new methods of using optical excitation we have formulated theoretically the problem of photon assisted tunneling across a material interface. This phenomenon is predicted to appear in a simple way in the experimental photoemission results. The results of this photon assisted tunneling calculation will be useful in describing forthcoming experimental data.

A. PHOTON INDUCED DIELECTRIC BREAKDOWN IN SiO_2

T. H. DiStefano, P. K. Roy, and M. Shatzkes

The present understanding of dielectric breakdown in insulators is based upon primitive experiments yielding little information other than breakdown voltage and its time, thickness, and temperature dependence. As a result of a lack of data, the concepts involved in understanding dielectric breakdown have evolved little in recent years. Accepted theories[1-3] invoke the energy loss behavior of one statistical electron in the insulator. There is insufficient data to support a more detailed theory of the physical events which occur during the initial critical stages of dielectric breakdown. This paper presents a new technique for obtaining information on the processes involved in breakdown, as applied to the specific case of SiO_2. The influence of an ionizing photon flux on the breakdown voltage and on pre-breakdown current are obtained as a function of radiation intensity. The radiation produces hole-electron pairs at a known rate which perturbs the process of dielectric breakdown. From the dependence upon photon flux, we determine the parameters of an expanded model for dielectric breakdown in SiO_2. From the data, we obtain an estimate for the hole-electron recombination cross section as well as an upper limit on hole mobility in SiO_2.

With the unravelling of the electronic structure of SiO_2,[4-6] particularly the valence band (VB) edge, understanding of the problem of hole transport has become relatively clearer. When SiO_2 is subjected to an ionizing radiation holes are produced in the top nonbonding band, which comprises essentially atomic oxygen orbitals and they can be detected by epr spectroscopy. The low hole mobility (μ_+) resulting from the narrow band width of the top VB is an intrinsic property of SiO_2 and plays an extremely important role in determining the physical processes which occur in the initial stages of a breakdown event.

We summarize the salient features of a simple model, which predicts a reduction of dielectric strength due to ionizing radiation. The model is based on the mechanism of electron injection, impact ionization and electron-hole radiative recombination. Electrons are injected into the insulator by Fowler-Nordheim tunneling at the cathode and scattered to lower energies by electron-phonon scattering. The injected electrons are accelerated by the electric field so that after traversing certain distance, a high energy tail of the electron energy distribution has sufficient energy to ionize the lattice. Electrons above the ionization threshold[6,7] (9 eV above the bottom of the conduction band) are assumed to produce impact ionization with a mean length λ_i. Each impact ionization event leaves behind a low-mobility VB hole.[1] It is assumed the hole moves an insignificant distance before it is annihilated by recombination with another injected electron. Repeated impact ionization will cause the build up of a residual cloud of positive space charge. As a result, the potential is distorted so as to enhance the cathode field leading to impact ionization nearer the cathode, which moves the

centroid of positive charge closer to the cathode. This, in turn, increases the cathode field, leading to a regenerative breakdown process. The holes downstream from the major ionization region are removed by recombination. The critical point at the maximum voltage is the beginning of the negative resistance regime and the onset of a dielectric breakdown instability.

Figure 1 shows schematically the characteristic I-V curve for a relatively thick film of SiO_2 displaying an unstable negative resistance region above the critical current on the knee of the curve. The onset of breakdown will not occur as long as the cathode voltage V is below V_{bd}. However, at this voltage breakdown can be attained if one can go from state 1 to the corresponding state in the negative resistance region at state 2. This can be achieved by the artificial introduction of positive charges by subjecting the SiO_2 to an ionizing radiation above the threshold energy. Holes, being relatively immobile, will induce a field distortion (Fig. 2) resulting in an increase in the injected electron current and a reduction in the breakdown voltage. Therefore, the effect of an ionizing radiation is to reduce drastically the breakdown voltage and can be schematically represented (Fig. 1) by a shifting of the nose of the I-V curve to a lower voltage. We discuss here the first experimental evidence of the dramatic influence of the intensity of monochromatic ionizing radiation (uv light, $\hbar\omega$ = 9.7 eV) on the breakdown strength. Thick SiO_2 samples for self-healing breakdown experiments were grown thermally on (100) n-Si (1 ohm-cm) in dry oxygen atmosphere for 58 hours to attain a thickness of 6920 Å. MOS (Metal-SiO_2-Si) capacitors were prepared by a subsequent deposit of 125 Å semitransparent Au electrode onto the oxide by evaporation.

The experimental configuration is shown schematically in Fig. 3. Throughout the measurements the MOS capacitors were vacuum sealed to a McPhearson-225 type monochrometer capable of generating uv light (0-15 eV) produced by a hydrogen gas glow discharge. The intensity of the uv light (9.7 eV) was varied by opening the entrance slit which was subsequently calibrated against a photocathode for ascertaining the absolute value of the intensity. The voltage was varied by a slowly varying linear ramp circuit (speed = 2 V/sec) built around a programmable power supply (0-1000 V). The current was measured by a Katheley's picoammeter. As the voltage was scanned with the ramp circuit, current spikes were observed when the voltage reached the breakdown value. A typical recorder output of the current-voltage scan at a finite light intensity is shown in Fig. 4, indicating the breakdown voltage by the appearance of a sharp current spike followed immediately by similar successive spikes. The breakdown voltage was taken to be the voltage of the first current spike in a particular scan. Histograms were plotted for these voltages for different scans (typically 15) and the average value was taken to be the breakdown voltage (V_{bd}) for that intensity. For finite light intensity the prebreakdown current occurring at voltages higher than 120 V is due to increased Fowler-Nordheim tunneling (Fig. 1) due to the field distortion (Fig. 2) produced by relatively immobile holes

produced at the top ov VB by impact ionization. Experimental scatter in the breakdown voltage was within $\pm$ 5 V. Figure 5 shows the dependence of the breakdown voltage as a function of the light intensity. Results show a dramatic reduction of the breakdown voltage from 590 V to about 300 V as the relative intensity of light is changed from 0 to 0.2, this followed by an asymtotic decrease to 255 V when the intensity reaches its maximum normalized value of 1.

The experimental functional dependence of the breakdown voltage with light intensity matches very well with the theoretical predictions in a simple model for dielectric breakdown.[8] The key parameter λ being the one dimensional projection of the phonon scattering length. The electron scattering events are assumed to be a Poisson process, and to involve the loss of one LO-phonon per collision (0.153 eV) which is assumed to be predominantly a forward scattering event. The probability that an electron will suffer n collisions in traversing a distance x is,

$$P(n,x) = \frac{1}{n!}\left(\frac{x}{\lambda}\right)^{n} e^{-x/\lambda}. \tag{1}$$

A discrete energy distribution curve at point x is obtained by allowing the electron to lose one phonon or $\hbar\omega$ in each collision. At x, the probability P is a function of the energy E,

$$P(x,E) = \frac{1}{(-E/\hbar\omega)!}\left(\frac{x}{\lambda}\right)^{-E/\hbar\omega} e^{-(x/\lambda)}, \tag{2}$$

or, by the central limit theorem, the energy distribution is

$$D(x,E) \simeq \frac{(1/\hbar\omega)}{\sqrt{2\pi(x/\lambda)}}\, e^{-\frac{(E/\hbar\omega + x/\lambda)^2}{2(x/\lambda)}} \tag{3}$$

where E is the electron energy with respect to the initial energy.

For the case in which an electron ionizes the lattice as soon as it attains an energy of E_g above the conduction band edge, the rate of impact ionization or production of positive charge is,

$$\dot{\rho}\Big|_{+_i} = J\,\frac{d}{dx}\int_{\phi(x)+E_g}^{\infty} D(x,E)\,dE. \tag{4}$$

where $\phi(x)$ is the field potential at x, and J is the initial Fowler-Nordheim current density.

The rate of positive charge production at the top of VB by uv light is given by:

$$\dot{\rho}_+\Big|_L = \frac{I}{\delta}\, e^{\frac{-(d-x)}{\delta}} \qquad (5)$$

where I = light intensity, δ = (attenuation length taken to be 350 Å) and d = thickness of SiO_2 film (6920 Å). The rate of annihilation of positive charge by recombination is given by:

$$\dot{\rho}_+\Big|_r = \frac{J_\rho}{e} + \int_{\phi(x)}^{0} \sigma(E)\, D(X,E)\, dE \qquad (6)$$

where σ (E) is the energy dependent recombination cross section and ρ_+ is the hole charge density.

In the steady state condition, the rate of production of holes by impact ionization and uv light is equal to that of annihilation by recombination.

$$\dot{\rho}_+\Big|_i + \dot{\rho}_+\Big|_L = \dot{\rho}_+\Big|_r . \qquad (7)$$

The functional dependence of the breakdown voltage on light intensity in our model and the current-voltage characteristic were calculated for a 6920 Å film of SiO_2. The best match with experiment was obtained for λ = 1.34 Å, $\sigma(E) = 10^{-24}$ cm^2, and $J_\rho = 38.86 \times 10^{-4}$ Amp/cm^2. The set value 1.34 Å for the one dimensional projection of electron-phonon scattering length λ determines V_{bd} for I = 0. Results of the calculation are shown in Figs 5 and 6. For intensities higher than 0.2, the asymtotic shape and the lower limit of the V_{bd} is controlled by σ(E) and only weakly by λ. Figure 6 gives the physical picture of our model as the light intensity is changed from 0 to 1. The increase in the initial portion of the J-V characteristic curves is due to the increased cathode field and the resulting Fowler-Nordheim tunneling current. The initial dramatic reduction in V_{bd} (0 < I < 0.2) is caused by the same reason, namely the accummulation of the relatively immobile holes at the top of VB causing the field distortion, more electron current injection and a reduction in the voltage necessary to attain the unstable negative resistance region. The pre-breakdown current for a particular light intensity was estimated from Fig. 6 by substracting the Fowler-Nordheim tunneling current for I = 0 with the corresponding current for that intensity. Theoretical results matches very well the prebreak currents

as observed experimentally for finite light intensities as shown in Fig. 4. An estimate of the hole mobility (μ_e+) was made from our experimental results by equating the maximum life time of the holes (t_e+) to the transit time through 6920 Å SiO_2 (t_e). The upper limit of μ_e+ was found to be 8.25×10^{-14} $cm^2/V\text{-sec}$. This relatively low μ_e+ may be expected since the width of the top VB is about 1 eV, which is narrow enough to cause Anderson localization in a lattice with imperfections and defects.

References

1. Fröhlich, H.; Proc. Roy. Soc. A160, 230 (1937).
   A178, 493 (1942).
   A188, 521 (1947).

2. Seitz, F., Phys. Rev. 76, 1376 (1949).

3. Von Hippel, A.; J. Appl. Phys. 8, 815 (1937).
   Phys. Rev. 54, 1096 (1938).

   Von Hippel, A. and Alger, R. S., Phys. Rev. 76, 127 (1949).

4. DiStefano, T. H. and Eastman, D. E., Phys. Rev. Letters 27, 1560 (1971).

5. Fischer, W., "Chemical Bonding and Valence State - Non-Metals" (in Advances in X-ray Analysis, Vol. 13, ed. by B. L. Henke, J. B. Newkirk, and G. R. Mallett, Plenum Press, 1970) p 159.

   D. J. Nagel, "Interpretation of Valence Band X-ray Spectra" ibid. p. 182.

6. T H. DiStefano and D. E. Eastman, Solid State Comm. 9, 2259 (1971).

7. T. H. DiStefano and P. K. Roy, Optical Properties of Allotropic Forms of SiO_2, 2nd Semi-Annual Technical Reprot, ARPA Contract No. F19628-73-C-0006.

8. T. H. DiStefano and M. Shatzkes, Impact Ionization Model for Dielectric Instability and Breakdown, 2nd Semi-Annual Technical Report, ARPA Contract No. F 19628-73-C-0006.

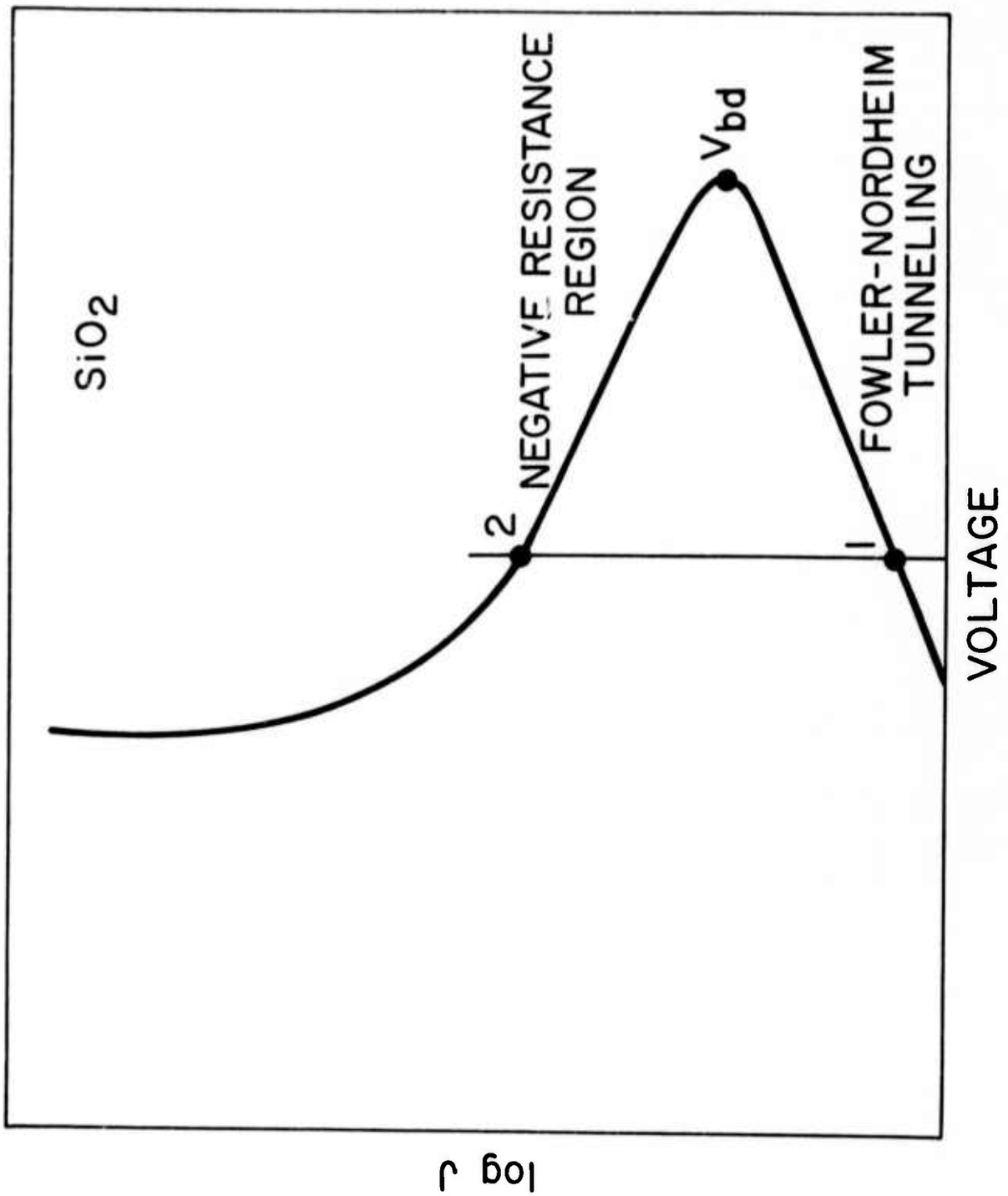

Figure 1: A typical current density vs applied voltage characteristic for a thick SiO_2 film. The negative resistance instability begins at the critical point V_{bd} on the knee of the curve. The Fowler-Nordheim tunneling region occurs at voltages below V_{bd}. At an applied voltage shown by the line, two states of the system are possible. State 1 corresponds to the steady state solution with no significant positive charge layer. State 2, which occurs at the same voltage as state 1, is in the negative resistance breakdown regime, in which a positive charge layer is found near the cathode.

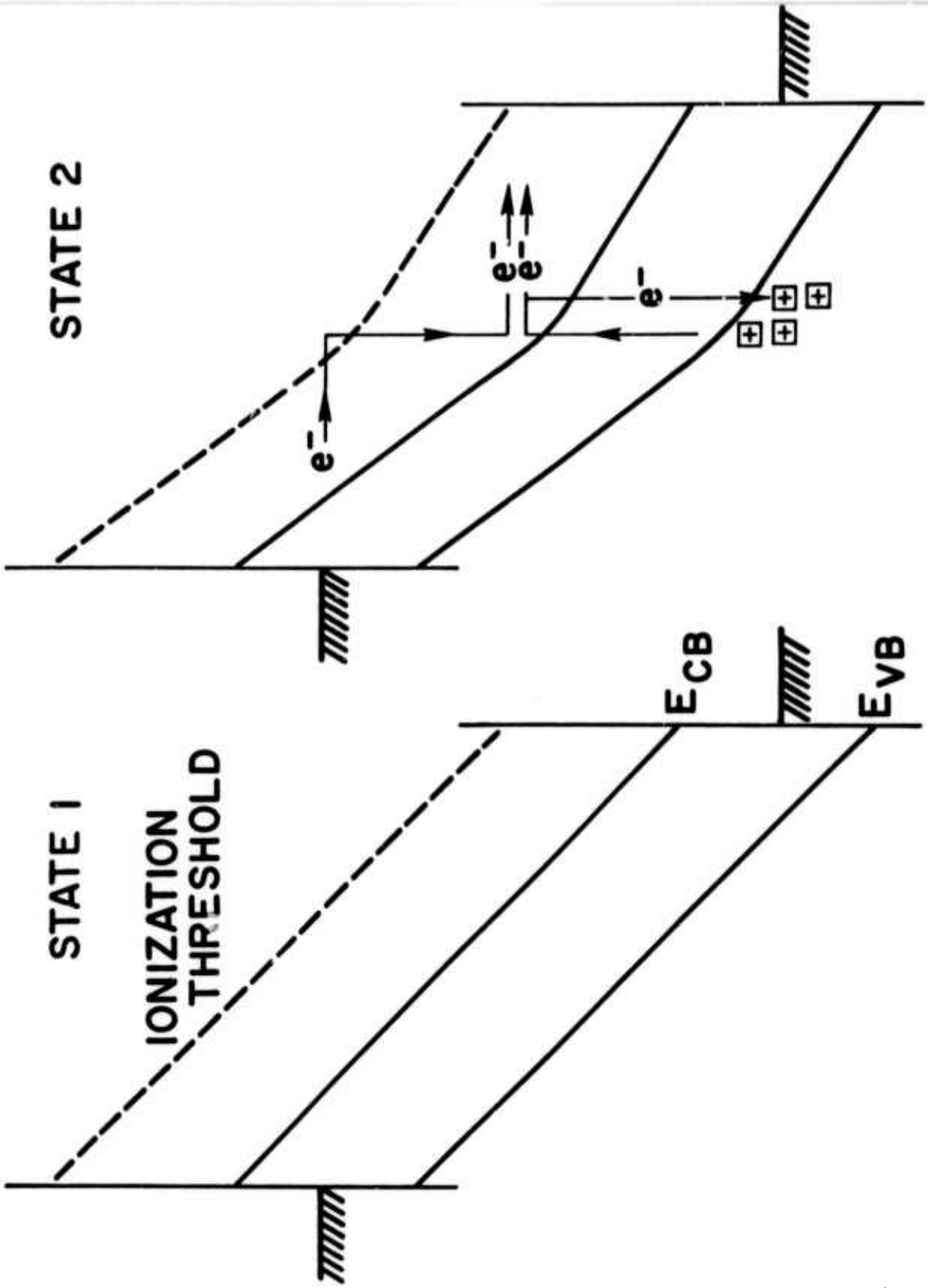

Figure 2: Schematic representation of states 1 and 2, State 1 has no significant positive charge layer. A positive space charge layer appears near the cathode orbital of the VB induces a field distortion (state 2) which leads to more electron injection, impact ionization and a runaway breakdown.

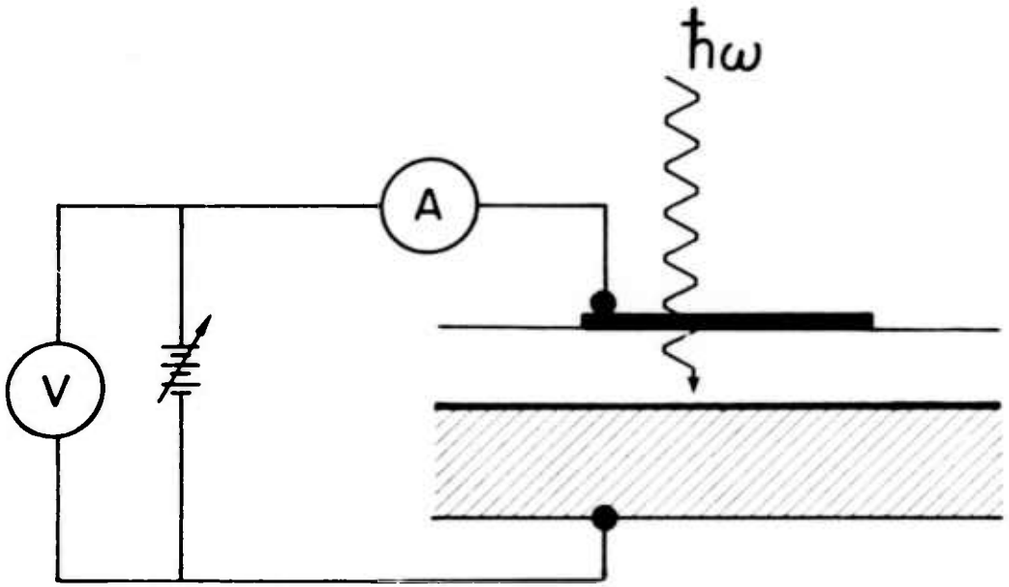

Figure 3: Radiation induced breakdown experimental set up. The voltage ramp circuit is a kepco programmable power supply, Rate = 1.6 V/sec. The current is measured by a Katheley's picoammeter. The sample is (100) n-type Si onto which 6920 Å SiO_2 is thermally grown, followed by a subsequent deposit of a 125 Å semitransparent Au electrode. The radiation is $\hbar\omega$ = 9.7 eV light.

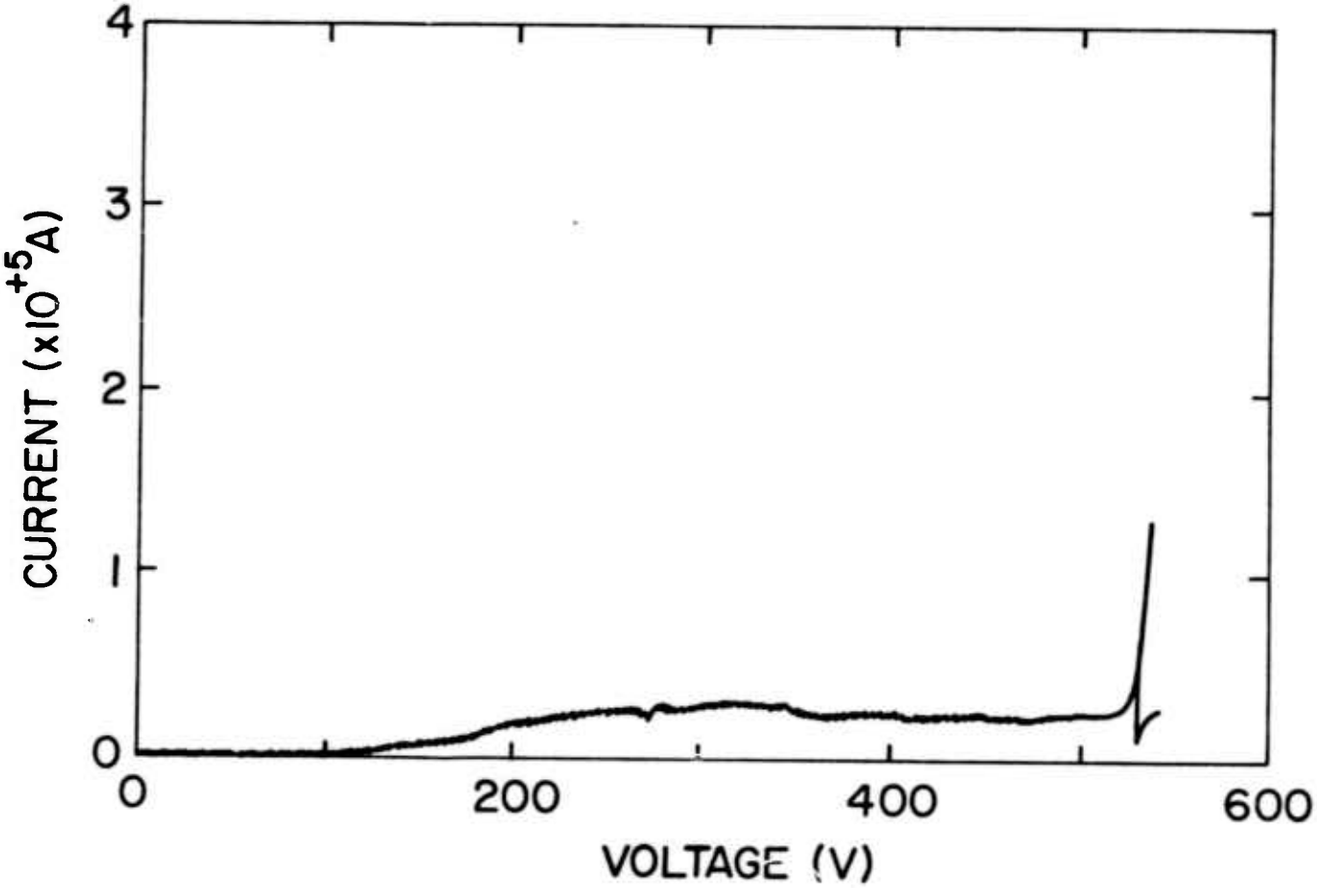

Figure 4: The current density - ramp voltage characteristic for finite light intensity indicating the breakdown current above 120 V followed by a sharp spike at the breakdown voltage.

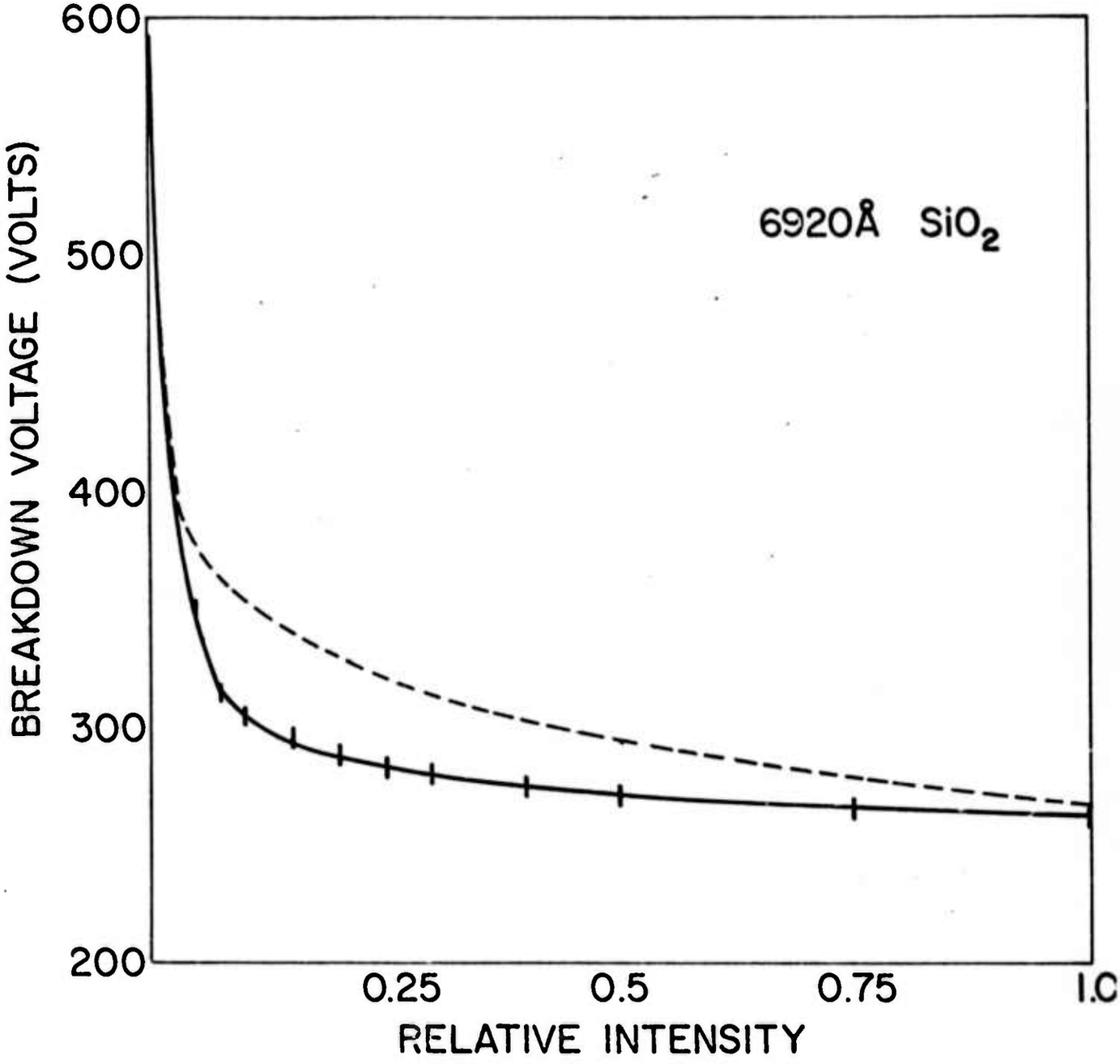
600
500
400
300
200
BREAKDOWN VOLTAGE (VOLTS)
6920Å SiO2
0.25
0.5
0.75
1.0
RELATIVE INTENSITY

Fig. 5

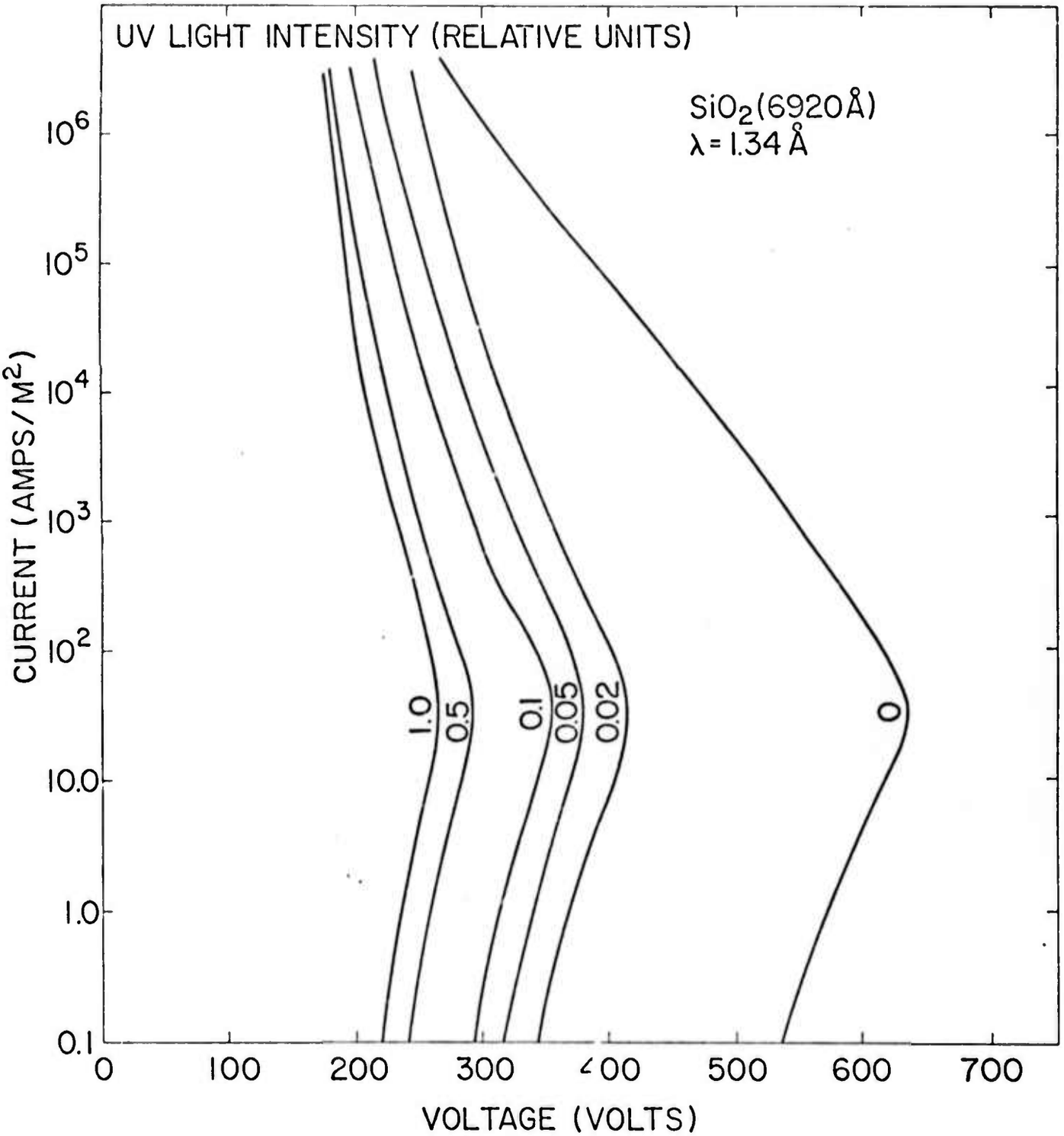

Figure 6: The current-voltage characteristic for 6920 Å SiO_2 for different light intensities using the energy dependent recombination cross section, $\sigma(E) = 0.01$ that of Milne and the one dimensional projection of the electron-phonon scattering length, $\lambda = 1.34$ Å. The Fowler-Nordheim tunneling regime, the critical point on the knee, V_{bd} and the negative resistance region is shown along with the drastic initial reduction in V_{bd} followed by a gradual decrease as the light intensity is varied from 0 to 1.

B. PHOTON ASSISTED TUNNELING IN INTERNAL PHOTOEMISSION
I. THEORY

C. G. Wang and T. H. DiStefano

The photoelectric emission from the surface of a conductor can be well understood on the basis of the Fermi-Dirac distribution for a free electron gas in a metal and the classical image force barrier at the surface. The dependence of an applied field arises in the lowering of the barrier by the square root of the applied field, and by including the tunneling through the potential barrier Fowler and Nordheim carried out their analysis in the late nineteen twenties. The historical developements and a comprehensive mathematical presentation of this subject, up to 1956, can be found in an article by Good and Müller in the Hand Book der Physik.[1]

Recent interest in interface physics in terms of band bending (Inkson) and carrier injection has led to renewed efforts to use internal photoemission as a tool to measure the work functions, the carrier transport properties, and the transport properties at the interfaces between metal and insulator or metal and semiconductor, and to study the energy band relationship at the interfaces. It can also be used to measure the impurity concentrations or surface contamination. The current work is to present the basic theoretical analysis of photoemission from a unified point of view, with photon assisted tunneling in particular, and to derive algebric relationships which would be necessary for understanding of experimental results.

We shall consider photon assisted field emission from metal into insulator in the limit of low temperature and assume that electrons are in a simple conduction band with a simple effective mass m*, and that the photoemission is independent of depth as well as it has a constant yield. The photon energy $\hbar\omega$ raises the electron energies from those at the Fermi energy E_F and lower, so for simplicity of notation, the variable quantity $\hbar\omega$ is absorbed into E_F, and we shall not carry along $\hbar\omega$ in our algebra.

Following Fig. 1, the photoassisted field emission current I is a product of two functions-n, the supply function, and D, the transmission coefficient. Consider first the tunneling current I_t,

$$I_t = \alpha_o e \int_{-\infty}^{-e\Delta\phi} n(E)\, D(E)\, dE \quad , \qquad (1)$$

where α_o is the photoefficiency and E is the electron energy. E is always negative as the zero is taken at the threshold. In the usual WKB approximations with small probability of penetration,

$$D(E) = e^{-\int_{x_1}^{x_2} \sqrt{\frac{8m^*}{h^2}(V(x)-E)}\, dx} \quad , \qquad (2)$$

where m* is the effective electron mass, h the Planck's constant, V(x) the potential; $V(x>o) = -eFx - e^2/4x$, F the effective applied field which includes the electrostatic relaxation by dielectric constant ϵ, and

$$\left.\begin{matrix} x_1 \\ x_2 \end{matrix}\right\} = \frac{|E|}{2eF}\left(1 \mp \sqrt{1 - e^3F/E^2}\right)$$; they are the branch points of the tunneling electron.

D(E) has a solution[1]

$$D(E) = e^{-\frac{4\sqrt{2m^*|E|^3}}{3\hbar eF} v(y)} \quad , \qquad (3)$$

where

$$y = e\Delta\phi_{max}/|E| = \sqrt{e^3F}/|E| \quad , \quad \text{and}$$

$$v(y) = 2^{-\frac{1}{2}}\sqrt{1+\sqrt{1-y^2}}\left[L_1(k) - (1-\sqrt{1-y^2})L_2(k)\right]$$

with

$$k^2 = 2\sqrt{1-y^2}/(1+\sqrt{1-y^2}) \quad , \quad \text{and}$$

$$L_1(k) = \int_0^{\pi/2}\sqrt{1-k^2\sin^2\varphi}\, d\varphi \quad ,$$

$$L_2(k) = \int_0^{\pi/2}\frac{d\varphi}{\sqrt{1-k^2\sin^2\varphi}} \quad .$$

As $y = e\Delta\phi_{max}/|E| \leq 1.0$, and due to the exponential decrease of D for small y, we may limit the range of interest of y at $0.6 \leq y \leq 1$ where $v(y) \approx 1.5\,(1-y)$. From (3),

we have $$D(E) = e^{-\frac{2\sqrt{2m^*|E|}}{\hbar\Delta\phi^2}(|E| - e\Delta\phi)} \equiv e^{-2d} \quad . \qquad (4)$$

Note that for large penetration D, from conservation of current flux, we should have instead

$$D(E) = \frac{e^{-2d}}{1+e^{-2d}} = \frac{1}{1+e^{2d}} \simeq (1-e^{-2d})\, e^{-2d} \quad . \qquad (5)$$

Equation (5) can be considered as the usual WKB approximation of e^{-2d} coupled with a small correction to the preexponential factor $(1-e^{-2d})$. We can treat $(1-e^{-2d}) \simeq 1$ for most cases. The supply function n(E) can be derived from the Fermi-Dirac statistics,[1]

$$n(E)dE = \frac{4\pi m^* kT}{h^3} \ln\left(1 + e^{\frac{E_f - E}{kT}}\right) dE$$

$$\simeq \frac{4\pi m^*}{h^3} (E_f - E)\, dE \quad \text{for } T = 0 \quad . \qquad (6)$$

From (4) and (6), Equation (1) becomes

$$I_t(E) = \frac{4\pi m^* e\, \alpha_0}{h^3} \int_{-\infty}^{-e\Delta\phi} e^{\frac{-2\sqrt{2m^*|E|}}{\hbar eF}(|E| - e\Delta\phi)} (E_f - E)\, dE \quad .$$

A change of variable $\delta \equiv |E| - e\Delta\phi$, and let $I_0 = \frac{4\pi m^* e}{h^3}$,

we have

$$I_t(E) = \alpha_0 I_0 \int_0^{\infty} e^{-\frac{\sqrt{8m^*|E|}}{\hbar eF}\delta} \left[E_f - e\Delta\phi + \delta\right] d\delta$$

$$= \alpha_0 I_0 \left[(E_f - e\Delta\phi) \int_0^{\infty} e^{-\frac{\sqrt{8m^*(e\Delta\phi + \delta)}}{\hbar eF}\delta} d\delta + \int_0^{\infty} e^{-\frac{\sqrt{8m^*(e\Delta\phi+\delta)}}{\hbar eF}\delta} \delta\, d\delta \right.$$

expanding to second order,

$$I_t(E) = \alpha_0 I_0 \left[(E_F - e\phi) \int_0^\infty e^{-\frac{2\sqrt{2m^*}}{\hbar e F}\left(\sqrt{e\phi}\,\delta + \frac{\delta^2}{2\sqrt{e\phi}}\right)} d\delta \right.$$

$$\left. + \int_0^\infty e^{-\frac{2\sqrt{2m^*}}{\hbar e F}\left(\sqrt{e\phi}\,\delta + \delta^2/2\sqrt{e\phi}\right)} \delta\, d\delta \right]$$

$$= \alpha_0 I_0 \left[(E_F - e\phi) \int_\alpha^\infty e^{-(\alpha+\beta\delta)^2} \frac{e^{\alpha^2}}{\beta} d(\alpha+\beta\delta) \right.$$

$$\left. + \int_\alpha^\infty e^{-(\alpha+\beta\delta)^2} \frac{e^{\alpha^2}}{\beta} \xi\, d(\alpha+\beta\delta) \right] ,$$

where $\alpha = \sqrt{\frac{2m^* e\phi}{\hbar e F}} \sqrt[4]{\frac{e\phi}{2m^*}} = \left(\frac{3.43\times10^9}{F}\right)^{\frac{1}{8}}$, with $m^* = 0.41\, m_e$ for SiO_2 and F in volts/cm ϵ ,

and

$$\beta = \alpha/e\phi = \alpha'(3.79\times10^{-4} F^{\frac{1}{2}}) .$$

After some algebric manipulation, the integral becomes

$$I_t(E) = \alpha_0 I_0 \frac{e^{\alpha^2}\sqrt{\pi}}{2\beta} \left\{ (E_F - e\phi)(1 - \mathrm{erf}(\alpha)) + \frac{e^{-\alpha^2}}{\beta\sqrt{\pi}} - \frac{\alpha}{\beta}\left[1 - \mathrm{erf}(\alpha)\right] \right\}$$

$$= \alpha_0 I_0 \left\{ \frac{(E_F - e\phi)\sqrt{\pi}\, e\phi}{2\alpha^2} \alpha e^{\alpha^2} \mathrm{erfc}(\alpha) + \frac{(e\phi)^2}{2\alpha^2} - \frac{\sqrt{\pi}(e\phi)^2}{2\alpha^2} \alpha e^{\alpha^2} \mathrm{erfc}(\alpha) \right\}$$

$$= \alpha_0 I_0 \frac{e\phi}{2\alpha^2} \left\{ (E_F - e\phi)\sqrt{\pi}\, g(\alpha) + e\phi \left[1 - \sqrt{\pi}\, g(\alpha)\right] \right\} ,$$

(7)

where erf(α) is the error function with argument α, erfc(α) = 1 - erf(α), and $g(\alpha) = \alpha e^{\alpha^2} \cdot \mathrm{erfc}(\alpha)$ is the complementary error function of the order one-half over a large range of the effective applied field F (Fig. II) $\sqrt{\pi}\, g(\alpha)$ is of the order unity and $(1-\sqrt{\pi}\, g(\alpha))$ is a small correction at a constant applied field.

For dimensional considerations, the yield for the well known Schottky lowering of the barrier is $I_s = \alpha_o I_o (E_F - e\Delta\phi)^2$, where again the variable $\hbar\omega$ is included in the Fermi energy E_F, and the yield for the tunneling of the barrier is $I_t = \alpha_o I_o [A(E_F - e\Delta\phi) + B]$ where $A = e\Delta\phi\sqrt{\pi}\, g(\alpha)/2\alpha^2$ and $B = (e\Delta\phi)^2[1-\sqrt{\pi}\, g(\alpha)]/2\alpha^2$. Combining the two yields,

$$I = I_s + I_t = \alpha_o I_o \left[(E_F - e\Delta\phi)^2 + A(E_F - e\Delta\phi) + B \right] \qquad (8)$$
$$= \alpha_o I_o \left[\left(E_F - e\Delta\phi + \frac{A}{2}\right)^2 + B - A^2/4 \right] .$$

Thus, the Schottky yield is effectively shifted in the yield plot by photon assisted tunneling by an amount A/2 and by $(B-A^2/4)$ at a constant applied field F. Figure III illustrates the separate contribution of I_s and I_t on the photoyield . Note that by holding photon energy constant, the decrease in photothreshold energy $\alpha F^{1/2}$ for I_s, but $\alpha F^{5/4}$ for I_t. I_t has a stronger dependence on the applied field F than that of the dipole layer model αF, as suggested by Mead et al.[3]

Having considered I_t as a correction to I_s, the quantum mechanical reflection I_R for the energies above the threshold energy should also be treated on the same basis as that of I_t. However, due to the small range of the limits of integration of the supply function, the resultant I_R is much smaller than I_t and may be neglected.[4]

The thermal spread of the supply function in Eq. (6) may be considered as a separate correction as long as the thermal energy is much smaller than the work function. With unity for transmission coefficiency, the current is then

$$I_{th} = \alpha_o e \int_{e\phi}^{\infty} \frac{4\pi m^* kT}{h^3} \ln\left(1 + e^{\frac{E_F - E}{kT}}\right) dE = \alpha_o I_o (kT)^2 f(x) ,$$

where $x = \exp\left(\frac{E_F - e\Delta\phi}{kT}\right)$ and f(x) is the well known Fowler function. This correction can be checked by the usual Fowler plot of the $\ln I_{th}/(kT)^2$

vs $\frac{E_F - e\Delta\phi}{kT}$ which gives rise to a thermal tail of the order of 4 kT .

References

1. R. H. Good, Jr. and Erwin W. Müller, Field Emission, Hand Book der Physik 21, 176 (1956).

2. M. Abramowitz and I. A. Stegun, editors, Handbook of Mathematical Functions, National Bureau of Standards.

3. C. A. Mead, E. H. Snow, and B. E. Deal, Barrier Lowering and Field Penetration at Metal-Dielectric Interfaces, Appl. Phys. Letters 9, 53 (1966).

4. E. L. Murphy and R. H. Good, Jr., Thermionic Emission, Filed Emission, and the Transition Region, Phys. Rev. 102, 1464 (1956).

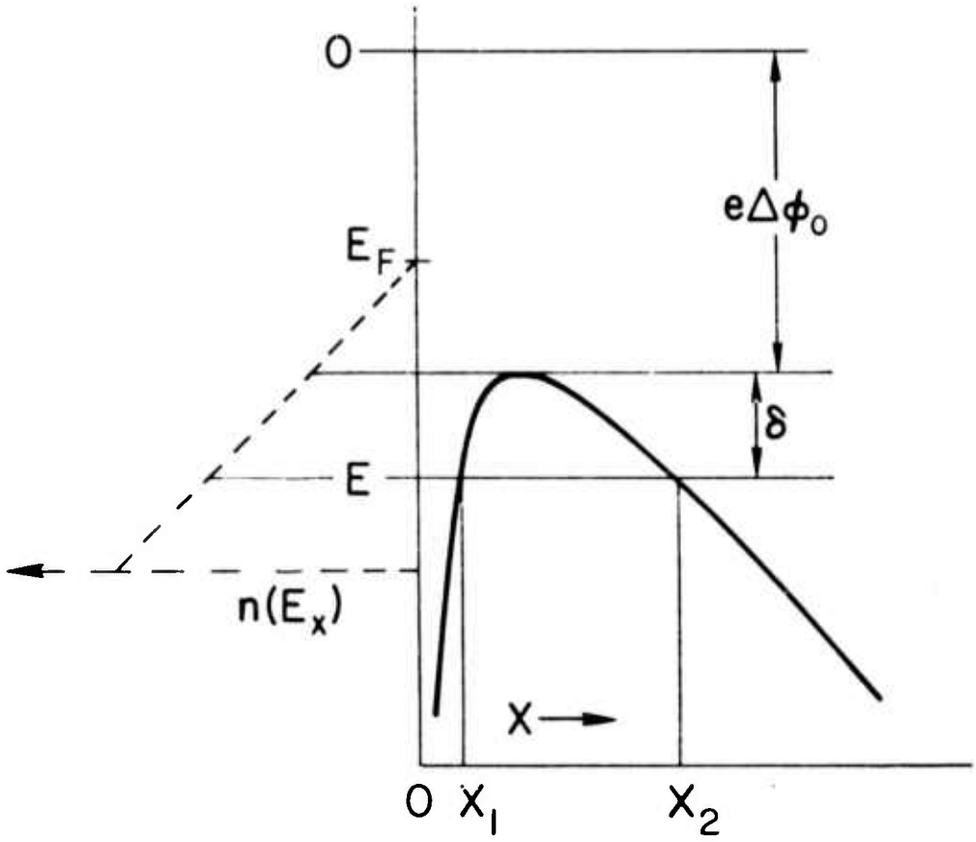

Figure 1: SCHOTTKY POTENTIAL BARRIER
Conductor surface begins with x=o, x_1 and x_2 are the points of zero momentum for electrons with transverse kinetic energy ε. $e\Delta\phi$ in Schottky barrier. $n(\varepsilon_+)$ is the electron distribution function, with a triangular shape for the transverse component alone.

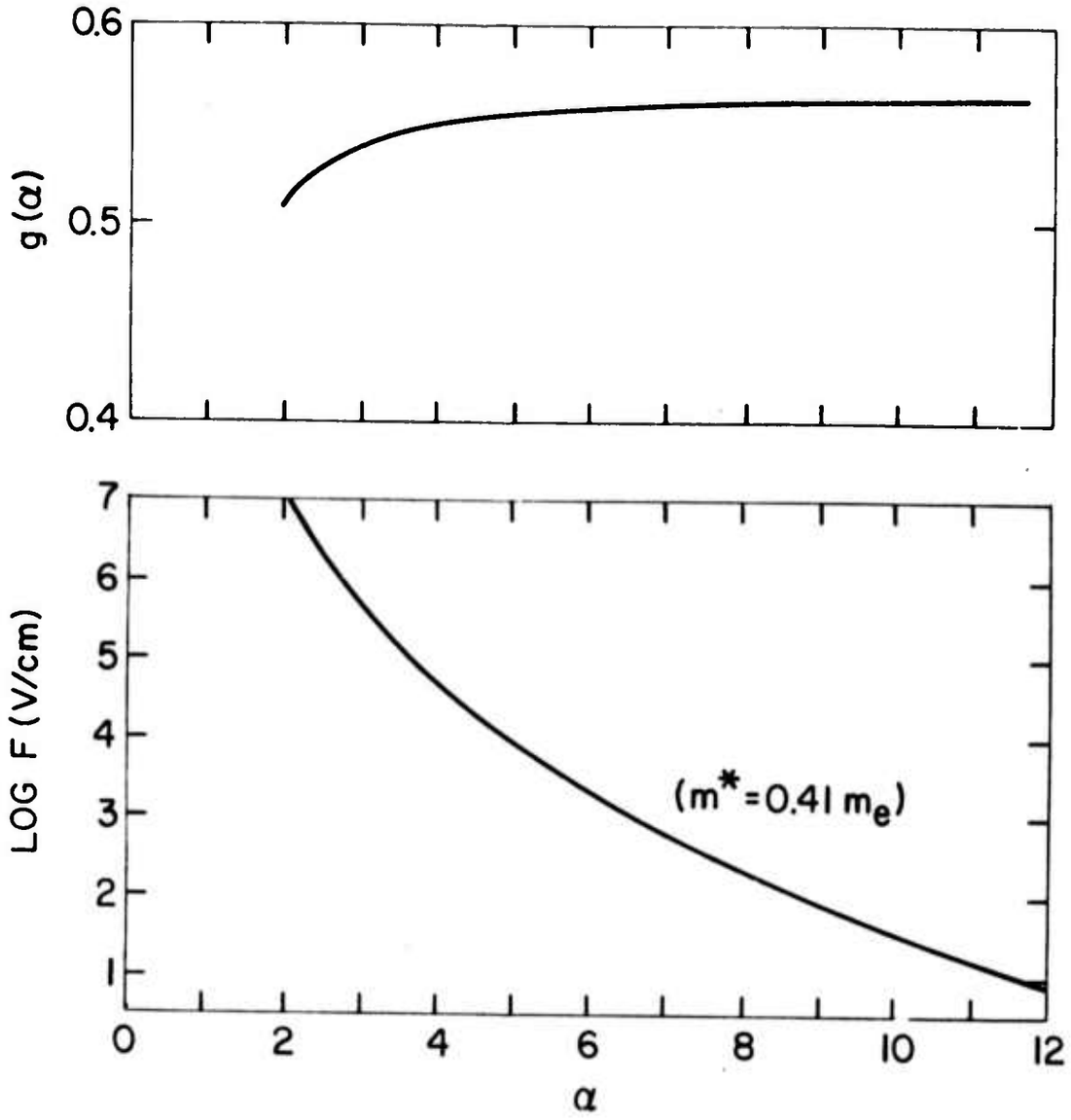

Figure 2: COMPLEMENTARY ERROR FUNCTION g(α)
The function g(α) is not sensitive to the applied field F.

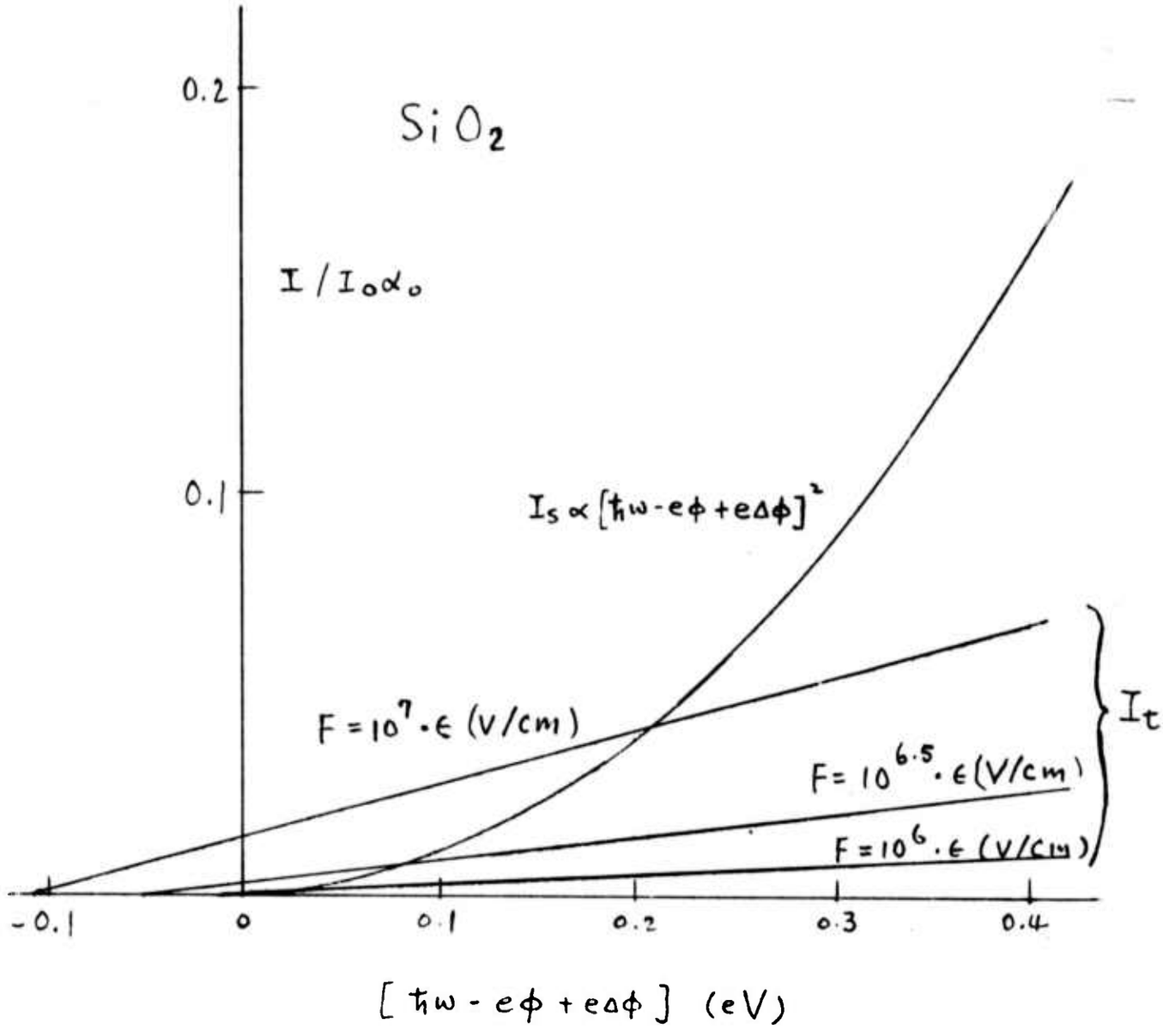
0.2
SiO_2
$I / I_o \alpha_o$
0.1
$I_s \propto [\hbar\omega - e\phi + e\Delta\phi]^2$
$F = 10^7 \cdot \epsilon$ (V/cm)
$F = 10^{6.5} \cdot \epsilon$ (V/cm)
$F = 10^6 \cdot \epsilon$ (V/cm)
I_t
-0.1
0
0.1
0.2
0.3
0.4
$[\hbar\omega - e\phi + e\Delta\phi]$ (eV)

Fig. III

II. BAND STRUCTURE AND SWITCHING IN METAL OXIDE INSULATORS

We present a summary of our results relating to structural, electronic, and photoemission properties of Nb_2O_5 thin films. These films are interesting because of the relatively fast bistable switching found in capacitors made with low melting point electrodes. A capacitor of Nb_2O_5 can be made to switch between two different resistance states by the application of voltage pulses of the proper sign and magnitude, where switching takes place in a filament formed by a controlled breakdown of the amorphous Nb_2O_5. We have investigated the conditions which determine the filament formation as well as the mechaism of switching. Our results indicate that filament formation and switching are structural rather than electronic, and as such are not attractive for device application in any situation where reliability is required (i.e, computers).

In essence, we find that switching in Nb_2O_5 occurs in a small region or filament of the material which has been crystallized by a "forming" process. Switching itself involves the making and breaking of conductive metallic paths in the grain boundaries of the crystallized region. Apparently, metal from the low melting electrodes flows into the grain boundaries during the forming process. Since each switching event involves a change in the metal matrix material, the switch can be expected to have a limited lifetime.

We have developed a photocapacitance technique to study deep traps in insulators, and we have applied this method to an investigation of the traps at a SiO_2:Si_3N_4 interface. It is these traps which are responsible for charge storage and memory in an MNOS field effect transistor. From the photoexcitation data, we find that the electron traps that are filled and emptied in an MNOS memory transistor are 3.0 eV below the conduction band of Si_3N_4. These deep traps are not the same as those seen at 0.1 eV to 1.5 eV[4] by thermally stimulated current and I-V measurements on bulk Si_3N_4. It appears that the 3.0 eV deep trap is associated with the SiO_2:Si_3N_4 interface region and not with the bulk material.

A. ELECTRONIC CONTACT BARRIERS AND MORPHOLOGY OF Nb_2O_5 THIN FILMS

R. B. Laibowitz, T. H. DiStefano and S. Mader

Introduction

Amorphous thin films of Nb_2O_5 exhibit electrical switching between two resistance states; this bistable characteristic is usually obtained after the application of a high (forming) voltage to the nonconductive amorphous film.[1-3] The resistance states are stable at zero applied bias (memory effect) and resistance ratios between the high and low resistance state of greater than ten are commonly achieved.[3] A process of forming results in a locally damaged region of the insulator in which the bistable switching occurs. The structure of this conducting channel as well as the exact mechanism of switching has not been determined. We have used transmission electron microscopy to directly observe samples of pure and doped Nb_2O_5 during the forming and switching processes.[4] In this way, we found that the amorphous material crystallizes during the forming process and that further changes occur in the filament during the switching cycles.

The Nb_2O_5 films which are studied for their bistable characteristics are generally 1-2000 Å thick although thinner films can also be used.[2,5] They are grown on Nb substrates (either bulk or thin films) by any one of several techniques - anodization, sputtering, etc. Thus, Nb is generally one of the electrodes; for the counter or top electrode several materials have been used. Bi generally gives the best switching parameters but in general, the experimental results on the metal-Nb_2O_5-Nb sandwich structures appear to depend on the particular metal used for the counterelectrode. This has led to speculation on the role of the contact barrier at the metal-Nb_2O_5 interface in the conduction process.[1,6] For example, a localized barrier lowering could lead to enhanced electron injection and subsequent heating leading to the formation of a conducting channel.[7] In addition, reversible barrier lowering might possibly explain the bistable characteristic.[1] In order to study the barrier properities we have used the scanning internal photoemission (SIP) technique,[8] to resolve local barrier inhomogenities as small as 1 micron in spacial extent. As will be shown, it appears that contact barriers to the Nb_2O_5 films do not play as important a role in the switching properties as do structural imperfections. It does not appear that filament formation is related to a change in the contact barrier to the Nb_2O_5.

Experimental Technique

The thin film sandwich structures were formed on thin films of Nb deposited on Al_2O_3 or Si wafers. High quality films were obtained by either e-beam heating in a UHV system or rf sputtering.[5] For the films made in the UHV system, pressures during evaporation were generally 10^{-8} torr. The experimental results were not found to be significantly affected by the crystallinity of the substrate. The Nb_2O_5 films were

generally formed by wet anodization;[2,3,5] however it was found that sputtered oxide films could also be used with similar results. The sputtered Nb_2O_5 was particularly advantageous for making doped oxide films since the dopant could easily be added to the sputtering target and incorporated into the oxide film during the deposition. Bi was the principal impurity introduced in this way. Of the many counterelectrode materials from which a bistable Nb_2O_5 capacitor could be formed, this paper reports on results using only Bi counterelectrodes. These electrodes were semitransparent so that optical measurements could be made on the sandwich structure.

The basic apparatus for the SIP technique[10] is shown in Fig. 1. The use of a laser for the light source allows a newly resolution limited spot size to be used with subsequent high resolution scans obtainable. The sample is scanned by rotating mirrors which deflect the light spot to cover a 300μ x 300μ area of the sample. The He-Ne laser at a wave length of 6328 Å was used to excite the photocurrent from the bismuth electrode which was collected by the base electrode. The photocurrent which is porportional to the photoyield is then automatically plotted as a function of the spatial coordinates x and y of the sample. This is accomplished by having the photocurrent modulate the z axis on the display CRT as shown in Fig. 1. Also shown in the figure is the reflectivity system used to obtain a real image of the sample. It consists simply of a half silvered mirror and a photodiode detector which again drives the z-axis of the display CRT. This reflectivity system not only allows proper sample alignment but has also enabled one to examine the samples in a high contrast reflectivity mode.

Samples of Nb_2O_5 were also examined by transmission electron microscopy (TEM). A gap between two closely spaced metal electrodes (1-2000 Å spacing) was filled by sputtered Nb_2O_5 as shown in Fig. 2. This is basically the same geometry as we previously used in our GeTe studies[4,11] and the fabrication of such samples by e-beam lithography techniques is discussed in the references. With the back part of the wafer etched away as shown in the figure, the active element is transparent to the 100 kev electrons used in the TEM. This allowed high resolution microscopy and diffraction studies to be made. Nb electrodes were used in this lateral switching geometry. The effect of Bi electrode on the operation was successfully studied by doping the oxide with Bi. Past results had indicated[12] that a possible result of the forming was the incorporation of the Bi from the electrode into the oxide. Sample biasing was usually accomplished by using a curve tracing oscilloscope with a current limiting series resistor.

Experimental Results

Photoemission

As has been noted, we have used the SIP technique to study Nb_2O_5-Bi interface. In this case, the photocurrent was emitted from a 200 Å thick Bi electrode into the Nb_2O_5 by laser radiation. Long stripes of

Bi, about 0.025 cm wide, were used as electrodes. A typical SIP map is shown in Fig. 3a in which bright regions correspond to areas of high photoyield. The edge of the Bi stripe can be seen in the lower left. Seen in all such maps for Nb_2O_5-Bi interface are spotty dark regions which result from higher than average contact barriers. These dark regions are the dominant features in the photoemission from these samples. The vertical striations are produced by slow variations in the background leakage current through the sample and the data shown is a composite of many pictures taken along the stripe. A reflectivity map taken from the same region is shown in Fig. 3b, and the dark areas in reflectivity coincide exactly with similar regions in photoemission. This sort of reflectivity variation is typical of metal-insulator systems in which an interface reaction has taken place, i.e., in the dark regions the Bi electrode has reacted with the underlying Nb_2O_5. The patterns remain stable during heat treatments up to about 200°C.

In order to study the effect of the barrier on the switching and forming steps, the sample of Fig. 3 was biased to high voltages. This study was facilitated by the use of the thin electrode which allows several formings to be attempted. The conducting channel formed as a result of the high voltage always appeared in the dark regions of the SIP map where the contact barrier was highest. On the scale of about 1 micron, this observation tends to eliminate the model wherein local points of a lowered barrier are needed to initiate the conducting channel. While studies at much higher resolution (0.1μ) would be needed to completely eliminate this possibility, an alternate explanation is formulated which fits well with the TEM results. Thus, the dark regions where interface reactions have taken place are now spots in the Nb_2O_5. As the electric field across the sample is increased, these locations will be the first to break down, leading to the conducting channel. Such sites could originally form due to local hot spots during the evaporation or reflect defects or impurities in the substrate or film.

TEM

A top view of the sample geometry of Fig. 2 is shown in the micrograph of Fig. 4a. The Nb electrodes which are opaque to electrons which are used in the microscope appear black in the micrograph while the amorphous Nb_2O_5 appears lighter. The Nb_2O_5 also covers the Nb electrodes as well as filling the gap as the active element in Fig. 2. In situ electron diffraction on the amorphous material shows the typical amorphous patterns for both the pure and Bi-doped Nb_2O_5. Under electrical bias, the samples initially exhibit a very high resistance up to about 30 V for a gap width of about 2000 Å. At this field, a forming process occurs and crystallization of the amorphous material results. The shape of the crystallized region is filamentary and generally begins at an asperity on the electrode. Often such filaments will form at the sides of the electrodes rather than across the gap and an example of such a filament is shown in Fig. 4b. The filamentary

path in this case is semicircular from one electrode to the other and is made up of crystalline Nb_2O_5. Such edge filaments occur more regularly with narrow gaps in which there is insufficient contact or adhesion between the Nb_2O_5 within the gap and the electrode. This can also be seen in Fig. 4b by the slightly lighter regions adjacent to the electrodes. Other active, lower melting point temperature materials such as GeTe[4,11] fill the gap more efficiently and tend to form filaments directly across the gap. However, it is through these crystallized filamentary regions that the current flows after the forming process with a significant resistance drop.

In situ electron diffraction was used to identify the phases formed during the biasing. An electron diffraction pattern taken from the crystalline filament is shown in Fig. 5. Analysis of such data shows that the crystallites have the d-spacing corresponding to the high temperature, monoclinic phase of Nb_2O_5.[13] The particular monoclinic form which is observed is very close to the tetragonal variation and the crystals have lattice constants of 3.9 Å and 13.0 Å. Often the long axis is in the direction of current flow in the filament and follows a curvature defined by the expected field pattern. Upon further application of high currents, the crystallized region grows. These results are independent of the doping of the oxide and similar structures are seen in the Bi doped material.

Reproducible switching was not observed in these symmetric samples which have Nb electrodes on both sides of the gap. In order to simulate the effect of the Bi, up to 15 at. % of Bi was added to the Nb_2O_5 during the deposition. The initial resistance of the Bi doped oxide was again quite high but a lower forming voltage was needed to induce the crystallization. As discussed above, similar patterns and phases were observed in both doped and pure Nb_2O_5. However, a much lower resistance state was obtained in the Bi doped sample. A closer examination of the crystallized region in these samples showed that the grain boundaries were more pronounced and changed with increasing current as shown in Fig. 6. Figure 6a shows a section of the filament immediately after forming in which the crystalline grains can easily be seen. As increasing current passes through this section, the structure of the grain boundaries change as shown in Fig. 6b. The effect of the current makes the boundaries transparent, first in spots and then along the length of the boundary. Either material is lost from the boundary or agglomeration at boundary intersections is occurring. As the effect is somewhat reversible at low current densities, some movement and pile up is expected with loss of material occurring at high current densities. This result appears to be due to precipitation of the Bi at the internal surfaces and leads to highly conductive, almost metallic paths through the oxide. This explanation is reasonable in light of the fact that Bi is virtually insoluble in crystalline Nb_2O_5.

Continued switching of these planar samples usually led to an irreversible failure. The particular structure is quite useful for

applying fields to active materials while viewing the sample via TEM. However, because TEM requires very thin films, the quantity of material being biased is very small and filament growth, thin spots, adhesion and heating problems usually lead to sample failure. In addition, for the planar samples only similar electrodes were prepared and comparison of detailed switching mechanisms including temperature dependence was not possible.

Discussion and Conclusions

During the course of this work, basically two models were proposed to explain the initiation of the forming and subsequent switching. The first one considered that sites of local barrier lowering might exist as observed in other systems[7] leading to enhanced electron injection, heating and filament formation. The contact barrier to the filament would then continue to play a role in the switching cycles. While the exact mechanism for the switching remains to be determined, we have not seen any sites of significant local barrier change although a patchy barrier has been observed. Rather, the more straightforward explanation of filament formation based on weak spots or asperities seems to fit the results of the photoemission and TEM work. At such sites a field enhancement occurs and breakdown occurs at the weakest point. Sites where interface reactions have taken place or local thin spots would be the most likely candidates. The thin spots in the sandwich geometry would correspond to asperities on the electrodes as preferred sites. This observation fits nicely with the combined results from the photoemission and TEM.

The TEM work has also shown conclusively that crystalline filaments form the conducting paths in Nb_2O_5. The low resistance state in the bistable resistor formed by Bi-Nb_2O_5-Nb samples is known to be almost metallic[3] in nature. A likely explanation for this effect can be formed from our work on doped Nb_2O_5. The Bi (and possibly other metallic impurities) is incorporated into the amorphous oxide during growth or during forming. Since the Bi is insoluble in the crystalline matrix, Bi must precipitate at internal surfaces like grain boundaries once crystallization has occurred. This process produces highly conductive paths between the electrodes and thus appears responsible for the low resistance state. The Bi in the grain boundaries appears to be mobile under bias and this mobility leads to resistance changes when the electrical continuity of the paths is broken. However, dc tailed switching studies must await samples with dissimilar electrodes but it does appear that many of the results obtained on Nb_2O_5 bistable resistors can be understood in terms of structural phenomena. This conclusion would lend to agree with observations made on other switchable materials.

The authors wish to acknowledge helpful discussions with R. Rosenberg, K. C. Park and the assistance of S. Libertini, A. A. Levi, J. M.Viggiano and S. Herd.

References

1. R. B. Laibowitz, L. Esaki and P. J. Stiles, Phys. Lett. 36A, 429 (1971).

2. T. W. Hickmott and W. R. Hiatt, Sol. State Elect. 13, 1022 (1970).

3. S. Basavaiah and K. C. Park, IEEE Trans. ED-20, 149 (1973).

4. P. Chaudhari and R. B. Laibowitz, Thin Solid Films 12, 239 (1972).

5. R. B. Laibowitz and A. A. Levi, Conduction in Low Mobility Materials, Taylor and Francis, London, 1971, p. 63.

6. ARPA Technical Report No. 1, Contract No. F19628-73-C-0006, Jan. 31, 1973.

7. T. H. DiStefano, J. Appl. Phys. 44, 527 (1973).

8. T. H. DiStefano, Appl. Phys. Lett. 19, 280 (1971).

9. A. F. Mayadas, R. B. Laibowitz and J. J. Cuomo, J. Appl. Phys. 43, 1287 (1972).

10. T. H. DiStefano and J. M. Viggiano, IBM J. Res. and Develop.,

11. R. B. Laibowitz, S. R. Herd, P. Chaudhari, Phil. Mag. 28, 1155 (1973).

12. K. C. Park, Private Communication.

13. F. Laves, R. Moser and W. Petter, Naturwiss. 51, 356 (1964).

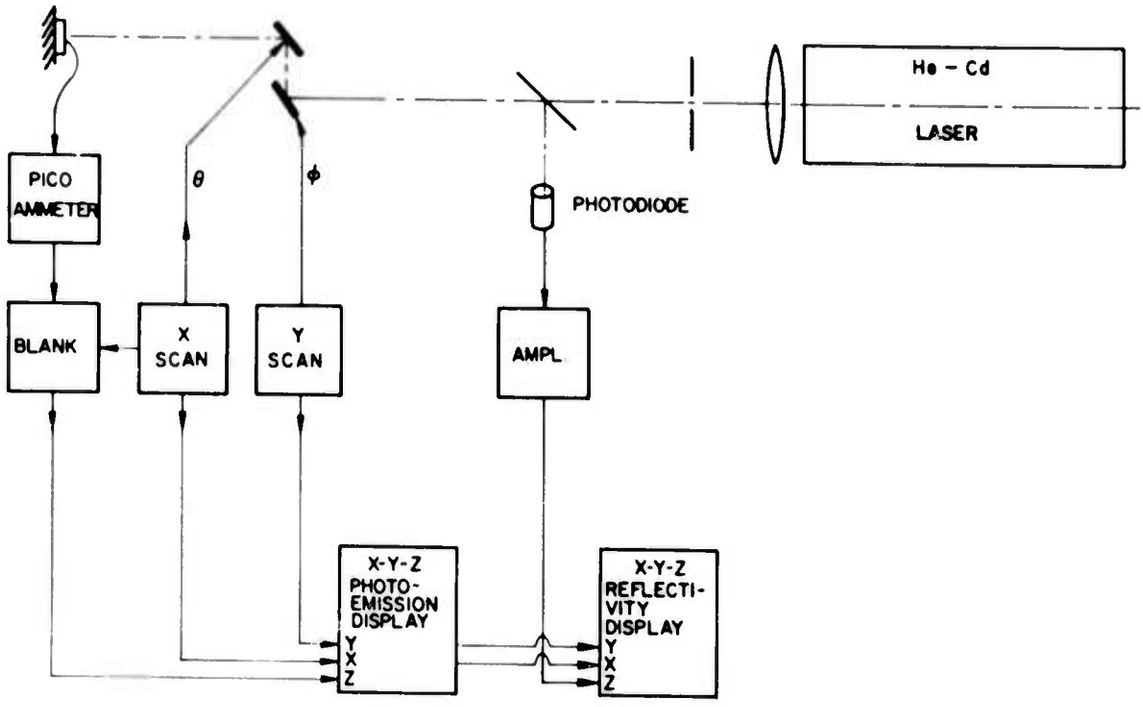

Figure 1: Measurement apparatus for the SIP system. Photocurrent produced by a scanning light spot is detected and displayed as a function of X and Y on a display CRT.

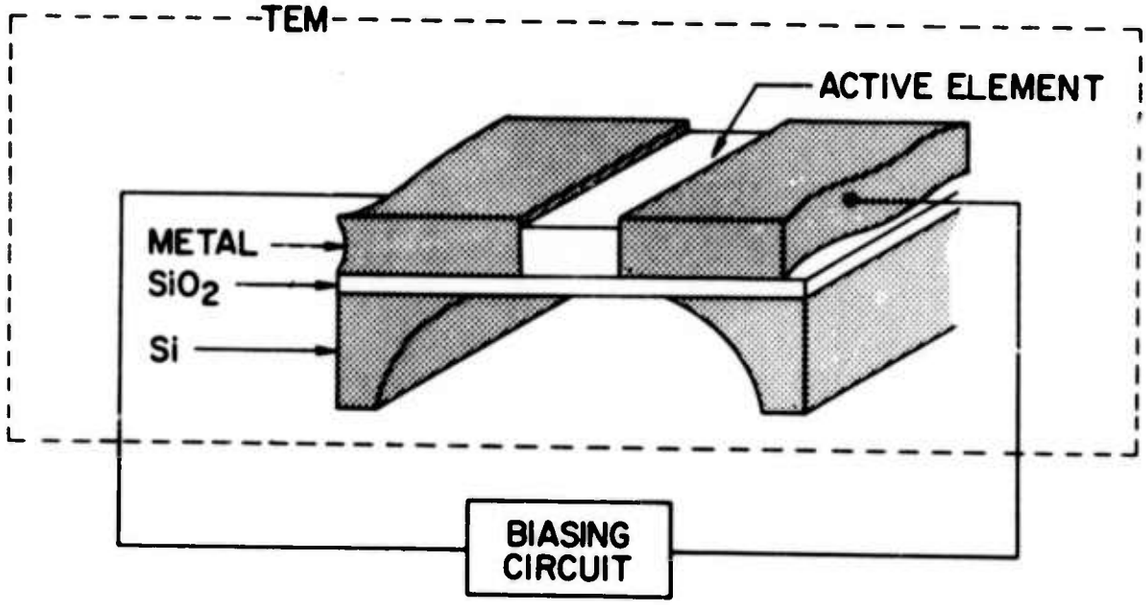

Figure 2: Schematic diagram of a sample prepared for simultaneous transmission electron microscopy (TEM) and electrical biasing measurement.

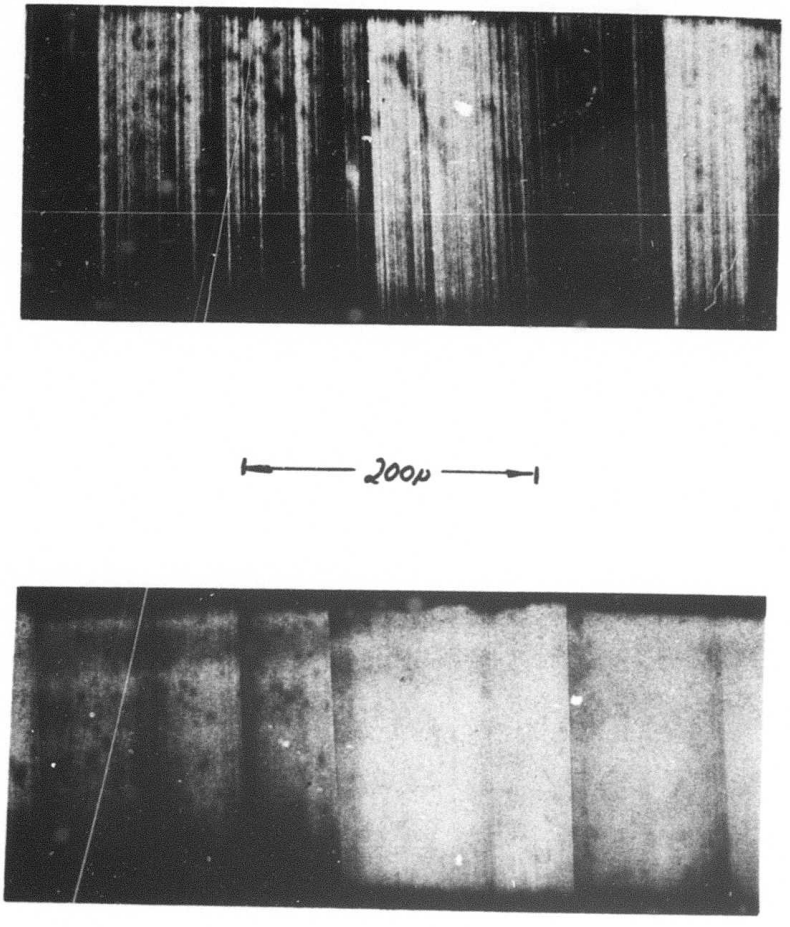

Figure 3: (a) Scanning Internal Photoemission map of the Nb_2O_5-Bi interface. The bright areas correspond to a relatively large photoelectric yield. (b) High contrast scanning reflectivity measurement of the same area as that shown in the photoemission measurement in (a).

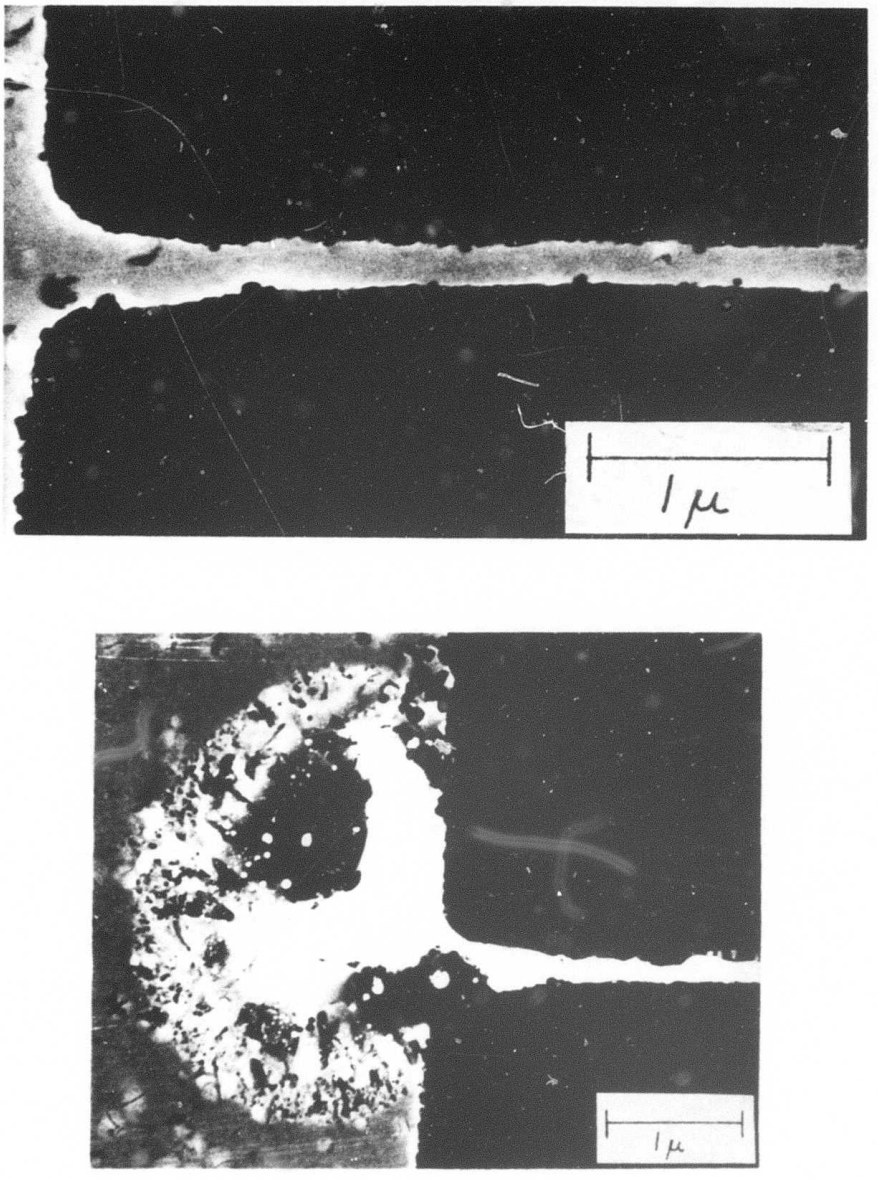

Figure 4: (a) Electron micrograph of the gap between two Nb electrodes. Amorphous Nb_2O_5 is between and around these electrodes.

(b) Typical edge - formed, crystalline filament after application of 30 volts across the gap.

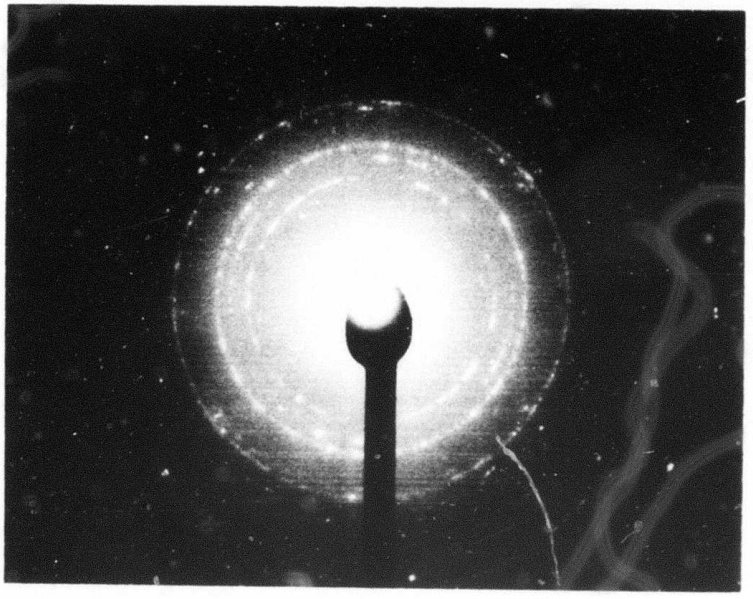

Figure 5: In situ electron diffraction pattern taken from the filaments formed from the amorphous Nb_2O_5.

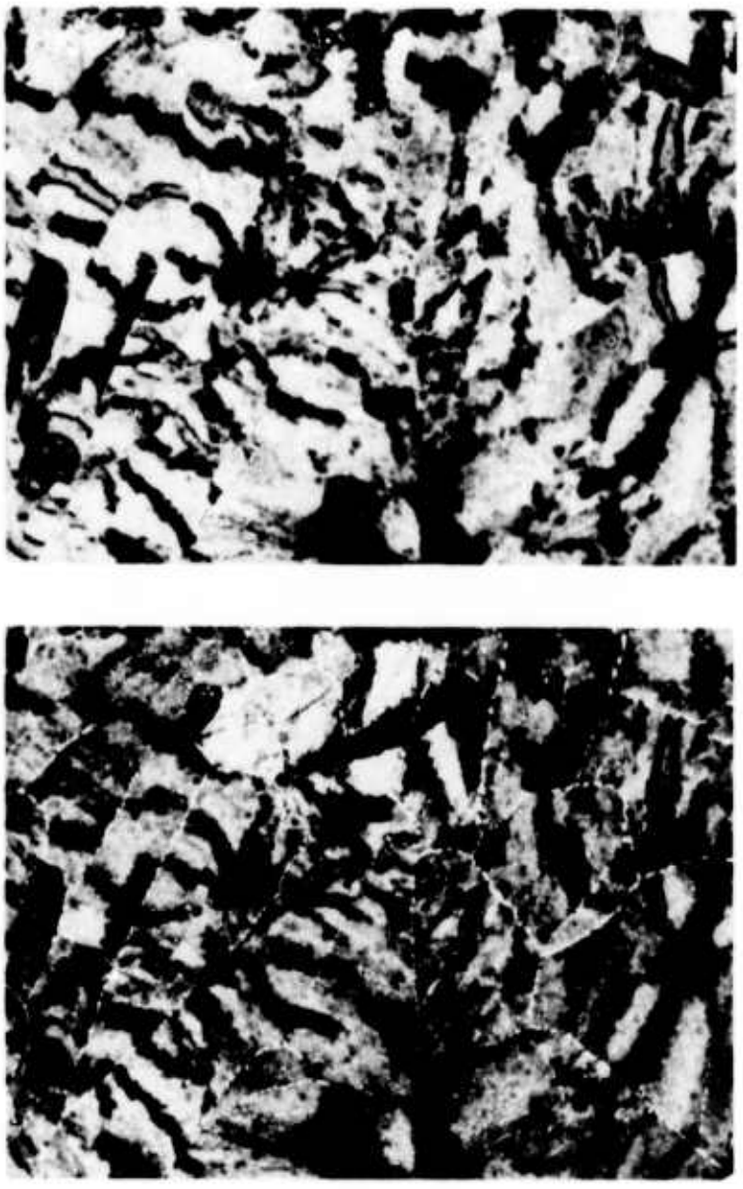

Figure 6: Micrographs of Nb_2O_5 crystallites in the conducting channel formed in Bi-doped Nb_2O_5 ($\sim$ 15 at. % Bi added to target)

(a) Before application of high current.
(b) After application of high current in which grain boundaries become more prominent.

B. ELECTRONIC STRUCTURE OF THE SiO_2:Si_3N_4 INTERFACE

T. H. DiStefano and J. M. Franz

INTRODUCTION

Electron traps in Si_3N_4 have been well characterized by several techniques including thermally stimulated currents[1-3] and I-V measurements.[4-6] Both techniques are able to determine the binding energy of traps which are characteristic of the bulk of Si_3N_4. Binding energies are found to lie in a range from about 0.1 eV to 1.2 eV, as measured by thermally stimulated currents and from about 0.5 eV to 1.5 eV determined from the I-V dependence. However, neither of these techniques is capable of being used to characterize the deep trapping levels associated with charge storage near the SiO_2:Si_3N_4 interface. It is the deep trap states near the interface of SiO_2 and Si_3N_4 which are responsible for charge storage in the MNOS memory transistor. A determination of the energy distribution of the deep traps associated with the interface is the primary object of the study presented here.

We have developed an used a photocapacitance technique to determine the distribution of the traps, near the SiO_2:Si_3N_4 interface, which are filled and emptied by electron tunneling in an MNOS transistor structure. The technique involves a measurement of the change in the stored charge near the interface induced by an exposure to monochromatic light. From the net decay in stored charge produced by light of various wavelengths, the spectral dependence of photoyield was determined for emission from the deep traps. The total charge on the interface is measured essentially by using the silicon substrate as an electrometer. From the voltage that must be applied to the silicon to maintain a condition of zero surface electric field, the total trapped charge was determined quite sensitively; the zero field condition was sensed by a measurement of the total capacitance of the MNOS structure. The spectral photoyield was obtained for traps filled in several ways and to various levels of total stored charge. From the photoemission spectra and thresholds, information is derived about the energy distribution of the deep traps responsible for memory in the MNOS transistor.

EXPERIMENT

The photoemission measurements of SiO_2:Si_3N_4 were performed on samples which are characteristic of an MNOS transistor. A sandwich structure was composed of a silicon substrate, 25 Å of SiO_2 formed on the silicon by oxidation, 400 Å of Si_3N_4 formed by chemical vapor deposition at 875°C, and finally 125 Å of aluminum to form a semitransparent electrode. Sampeles were formed on (100) 2Ω-cm silicon substrates of both n and p type. The semitransparent electrodes, 0.032" in diameter, were deposited by evaporation in a vacuum of about 2×10^{-6} torr. The samples exhibited typical charge storage and hysteresis effects, with a maximum total charge of about 1.3×10^{13} electrons/cm^2.

A photocapacitance technique was used to determine the photoyield from traps near the SiO_2:Si_3N_4 interface. During the measurements, a bias voltage was applied to the MNOS sandwich to maintain a zero electric field at the silicon surface, as is shown in Fig. 1. The zero surface field condition was sensed by a capacitance measurement at 100 KHz and maintained by a feedback loop from the capacitance measurement back to the sample bias. The capacitance was measured by a phase sensitive technique in order to reject leakage currents and photocurrent. In this flat-band condition, the bias voltage is directly related to the net charge density stored at the SiO_2-Si_3N_4 interface,

$$\rho = \frac{\varepsilon_0 \varepsilon_2 V_{fb}}{a} \quad , \tag{1}$$

where ρ is the net charge density, ε_2 is the dc dielectric constant of the Si_3N_4, V_{fb} is the bias voltage necessary to maintain the "flat-band" condition, and a is the thickness of the Si_3N_4 layer. It was assumed that the stored charge lies near the SiO_2:Si_3N_4 interface; this assumption is reasonable in this case, where the charge was introduced by tunneling from the silicon or by photoemission from the silicon.

The photoresponse of the system was obtained by shining monochromatic light through the semitransparent aluminum electrode and onto the SiO_2:Si_3N_4 interface. The light source was a Bausch and Lomb 0.5 meter monochromator with a Hg-Xe high pressure arc source. The emergent light was de-focused to cover uniformly the area of the sample electrode. The light intensity was measured with an RCA 1P42 photodiode covered by a layer of sodium salycilate phosphor; the photodiode was calibrated against an Eppley thermopile. Measurements were obtained for photon energies from 2 eV to 6 eV, which is the upper practical limit of the light source. A filter was used at energies below 3.5 eV to eliminate second order light in a range over which the sample was extremely sensitive. All of the spectra presented below were obtained at room temperature.

Light of sufficient energy $\hbar\omega$ excited electrons from the deep traps into the conduction band of the Si_3N_4. For the condition shown in Fig. 1, electrons excited into the Si_3N_4 are collected by the aluminum electrode; re-trapping of the electrons in the Si_3N_4 was not found to be a significant factor. Because of the photoexcitation of electrons from traps and the resulting discharge of the interface, the flat-band voltage shifts with exposure to light. The photoyield $Y(\hbar\omega)$ is then obtained as

$$Y(\hbar\omega) = \frac{\varepsilon_0 \varepsilon_2}{aeI(\hbar\omega)} \left.\frac{\Delta V_{fb}}{\Delta t}\right|_{\hbar\omega} \quad , \tag{2}$$

where $I(\hbar\omega)$ is the monochromatic photon flux at energy $\hbar\omega$ and is the electronic charge. The measurements were made in steps of finite internal Δt, which was between 10 and 60 seconds. The interval Δt was chosen t be sufficiently brief so that the total spectrum was not appreciably distorted by a deflection of the trapped charge near the end of the measurements sequence. The discharge measurements were performed in order, from low to high photon energy.

Photoyield spectra were obtained from the decay of V_{fb} caused by a sequence of light exposures. Typically, the decay of V_{fb} follows that shown in Fig. 2, which shows data for three different initial charge densities. In this case, the sample was exposed to 15 sec of light, in turn, at increasing photon energies spaced 0.1 eV apart. Some portion of the initial trapped charge is depleted during the course of the measurement, leading to some distortion of the spectra from this data, as will be discussed below. Another point of note is that throughout the set of measurements reported in Fig. 2, the electric field in the Si_3N_4 was always greater than 10^6 V/cm, which is sufficient to ionize shallow traps in the bulk of the Si_3N_4 and to assure the collection of electrons injected into the conduction band of the Si_3N_4.

Photoionization spectra were obtained for both positive and negative initial charge in the interface region. In the case of a net negative charge, the optical excitation was performed with the field conditions shown in Fig. 1 where the emitted electrons were collected by the aluminum electrode and the silicon surface was at zero field. The initial negative charge was introduced by either of two means, tunneling of electrons from the silicon or by photoinjection from the silicon produced by light of 5 eV photon energy. In the case of a net positive initial charge, the aluminum electrode was made positive during the optical excitation so as to collect any electrons emitted from the interface; in this case, the silicon surface was at a flat band condition only in the interval during which V_{fb} was measured. Thus, for initial conditions of both positive and negative charge, the electrons excited out of deep traps were swept through the Si_3N_4 and collected by the aluminum electrode.

Results

Photoyield spectra were obtained from the V_{fb} discharge curves by equation 2, which relates the photoyield Y to a shift in V_{fb}. The spectrum for a net initial electron density of 8.5×10^{12} e-/cm^2 is shown in Fig. 3. Similar spectra were obtained for initial conditions of 7.2×10^{12} e-/cm^2 and 5.5×10^{12} e-/cm^2. The spectra display a parabolic rise in yield above a threshold about 3.0 eV. The yield in Fig. 3 reaches a saturation level at a photon energy of about 4.0 eV, and then falls off. At photon energies above 4.25 eV, the yield drops rapidly to a negative value because of the filling of traps by photoinjection from the silicon substrate. Because of the photoinjection, the photoyield spectrum is valid only for photon energies below 4.25 eV.

For photon energies below 4.25 eV, the yield spectrum shows no structure other than the parabolic edge near threshold in all cases of a net negative charge, the shape of the yield curve is not significantly influenced by the total charge density. At proton energies near threshold, a plot of the halfpower of yield vs photon energy fits the data quite well, as in Fig. 4 to determine a threshold for ionization of about 3.0 eV. It is interesting that the threshold increases from 3.00 eV to only 3.05 eV when the net negative charge is changed from 5.5×10^{12} e-/cm^2 to 8.5 e-/cm^2. This suggests that the distribution of traps is not filled in sequence from low to high energy, but rather the traps are filled uniformly at all energies of the distribution.

Some information can be obtained from the decay of V_{fb} or stored charge in response to light of different photon energies. Figure 5 shows time dependent discharge curves for 3.5 eV, 4.0 eV, and 4.5 eV. Both the 3.5 eV and the 4.0 eV discharge curves decay to the same saturation value, corresponding to a drop in net stored charge from 8.5×10^{12} e-/cm^2 to about 3.4×10^{12} e$^-$/cm^2. Presumably saturation corresponds to the point at which all electrons accessible to ionization by a single photon have been removed. The remaining charge can be removed by a multi-step process which would be considerably slower in removing trapped charge. The discharge curve is quite different for light of 4.5 eV photon energy. Here, the V_{fb} decays rapidly to a saturation level which is higher than that at 3.5 eV or 4.0 eV; this larger net charge at saturation results from the operation of two competing processes, filling of traps by photoinjection and emptying by photoionization.

DISCUSSION

The imformation derived from the photoionization study adds to our knowledge of the SiO_2:Si_3N_4 interface, which is shown schematically in Fig. 6. The electronic levels are shown for the specific MNOS structure comprising Si:SiO_2:Si_3N_4:Al. As found in the photoionization study, the electron traps lie in a band beginning 3.0 eV below the Si_3N_4 conduction band. The total width of this trap band is less than 0.5 eV. However, other trap bands are thought to exist below the 4.25 eV limit of validity of the photoionization technique; these deep traps are responsible for the net positive stored charge in the MNOS structure. Another technique would be necessary to probe the deep traps with a binding energy greater than 4.25 eV.

The traps responsible for negative charge storage lie in a band 3.0 eV to 3.5 eV below the Si_3N_4 conduction band. No evidence is found in the photoionization measurements for electrons in the shallow traps, seen in TSC and I-V measurements at 0.1 eV to 1.5 eV binding energy, which are characteristic of bulk Si_3N_4. Presumably, the shallow traps throughout the bulk of the Si_3N_4 are ionized in the high electric fields

required to induce filling of the 3.0 eV deep traps. As a result, the traps responsible for charge storage in MNOS structures are not the shallow traps below 1.5 eV binding energy, but rather they have 3.0 eV or more binding energy. With the generally accepted 1.1 eV discontinuity in conduction bands between the SiO_2 and the Si_3N_4, the top of the trap distribution is 0.15 eV above the silicon valence band. This trap energy is somewhat lower than might be expected. However, the trap is somewhat approximate because of the uncertainty in the 1.1 eV step at the SiO_2: Si_3N_4 interface. A downward adjustment of the MeV step would raise the trap distribution with respect to the silicon.

References

1. E. J. M. Kendall, Phys. Stat. Sol. 32, 763 (1963).

2. R. Starnes, Report R554 April 1972.

3. J. M. Franz, D. Fitzgerald, and T. H. DiStefano, Charge Trapping in MNOS Capacitors, Electrochemical Society, 145th Meeting, San Francisco, May 13017, 1974.

4. E. J. M. Kendall, Canadian J. of Phys. 46, 2509 (1968).

5. S. M. Sze, J. Appl. Phys. 38, 2051 (1967).

6. Brown, Robinette, and Carlson, J. Electrochem. Soc. 115, 948 (1968).

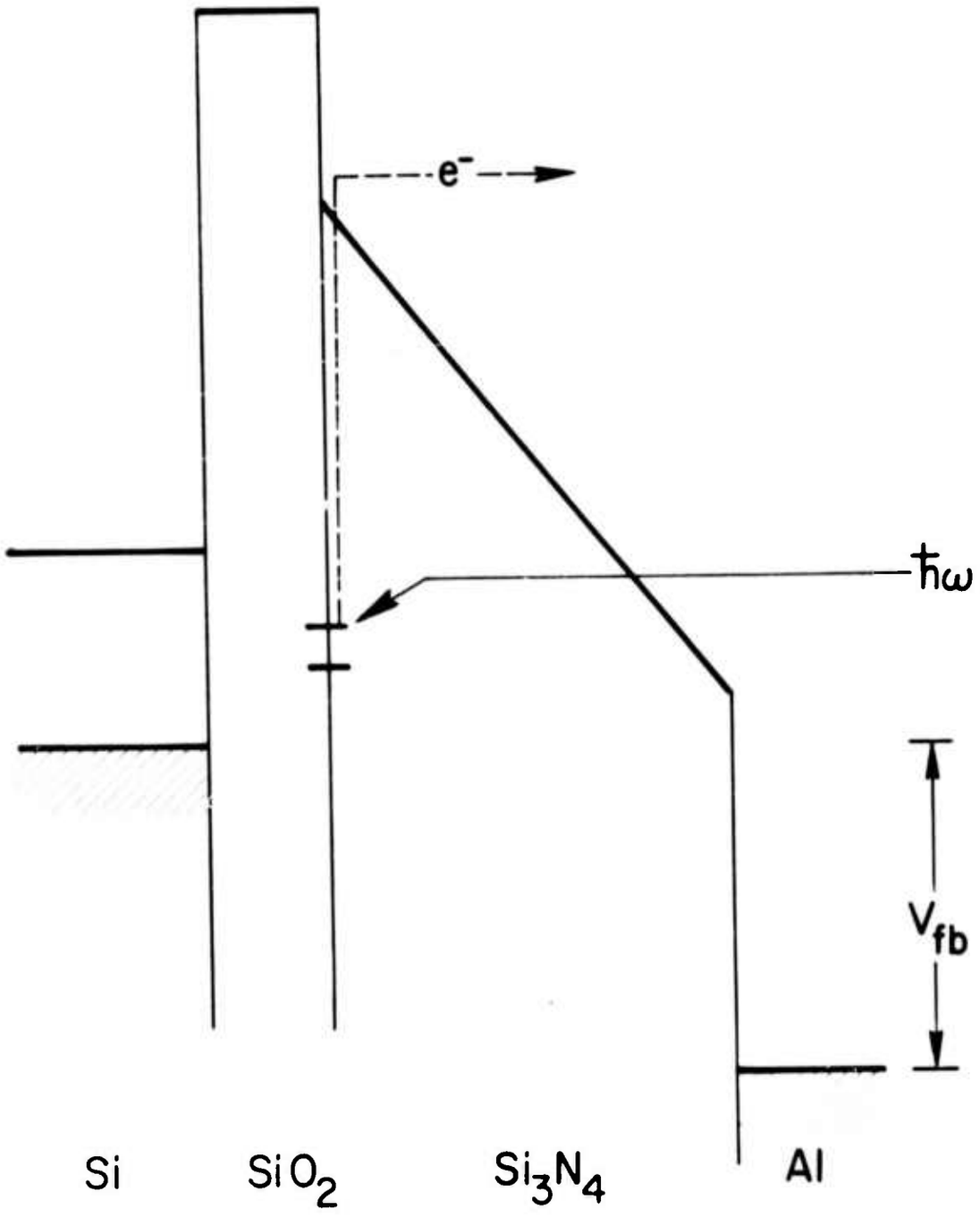

Fig. 1: Schematic representation of the photocapacitance technique which was used to determine the energy distribution of electrons trapped in a SiO_2:Si_3N_4 system. A semitransparent aluminum electrode is maintained at a potential V_{fb} at which the electric field at the silicon surface is zero. The zero field condition is sensed by a high frequency capacitance measurement and maintained by a feedback circuit. Photons of energy $\hbar\omega$ excite electrons from traps in the system to cause a change in the V_{fb} which can be related to a photoemission yield for the process.

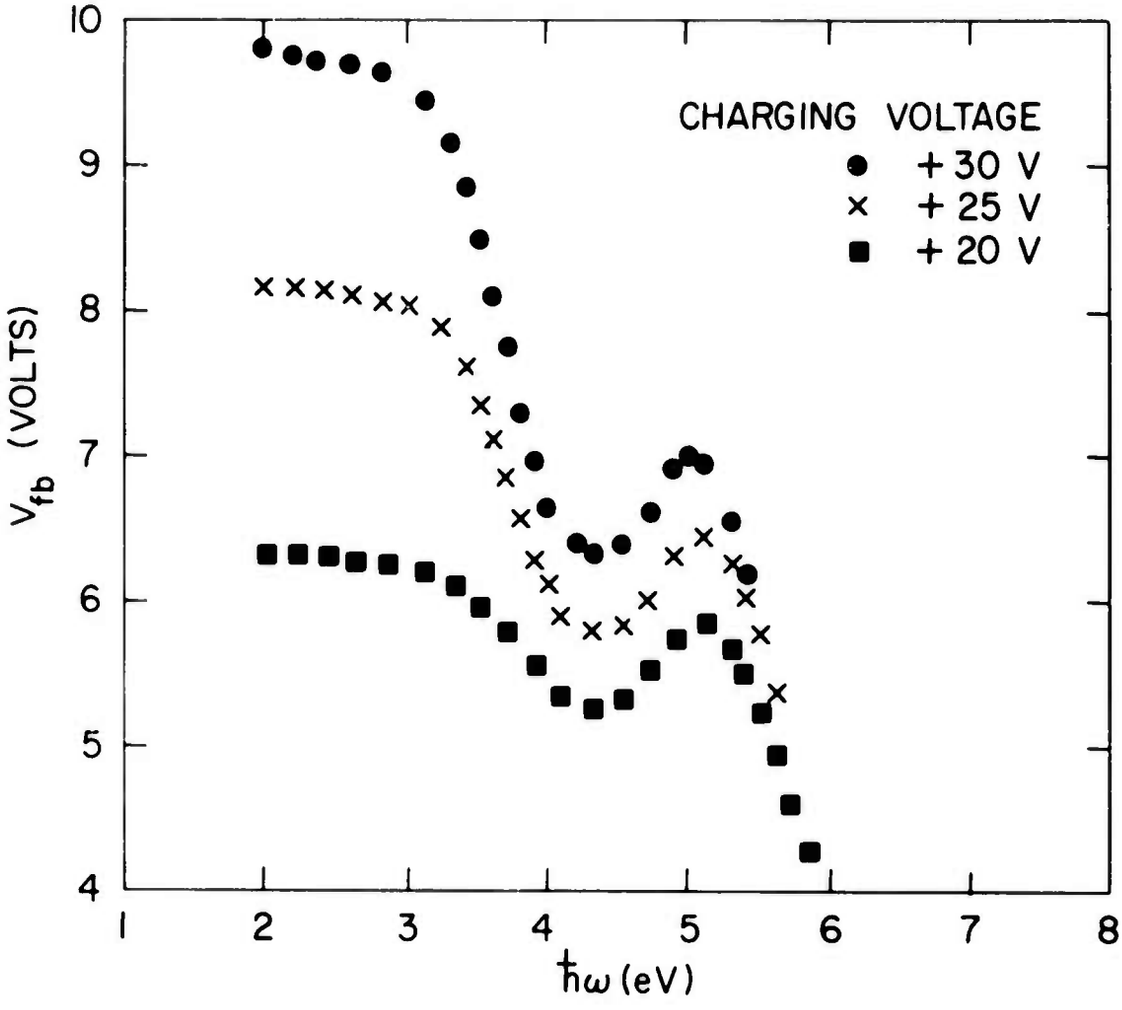

Fig. 2: Spectral dependence of the photon induced discharge of the sample for three different levels of initial charge. The discharge curves show the decay of the flat-band voltage caused by a 15 second exposure to light of the specified photon energy. The points were measured in sequence, from low to high photon energy.

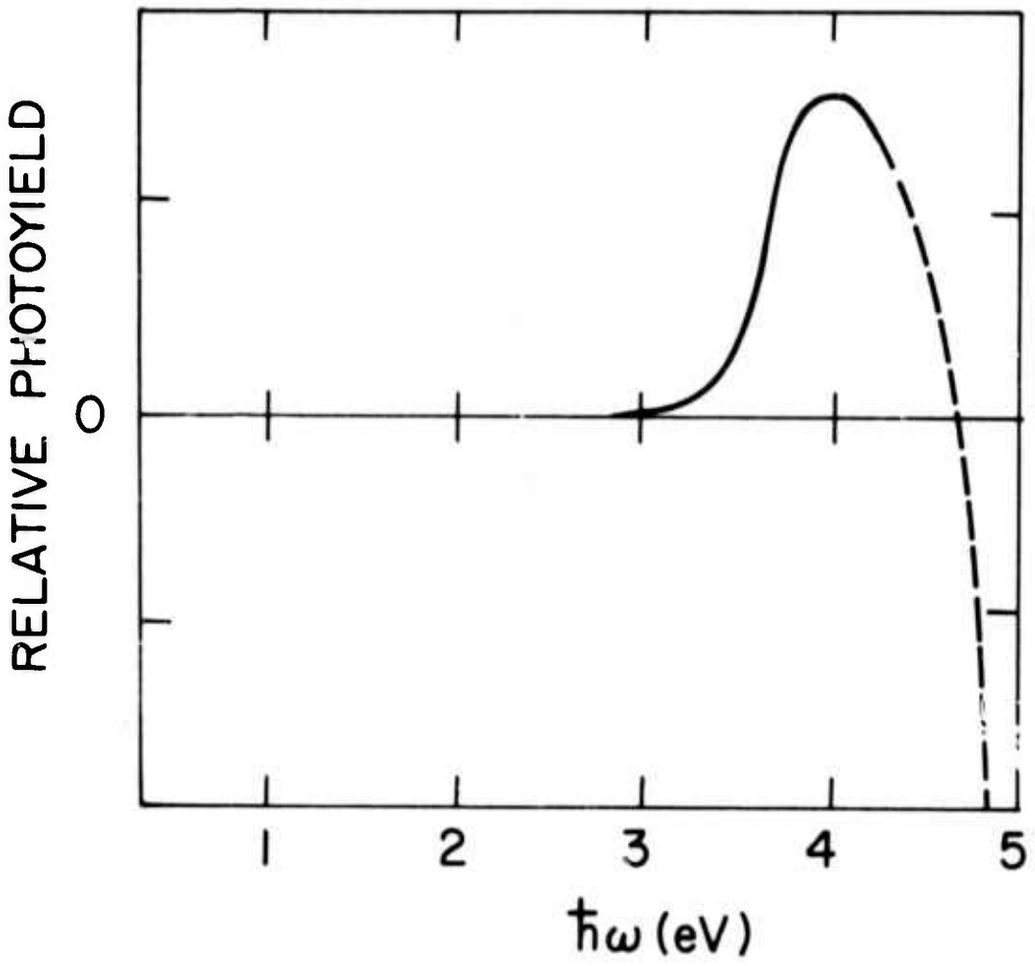

Fig. 3: The spectral dependence of the yield for photoemission from traps near the SiO_2:Si_3N_4 interface. The negative photoyield at energies above $\hbar\omega \cong 4.7$ eV is due to the filling of traps caused by photoninjection from the silicon substrate. The photoyield at photon energies above $\hbar\omega = 4.25$ eV contains a component due to the filling of traps by photoinjection.

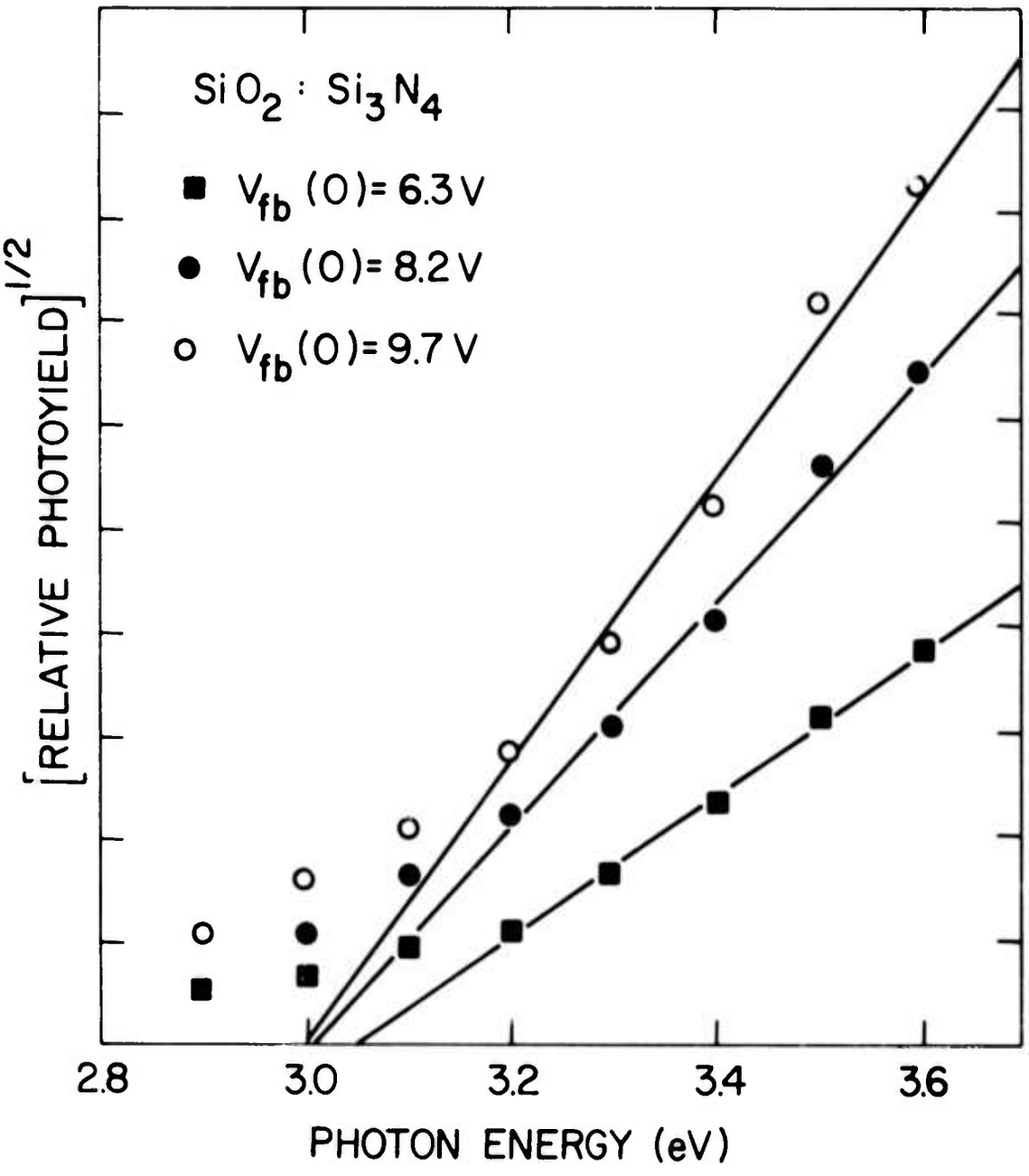

Fig. 4. The dependence of photoyield near the threshold for photoexcitation. The threshold for photoemission is determined by a half power plot to be 3.00, 3.01, and 3.05 eV $\pm$ 0.02 eV for initial trapped charge densities of 8.5×10^{12}, 7.2×10^{12}, and 5.5×10^{12} electrons/cm^2, respectively.

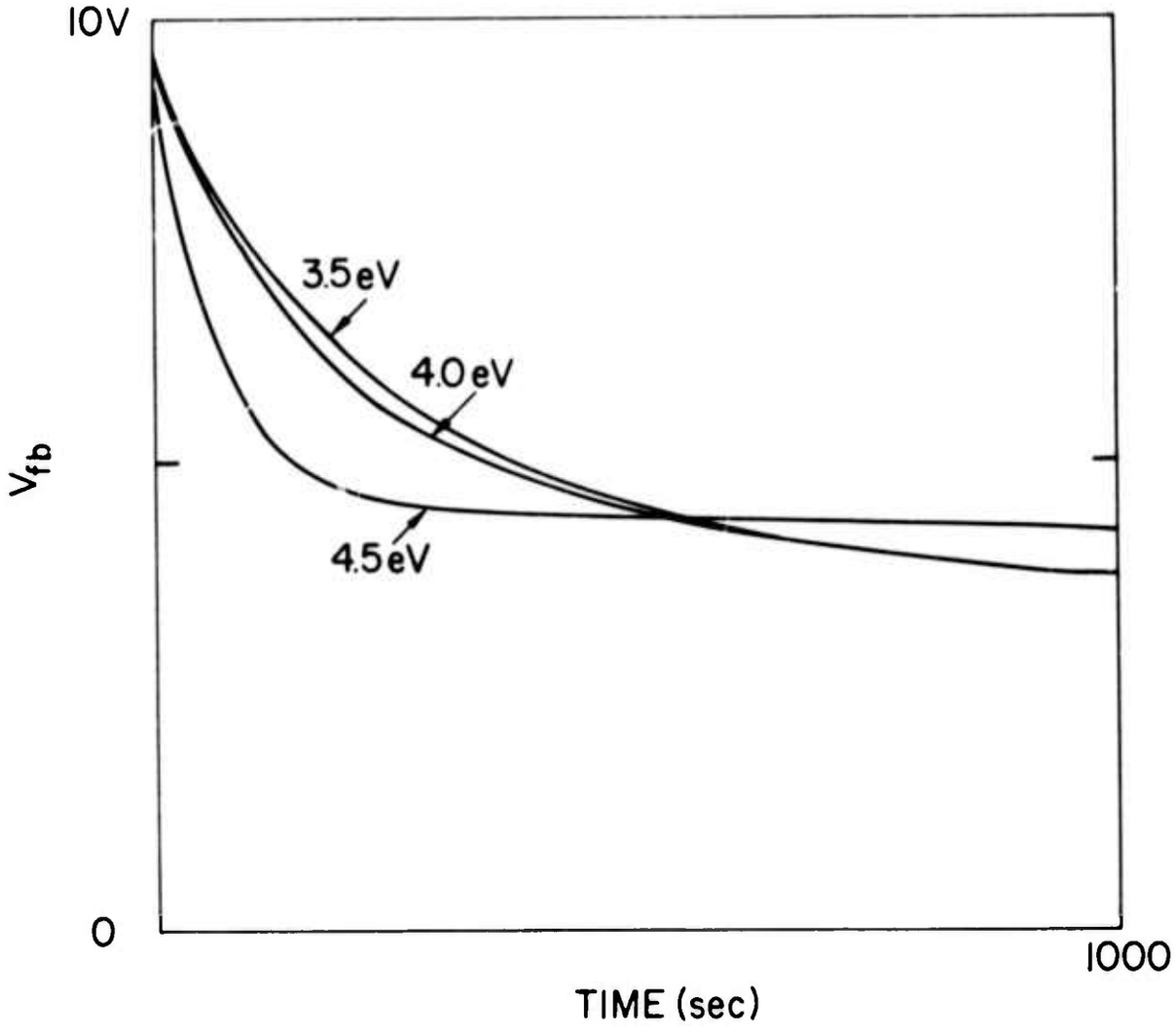

Fig. 5: The change in V_{fb} produced by exposure to photons of three different energies. The flat-band voltage relaxes to a saturation value of 3.9V for a photon energy of 4.0 eV and below. Above 4.0 eV, the saturation flat band voltage is somewhat higher due to the operation of two competing processes: photo-depopulation of traps and trap filling by photoinjection from the silicon.

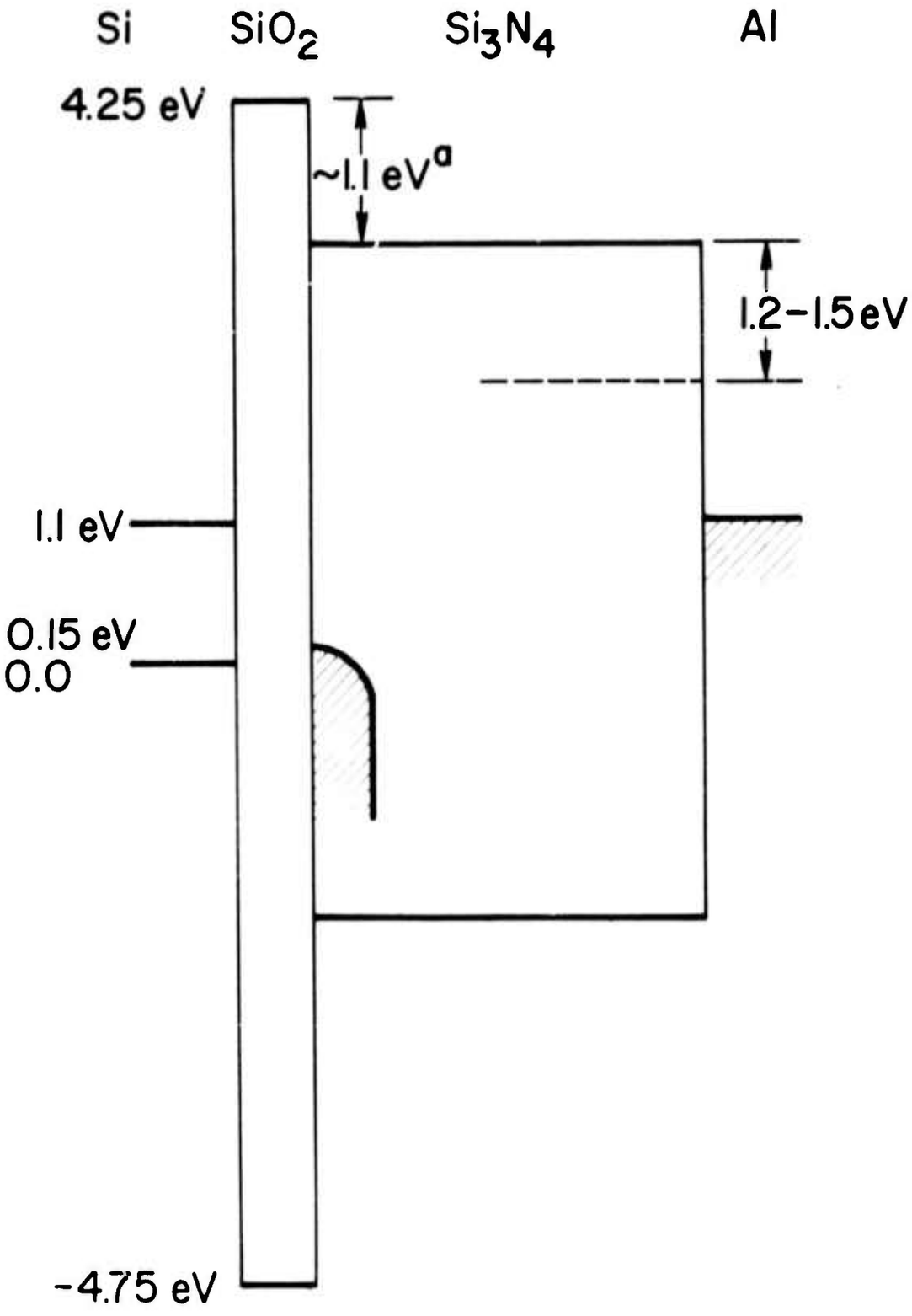

Fig. 6: The energy level diagram for the system SiO_2:Si_3N_4 showing the energy of the electron traps near the interface.

III. INSTABILITIES ASSOCIATED WITH METAL-GLASS INTERACTION

In present silicon devices, metals that make contact with SiO_2 are conductors such as Cu, Au, and Al, and transition metals such as Cr, Ti and V. Typical arrangements are triple-layer structure, e.g. $Au/Cr/SiO_2$, where a thin transition metal is used as an intermediate layer to develop strong adhesive bonds to the insulator. The high reactivity of a transition metal, however, has been found to lead to an easier decomposition of SiO_2 and reduces its insulating capability as reported in the 1st and 2nd semi-annual reports. The conducting metals potentially can also cause damage to the insulator due to their fast diffusion rate in glasses and their catalytic effects on devitrification. Even though the conducting metals usually are not fabricated in direct contact with the glass, we must point out that the intermediate transition metal layer is not a good diffusion barrier to prevent the conducting metallic atoms from reaching the insulator. To investigate the damaging effect of interaction of conducting metals and glasses, we have studied the morphology and kinetics of surface reactions for $Au/SiO_2/Si$ structure. When samples are held at elevated temperatures (above 500°C) in a dynamic vacuum, we observed an apparent decomposition of the glass film with subsequent migration of Au along the silicon surface. The migration is found to follow the crystallographic direction of the silicon. The decomposion of the glass film is dependent on the Au and on the partial pressure of oxygen of the environment.

Since glass-metal interaction is undesirable from the standpoint of the integrity of the glass, it is needed to strengthen the glass to show a better resistance to attack by metallic ions. Structurally, the network configuration of a glass is very loose and could be packed into a denser form. A denser form of glass is ideally better and is particularly desirable whenever a very thin glass layer (< 1000 Å) is required because thin glasses are especially vulnerable to pin holes. We have developed a new technique which potentially may be applied to densify a glass layer and to reduce its pin hole density. The technique is to expose the glass to a low dosage, high energy ion beam. The amount of compaction has been measured by Talystep and confirmed by the changes of density and reflective index obtained by ellipsometry. The densified glass layer has also been found to show an improved dielectric breakdown strength.

In the last session of this report, we presented our continuing progress on the understanding of silicide formation. Silicide, as shown in our earlier reports, is a product of glass-metal reaction. By directly reacting Ni with Si, a sequential formation of Ni_2Si, NiSi and $NiSi_2$ has been observed. The phase $NiSi_2$ is found to grow epitaxially on Si surfaces. We note that the epitaxy is obtained by solid state reaction rather than by the well-known liquid phase or vapor phase epitaxy.

A. SURFACE REACTIONS ON MOS STRUCTURES

E. I. Alessandrini, D. R. Campbell and K. N. Tu

Abstract

The morphology of surface reactions for $Au/SiO_2/Si$ structures has been studied as a function of environment. It was found that the reaction between thin gold film dots and thermally oxidized Si was strongly influenced by the partial pressure of oxygen. When samples are held at elevated temperatures (above 500°C) in a dynamic vacuum, an apparent decomposition of the oxide film with subsequent migration of Au along the exposed silicon surface was observed. The migration was found to follow the crystallographic directions of the silicon. Reduction of the oxide was dependent on the presence of the Au layer as regions free of Au remained intact. The reaction as a function of time, temperature, SiO_2 thickness and ambient conditions has been studied using optical microscopy as well as electron microprobe, microscopy, and diffraction techniques.

Introduction

An important consideration in the design of metal-oxide-semiconductor (MOS) devices is to choose combinations of materials which will retain their chemical and structural stability during fabrication and throughout operation. Gold is frequently a choice for the metal layer, largely because it is chemically inert and films are easily formed by sputtering or evaporation. However, other factors, such as poor adherence to SiO_2, reactivity with Si and high cost limit its use commercially.[1-3] Previous investigations on the stability of $Au/SiO_2/Si$ structures to heat treatments at temperatures from 800 to 1200°C have dealt with the diffusivity of Au through SiO_2 and with changes in electrical properties which accompany the migration of Au through the film and into the underlying Si. In general, the effects of varying environmental conditions such as the partial pressure of oxygen were not included.

In the course of experimentation on the stability of $Au/SiO_2/Si$ structures with respect to chemical reaction, devitrification, etc., during thermal stressing in various environments, we have observed a catostrophic mode of degradation of the oxide film which occurs in dynamic vacuum. After several hours of annealing at temperatures in the range 500 to 700°C, portions of the oxide in the vicinity of the Au are completely reduced. Concommitantly, Au reacts with the exposed Si and migrates in selective directions over the Si surface. Although this complex phenomena is not understood in terms of a sequence of basic mechanisms, the distinctive morphological changes that occur are readily observable and provide interesting examples of reactions that are unique to surfaces. We present here a qualitative description of these reacted surfaces which have been studied in various stages of development, noting effects of temperature, film thickness and environment using several analytical and microscopy techniques.

A. SURFACE REACTIONS ON MOS STRUCTURES

E. I. Alessandrini, D. R. Campbell and K. N. Tu

Abstract

The morphology of surface reactions for $Au/SiO_2/Si$ structures has been studied as a function of environment. It was found that the reaction between thin gold film dots and thermally oxidized Si was strongly influenced by the partial pressure of oxygen. When samples are held at elevated temperatures (above 500°C) in a dynamic vacuum, an apparent decomposition of the oxide film with subsequent migration of Au along the exposed silicon surface was observed. The migration was found to follow the crystallographic directions of the silicon. Reduction of the oxide was dependent on the presence of the Au layer as regions free of Au remained intact. The reaction as a function of time, temperature, SiO_2 thickness and ambient conditions has been studied using optical microscopy as well as electron microprobe, microscopy, and diffraction techniques.

Introduction

An important consideration in the design of metal-oxide-semiconductor (MOS) devices is to choose combinations of materials which will retain their chemical and structural stability during fabrication and throughout operation. Gold is frequently a choice for the metal layer, largely because it is chemically inert and films are easily formed by sputtering or evaporation. However, other factors, such as poor adherence to SiO_2, reactivity with Si and high cost limit its use commercially. Previous investigations[1-3] on the stability of $Au/SiO_2/Si$ structures to heat treatments at temperatures from 800 to 1200°C have dealt with the diffusivity of Au through SiO_2 and with changes in electrical properties which accompany the migration of Au through the film and into the underlying Si. In general, the effects of varying environmental conditions such as the partial pressure of oxygen were not included.

In the course of experimentation on the stability of $Au/SiO_2/Si$ structures with respect to chemical reaction, devitrification, etc., during thermal stressing in various environments, we have observed a catostrophic mode of degradation of the oxide film which occurs in dynamic vacuum. After several hours of annealing at temperatures in the range 500 to 700°C, portions of the oxide in the vicinity of the Au are completely reduced. Concommitantly, Au reacts with the exposed Si and migrates in selective directions over the Si surface. Although this complex phenomena is not understood in terms of a sequence of basic mechanisms, the distinctive morphological changes that occur are readily observable and provide interesting examples of reactions that are unique to surfaces. We present here a qualitative description of these reacted surfaces which have been studied in various stages of development, noting effects of temperature, film thickness and environment using several analytical and microscopy techniques.

Experimental Procedure

Thin films of amorphous SiO_2 were prepared by dry thermal oxidation of silicon wafers (Czocharlski, boron doped, 2 ohm-cm) one inch in diameter with a (100) orientation. Films of Au were deposited through a mask onto oxidized Si wafers and formed as dots 30 mils in diameter spaced 80 mils apart from their centers. Two series of studies were carried out: (1) the thickness of the thermally grown oxide was varied over a range from 200Å to 2000Å and (2) the 500Å Au film dots were also vapor deposited on unoxidized Si wafers as well as fused quartz wafers for purposes of comparison.

Heat treatments were carried out in several environments; air, He, encapsulated vacuum and dynamic vacuum of 2×10^{-6} Torr. A heating cycle of 10°/min was used and this rate was the same for the individual experiments in the 500°C - 700°C temperature ranges. The times for each series of investigations was at intervals of 4, 8, 16, 32 and 36 hours.

On cooling to room temperature the surface morphology was studied. The results were observed using the optical microscope, electron microprobe, transmission electron microscope and diffraction instruments. These techniques made it possible to observe unusual effects on the surface of the $Au/SiO_2/Si$ series of samples. These reactions occurred only in the dynamic vacuum system and were not evident in the case of the other ambient conditions.

Experimental Results and Discussion

An optical micrograph of the surface of a 500Å $Au/800Å\ SiO_2/Si$ sample before and after heating at 700°C for 4 and 16 hours in a dynamic vacuum of 2×10^{-6} Torr can be seen in Figure 1. The as deposited Au appears bright and smooth on an amorphous SiO_2 background. After treatment for only 4 hours, the Au film becomes discontinuous over the oxide surface and in certain places the oxide film is completely reduced. In these areas of exposed Si, Au reacts with Si to form a Au-Si mixture which is apparently liquid at this temperature. The pattern of orthogonal channel segments which cover the exposed Si area suggests that liquid droplets are formed which then migrate across the surface by a "melt-through" process which leaves relatively deep troughs. As time increases, the channel pattern encompasses increasingly larger areas. The higher magnification of Figure 2 allows us to see the channels more clearly. They consist of largely straight line segments which follow the [110] crystallographic directions of Si.

The electron microprobe was used to study the redistribution of chemical species associated with the morphological changes exhibited in Figs. 1 and 2. With this technique we observed the changes in composition which occurred in areas labeled I, II and III in Fig. 3a. In area I, opens have formed in the Au film and the underlying oxide film is partially reduced. The scanning x-ray micrograph in Fig. 3b shows regions where distinct differences in the intensity of the Si Kα signal occur. We

attribute the low intensity areas to attenuation by accumulations of Au and the high intensity regions to areas where Au is missing. This was confirmed by another scanning x-ray micrograph (Fig. 3b) of the same area using Au Mα radiation. Areas of high intensity of the Au Mα signal where Au accumulated correspond to areas where the Si Kα signal is attenuated and vice versa.

The distribution of Au was examined in finer detail using Au Mα radiation to obtain reverse image topographs of areas II and III where little or no oxide remains. Clearer evidence that the migration of Au occurs along the channels or troughs previously discussed can be found in Fig. 4. In these images, which are comparable to back scattering, the Au shows up as bright spots at the ends of the crystallographically oriented pathways. Several Au-Si droplets near the outside of the original vapor deposited dot migrated over surprisingly large distances to the periphery of the exposed Si surface. It is not obvious from these images whether the edge of the opening in the SiO_2 layer receded by virtue of a catalytic effect of the Au-Si droplet on the reduction of SiO_2 or whether the oxide layer was merely a barrier to droplet migration. However, the absence of any reduction of SiO_2/Si in regions of the sample that were free of Au makes us suspect that Au plays an essential role in the reduction process.

In region II, microprobe analysis detected only a trace of oxygen and slightly more was found in region I. We hypothesize that channeling was not so distinctly present in these areas as compared to region III because the relatively large amounts of Au allowed most of the oxide reduction to take place without the necessity of long range droplet migration.

To determine whether or not SiO_2 was necessary for the migration of Au and if thickness plays an important role in this rate, a second series of experiments based on the presence and thickness of SiO_2 was carried out. A bare Si wafer and thermally grown SiO_2 films 200Å, 800Å, and 2000Å, upon which 500Å Au dots had been vapor deposited, were heat treated at 700°C for 32 hours in a vacuum 2×10^{-6} Torr. The results of this treatment is shown in Figure 5.

Where no oxide is present, the Au reacts with the Si beneath it, and no significant migration of Au occurs in the lateral direction. With a relatively thin oxide of 200Å as in Figure 5b, the reduction process is initiated all around the original circumference of the dot. Films of 800Å thickness show a similar effect. At 2000Å thickness, the process is initiated at only a few sites on the circumference. In contrast to the large effect of oxide thickness on the frequency of incidence of reduction sites, the rate at which an open area enlarges is only slightly affected, with openings in thinner oxides progressing a little faster than those in thicker films. We have also observed that with sufficiently long annealing, the receding of the oxide eventually stops, presumably due to depletion of Au.

These effects can be seen more dramatically in the optical micrograph of Figure 6. Here the oxide film is in the form of a taper with zero thickness at the bottom of the wafer increasing to 2000Å at the top. Over this range a 500Å Au stripe was deposited. The Au reacts with the Si as seen in the lower portion of the micrograph, then migrates away from the stripe where the film is thin. The reaction becomes less pronounced with increasing SiO_2 thickness.

The effect of thickness of SiO_2 on the Au induced degradation process indicates that oxide reduction may first initiate by the reaction of pure Au on the underlying film and this process is relatively slow; for example, a significant reaction between a Au film and a fused silicon substrate is not apparent after 16 hours at 700°C in dynamic vacuum (Fig. 7b) whereas extensive reaction occurred for Au/800°A SiO_2/Si and Au/Si given the same treatment. For this reason 2000Å films show fewer places where reduction has initiated since the ability of Au to reach the SiO_2/Si interface in these films may depend on the chance presence of weak or defective areas. For thinner films the reaction is uniform around the circumference of the dot. After this incubation period, Au contacts the exposed Si and reacts to form what is probably a Au-Si eutectic. This eutectic mixture attacks the oxide film by breaking the Si-O bond, disolving the Si and releasing the oxygen to the dynamic vacuum.

In order to examine the possibility of Au-Si formation, transmission electron diffraction and microscopy were used to investigate areas which were devoid of O_2 and showed only Si and Au in the electron microprobe results. Areas were thinned by back jet-etching through the Si wafer with a 9:1 HNO_3:HF solution leaving thin films for transmission studies. Electron diffraction patterns were obtained from these areas. They showed the single crystal (100) pattern of the Si wafer as well as randomly oriented polycrystalline rings (Figure 8). Some of the calculated "d" spacings from these reflections were in agreement with the data for Au and Si. The five extra reflections, which did not belong to either structure, could be indexed as belonging to a face-centered lattice. The miller indices of the observed planes could be assigned all odd or all even numbers. The weakness of the (200) and (222) indices may indicate a modified diamond structure, as the atomic ratios of Au and Si are a little different in the two f.c.c. sub-lattices. The lattice constant was a_o=4.400Å which is larger than that of Au a_o=4.07Å and smaller than that of Si a_o=5.42Å. Observed values for this unknown structure are in good agreement with the data of Yashida and Hirota[4] for an expanded Au lattice of a metastable Au-Si alloy phase near the Au_3Si composition.

A bright field electron micrograph of a selected area diffraction pattern is seen in Figure 8b. When the "d"=2.549(111) reflection was used for image formation a dark field micrograph was obtained (Fig. 8c) which showed small crystallites dispersed in the Au-Si matrix of the film. This sequence clearly identifies the particles which contributed to the extra reflections in the diffraction pattern.

5.

In summary, our work has shown that when $Au/SiO_2/Si$ structures are heated at low temperatures in a dynamic vacuum system the insulating oxide is destroyed. This dissociation of the oxide is dependent on the presence of the Au layer. Areas free of Au are not attacked, and the insulating properties are not destroyed. The migration of Au along Si crystallographic [110] directions can only occur when there is a decomposition of this oxide. Although the mechanism is not clearly understood, it is apparent that a Au-Si mixture in the molten state causes rapid reduction of the amorphous oxide. The Au-Si droplets also react with Si to form a metastable Au-Si phase in a matrix of a Au-Si eutectic.

Acknowledgements

The authors are grate... to Drs. P. Ho and R. Rosenberg for helpful discussions, J. D. Kuptsisffor electron microprobe analysis and J. Kucza and W. Kateley for technical assistance in sample preparation.

References

1. A. Z. Badaiov and V. B. Shuman, Soviet Physics-Semiconductors, Vol. 2 No. 5, 615 (1968).

2. D. R. Collins, D. K. Schroder, and C. T. Sah, Applied Physics Letters, 8, 12, 323 (1966).

3. S. F. Cagnina and E. H. Snow, J. Electrochem Soc., Solid State Science, 11, 1165, (1967).

4. M. Yoshida and S. Hirota, Japan J. Appl. Physics 11, 917 (1972).

500A Au/800A SiO_2/(100) Si

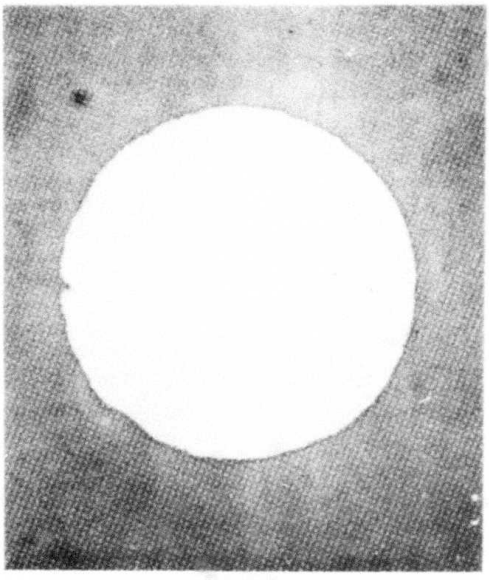

AS DEPOSITED x 48

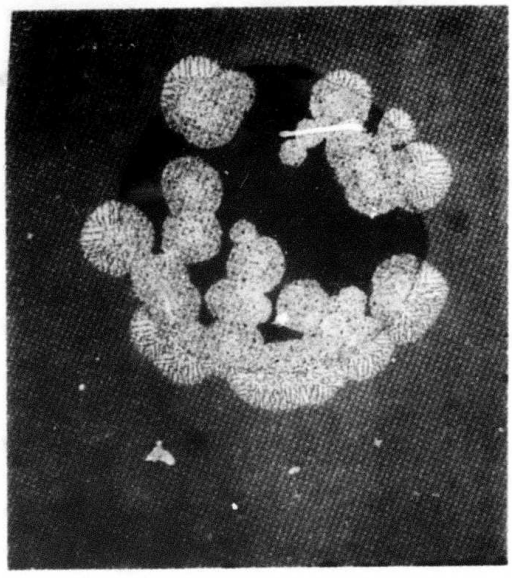

700°C 2×10^{-6} 4 hrs

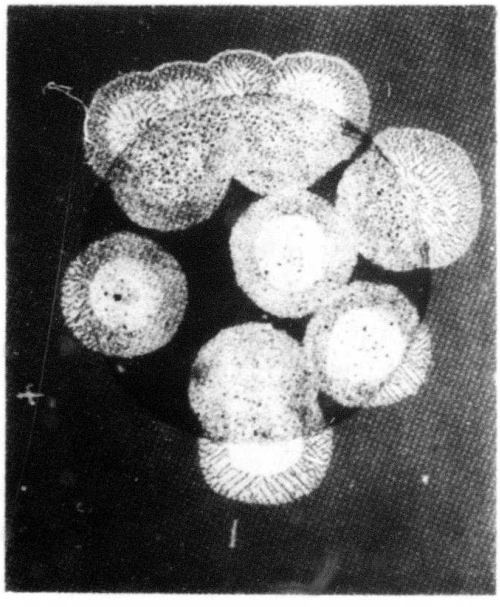

Treated 700°C 16 hrs 2×10^{-6} Torr

Optical Micrograph

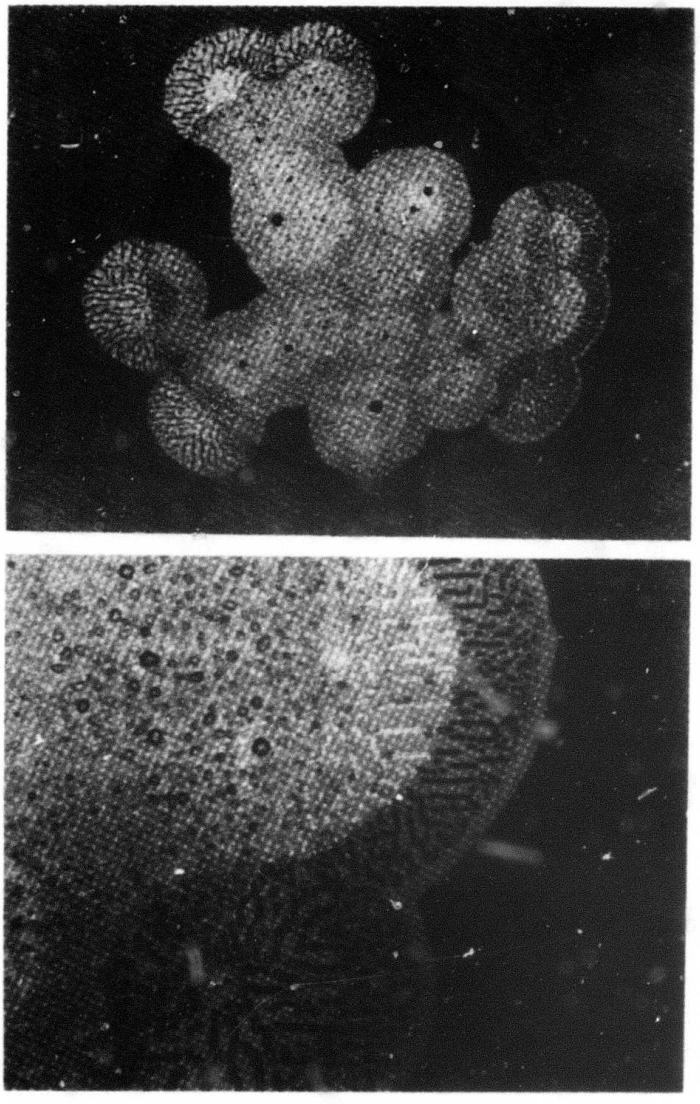

500A Au/800A SiO_2/(100)Si

700°C 2 x 10^{-6} Torr 8 hrs

500A Au/800A SiO_2/(100)Si

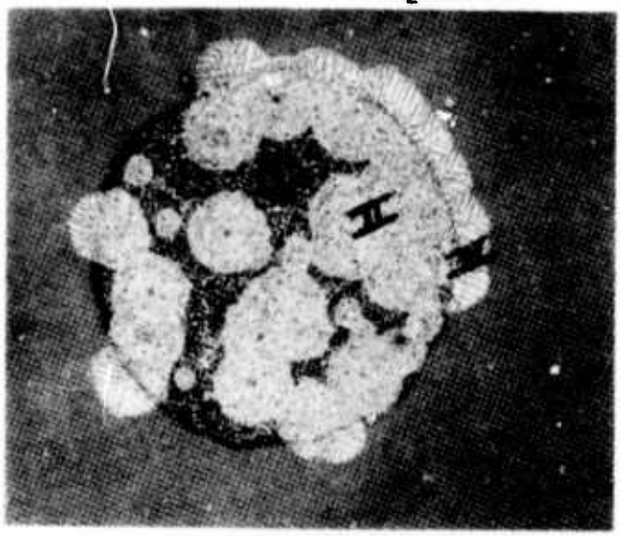

a. Optical Micrograph

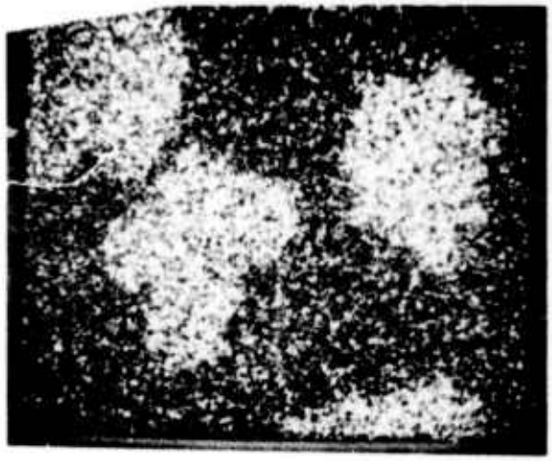

b.

Microprobe Scanning X-Ray Micrograph c.

Electron Microprobe

a.

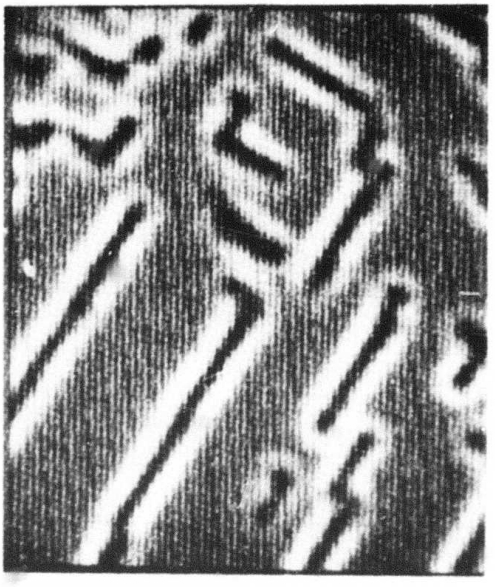

b.

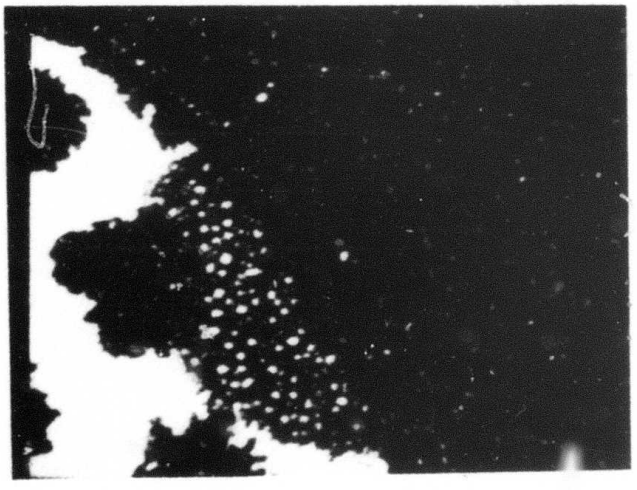

c. SAMPLE CURRENT REVERSE IMAGE

700^0 32 hrs 2×10^{-6}Torr x 48

500 Å Au / Si (100)

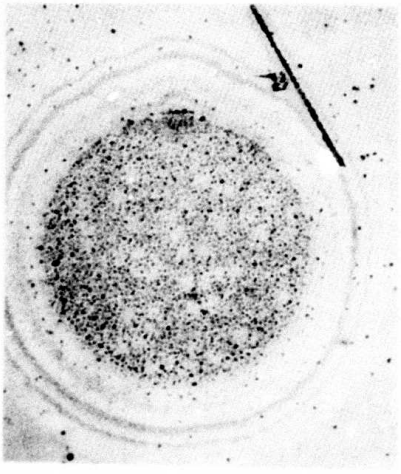

500Å Au/200Å SiO_2/(100)Si

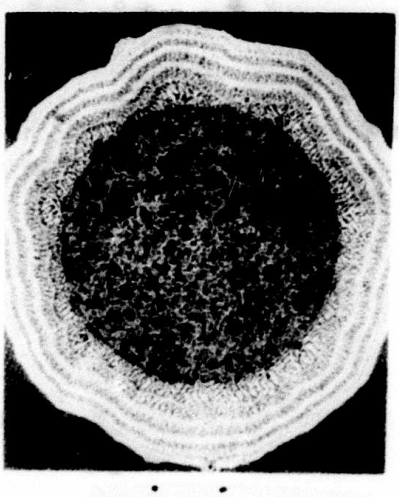

500Å Au/800Å SiO_2/(100)Si

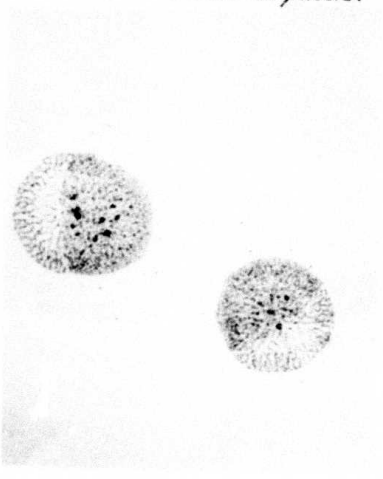

500Å Au/2000Å SiO_2/(100)Si

700°C 16 hrs 2×10^{-6} Torr

Optical Micrograph x 48

Optical Micrograph x 48

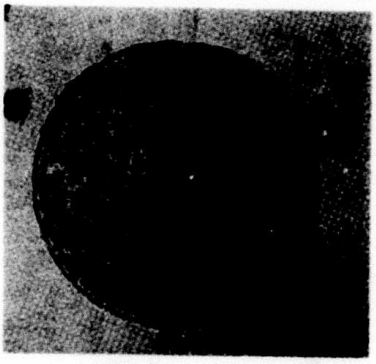

500A Au/(100)Si

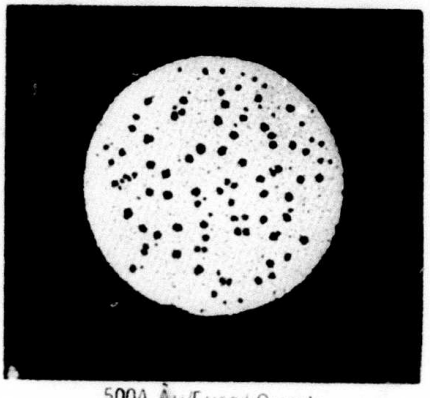

500A Au/Fused Quartz

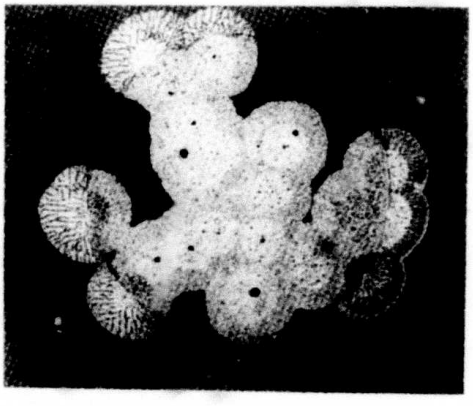

500A Au/800A SiO_2/(100)Si

700°C 16 hrs 2×10^{-6} Torr

500A Au/800A SiO_2/(100) Si

Treated 700°C 16 hrs 2×10^{-6} Torr

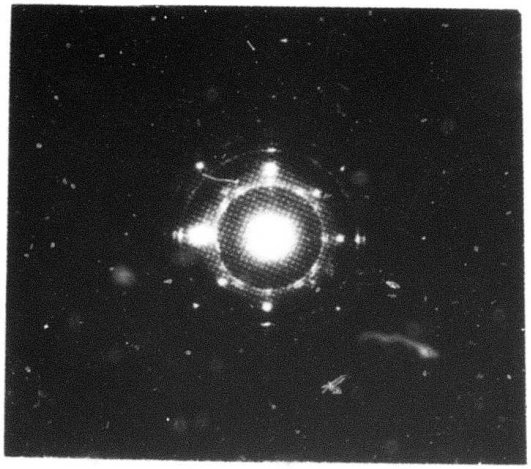

ELECTRON DIFFRACTION PATTERN

a.

BRIGHT FIELD

b.

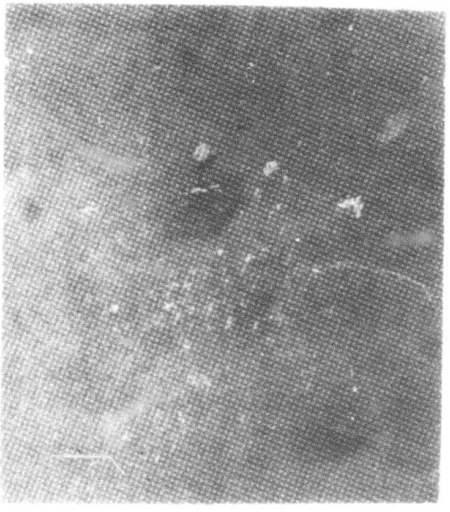

DARK FIELD

c.

ELECTRON MICROGRAPH

B. Ddensification of SiO_2 by Exposure to an Ion Beam

K. N. Tu, J. E. E. Baglin and T. H. DiStefano

INTRODUCTION:

When an ion beam is projected onto a glass surface or onto the surface of a glass coated with a thin metal film, a depression is left on the glass surface. The depression has a size the same as the cross section of the ion beam and has a depth depending on the energy and the dose of the beam and on the thickness of the glass. While the phenomenon of compaction of glass by radiation (electrons, x-rays, neutrons, etc.)[1-3] is known, the ion beam induced compaction is currently of great interest not only because it is associated with the new doping technique of ion implantation but also because the use of high energy ions in the MeV range allows us to separate the compaction process of ionization from atomic collisions. For radiation of lower energies (KeV range) compaction of glass is a combined result of atomic collisions and ionization. Thus, provided that there is an accurate measurement of compaction, the ion beam technique offers a simple experimental verification of theories of compaction of glass by radiation.

In the first part of this study, we have used Talystep with a depth sensitivity of $\pm$ 20 Å to measure the depth of the depression on the glass surface as a function of ion beam energy and dosage, and ion species. The Talystep is a direct measurement of compaction as compared to previous measurements by optical fringes or cantilever plate techniques, and the results have been compared to theory. We found that the amount of compaction does not vary in linear proportion to the total deposited energy but rather obeys a power relationship with the energy ($\sim E^{3/4}$).

In the second part of this study, compaction of thermally grown SiO_2 films of thickness of 1000 to 4000 Å on Si wafers was measured by ellipsometry via changes in density and reflective index. The results show that compaction by ion beams does occur in thin SiO_2 films and leads to a denser form of SiO_2 with a density increase of 1 to 2%. We note that this is the first measurement of densification of thermally grown SiO_2 by radiation. The densified SiO_2 has been found to show an improved dielectric breakdown strength indicating that it is a better intrinsic insulator and also that the number of pin holes has been reduced due to compaction.

EXPERIMENTAL PROCEDURES AND RESULTS

1. Samples

Both bulk and thin film SiO_2 samples have been used in this study for compaction. The bulk samples are 1" in diameter optical quality fused quartz discs with a thickness of 1/16". The thin film samples are obtained by dry oxidation of n-type, (100) orientation Si wafers with a

resistance of 2 ohm-cm. The thickness of the oxide layer is 4000 Å for ellipsometry and is about 200 Å for the dielectric breakdown measurements.

Ion beams of $^4He^+$ and $^{12}C^+$ ions in the MeV energy range have been used for the compaction. We have varied the dosage of the beam from 10^{14} to 10^{17} ions/cm^2. We note that the dosage of 10^{15} ions/cm^2 corresponds to about one monolayer of ions, a relatively small amount of material in relation to the amount of compaction observed. The size of the beam has a cross section of 1x 2 mm^2. All the depressions we made on the bulk samples have the same size which we found to be convenient for Talystep measurements. Since a larger area of depression is required for both ellipsometry and breakdown measurements, we have programmed the ion beam to scan continuously in the x and y directions to produce a compacted area of about 2 x 2 cm^2. Wafers for the breakdown measurement were annealed at 500°C for 1 hour before we put down by evaporation a matrix of 10 x 10 conducting Al thin film pads of 30 mils in diameter spaced 80 mils apart from their centers.

2. Phenomenon of Ion Beam Induced Compaction

Figure 1 shows an optical micrograph of a depression on a fused quartz coated with a 1000 Å Au film. The depression was produced by a 2 MeV $^4He^+$ ion beam of a dosage of 10^{15} ion/cm^2. The metallic film was used to bring out the contrast of the depression and to show that the depression is not caused by sputtering but rather by compaction. For the latter purpose, we deposited a Cr film of 200 Å in thickness onto the fused quartz surface and took nuclear backscattering measurements of the Cr layer before and after the compaction. Since we found no change in the Cr counts, it shows that the depression is not due to sputtering otherwise we should have sputtered away Cr and detected no Cr by backscattering after the compaction.

Since Au films have poor adhesion to glass surfaces, we were able to peel off the Au film and directly measure the depression in the glass surface. Figure 2 shows the Talysurf contours of the Au film surface and the fused quartz surface after we peeled off the Au. The two contors are identical, indicating that the formation of the depression is by the collapse of the glass. The depth was about 1700 Å. Since the penetration range of the ions in the fused quartz is estimated to be 2 to 4 microns, the glass has undergone a volume shrinkage of the order of a few percent.

3. Densification as a Function of Ion Flux.

In Fig. 2, the amount of depression in Å measured by Talystep has been plotted as a function of ion energy from 1 to 3 MeV and of ion dose from 10^{14} to 10^{17} ions/cm^2 for $^4He^+$ ions. Also plotted in the figure for comparison are depressions caused by low doses of $^{12}C^+$ ions at 2.5 MeV. As can be seen, carbon ions are more effective in compacting the glass. There appears a plateau or a saturation in compaction when the ion dose

is over 5×10^{15} ions/cm^2; the plateau increases with the ion energy. At lower doses, however, it is the slope of the curve, or the rate of change of compaction with respect to the dose that increases with the ion energy. Obviously, these curves enable us to select the right dose and energy for a specific compaction, and also to check the theories on compaction of glass by radiation.

According to Brice's energy partitioning calculation,[4] he showed that an implanted ion loses its energy through ionization processes and atomic collisions in the following manner:

$$\varepsilon + \nu = 1$$

where ε and ν are fractions of ion energy dissipated by ionization and by atomic collisions, respectively. Brice and Eernisse[5-6] further showed that ν is typically very small ($\nu < 0.08$) for ions of energy larger than 100 KeV. Thus, for MeV ions, it is reasonable to set $\nu = 0$ and disregard the atomic collisions. Then

$$\Delta V_{total} \simeq \Delta V_{elect.}$$

$$\simeq A \left[\phi E \cdot \frac{d\varepsilon}{dx}\right]^k$$

where ΔV is the specific volume change at depth x; A is a proportional constant; ϕ and E are ion dose and and energy respectively; $d\varepsilon/dx$ is the differential distribution of the fractional energy dissipated in ionization processes, and is found to vary very slowly for $0 \leq x \leq R$; where R is the ion projected range, and falls rapidly to zero for $x>R$; and k is an empirical power constant. The total amount of compaction can be obtained by an integrative assuming $d\varepsilon/dx$ is constant,

$$C = \int_0^R \Delta V dx = A' \left[\phi E\right]^k$$

Thus, if C is plotted vs ϕE on log-log scales, we shall obtain k from the slope of the curve. We found $k = 0.75$ to 0.78. It is worthwhile noting that $k = 1$ would mean simply that the total compaction is proportional to deposited ion energy up to the saturation plateau. Our finding of $k < 1$ may suggest that part of the energy may have been spent in straining the surrounding area of the depression.

4. Ellipsometry Measurement of Densified SiO_2 Films

Compaction of thermally-grown SiO_2 films was measured by ellipsometry instead of Talystep, because the thickness of the films was about 4000 Å and the change in thickness is too small to be determined by Talystep. The energy of the He ion beam was reduced to 50 KeV so

that the ions will not penetrate the oxide and damage the Si substrate or the Si-SiO_2 interface. Typical results of densification of SiO_2 films by 50 KeV $^4He^+$ ions at a dose of 2×10^{16} ions/cm^2 is shown in Table I. For comparison, the Table also contains ellipsometry measurements of thickness and reflection index of the oxide films before the implantation. As can be seen, after the implantation, a density increase of about 1% of the oxide was measured by the change in the film thickness. The reflective index of the oxide film was also found to increase by about 2%.

5. Dielectric Strength of Densified SiO_2

The dielectric strength of radiation densified SiO_2 was measured for the case of very thin films. In this case, the densification was produced by the implantation of low energy He ions into the thin film, with a subsequent annealing treatment to remove the ionized radiation damage. The ions did not sufficiently penetrate the film to produce noticeable damage in the substrate. It was found that the dielectric strength of 200 Å films was increased and the pinhole density was decreased with respect to undensified thin films. The results indicate that the collapse of microvoids caused by the densification increases the dielectric properties of the SiO_2.

The thin film samples were prepared by oxidizing the (100) surface of 2Ω-cm n-type silicon. The thermal oxidation was performed in dry oxygen at 1100°C. Half of each silicon wafer was densified by an implantation dose of 10^{16} He^{++}/cm^2 at an energy of 50 KeV; the unexposed half was used as a control. After implantation, the samples were annealed for one hour in dry H_2 at 450°C. The annealing procedure was required in order to remove the positively charged radiation damage left by the implantation. After annealing, fifty aluminum electrodes, 0.016" in diameter, were evaporated onto each half of the sample. The aluminum electros, 5000 Å thick, were evaporated onto samples initially at room temperature.

The breakdown voltage was measured for electrodes on both the implanted and the control halves of the samples. The breakdown voltage was determined by applying a voltage ramp to the sample and then measuring the voltage at which the current exceeded 10^{-4} A. For this set of measurements, the ramp rate was 0.01 V/Å-sec. Electrodes exhibiting an initial ohmic contact were not considered in the final results. A histogram showing the distribution of breakdown voltage for a typical sample is given in Fig. 4.

The implanted half of the sample has an average breakdown field of 6.7×10^6 V/cm, which is considerably greater than the 5.2×10^6 V/cm of the unimplanted half of the same sample. Also, the tail of the distribution at low fields is greatly reduced by the implantation. One explanation for the reduction of the low field tail is that the implantation reduces the density of "weak spots" in the SiO_2 film. This is

consistent with the theory that part of the densification of the SiO_2 is due to a collapse of micropores in the film; the number of "weak spots" resulting from micropores would then be expected to decrease with an increasing density of the SiO_2. In summary, densification of thin SiO_2 film increases the dielectric properties of the film in two ways: a decrease in the "weak spot" density and an increase in the average dielectric strength.

TABLE I

DENSIFICATION OF THERMALLY-GROWN SiO_2

	Wafer#	Thickness of SiO_2	Index of Reflection	Difference in Thickness after Implantation
Before	4	3,820	1.464	
Implantation	5	3,749	1.465	
After	4	3,779	1.4907	-41
Implantation	5	3,712	1.4901	-37

Implantation = 50 KeV Helium, 2×10^{16} ions/cm^2.

References

1. W. Primak and R. Kampwirth, J. Appl. Phys. 39, 5651 (1968)
2. W. Primak, J. Appl. Phys. 43 2745 (1972).
3. R. Brückner, J. Non-Cryst. Solids 5, 177 (1971).
4. D. K. Brice, Rad. Effects, 6, 77 (1970).
5. D. K. Brice, Phys. Rev. A6, 1791 (1972).
6. E. P. EerNisse, J. Appl. Phys. 45, 167 (1974).

Fig. 1: Optical micrograph of a depression of size 1 mm x 2 mm on a fused quartz surface coated with a 1000 Å film.

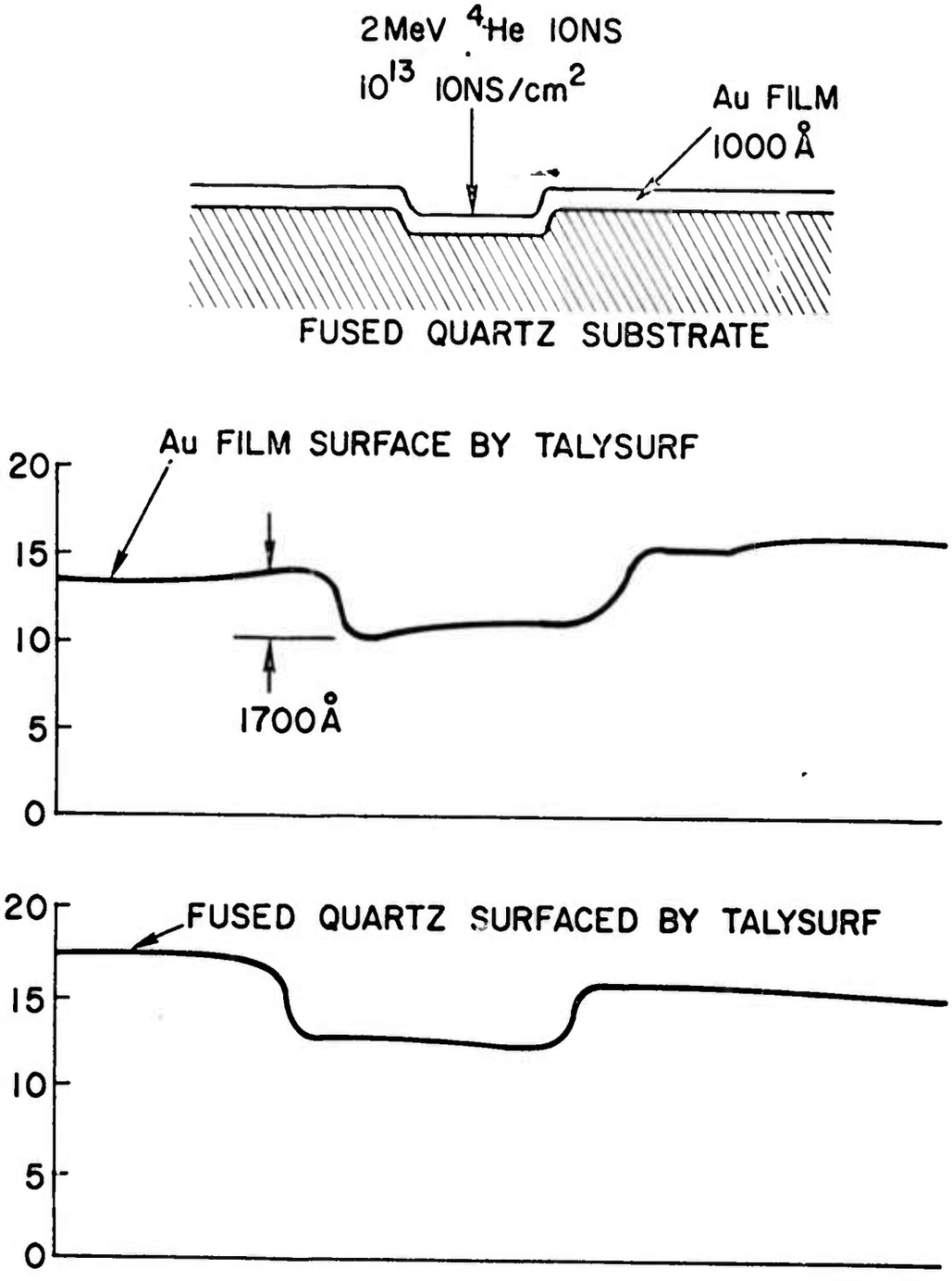

Fig. 2: Talysurf contours of the Au film surface and the fused quartz surface after the peeling of the Au film.

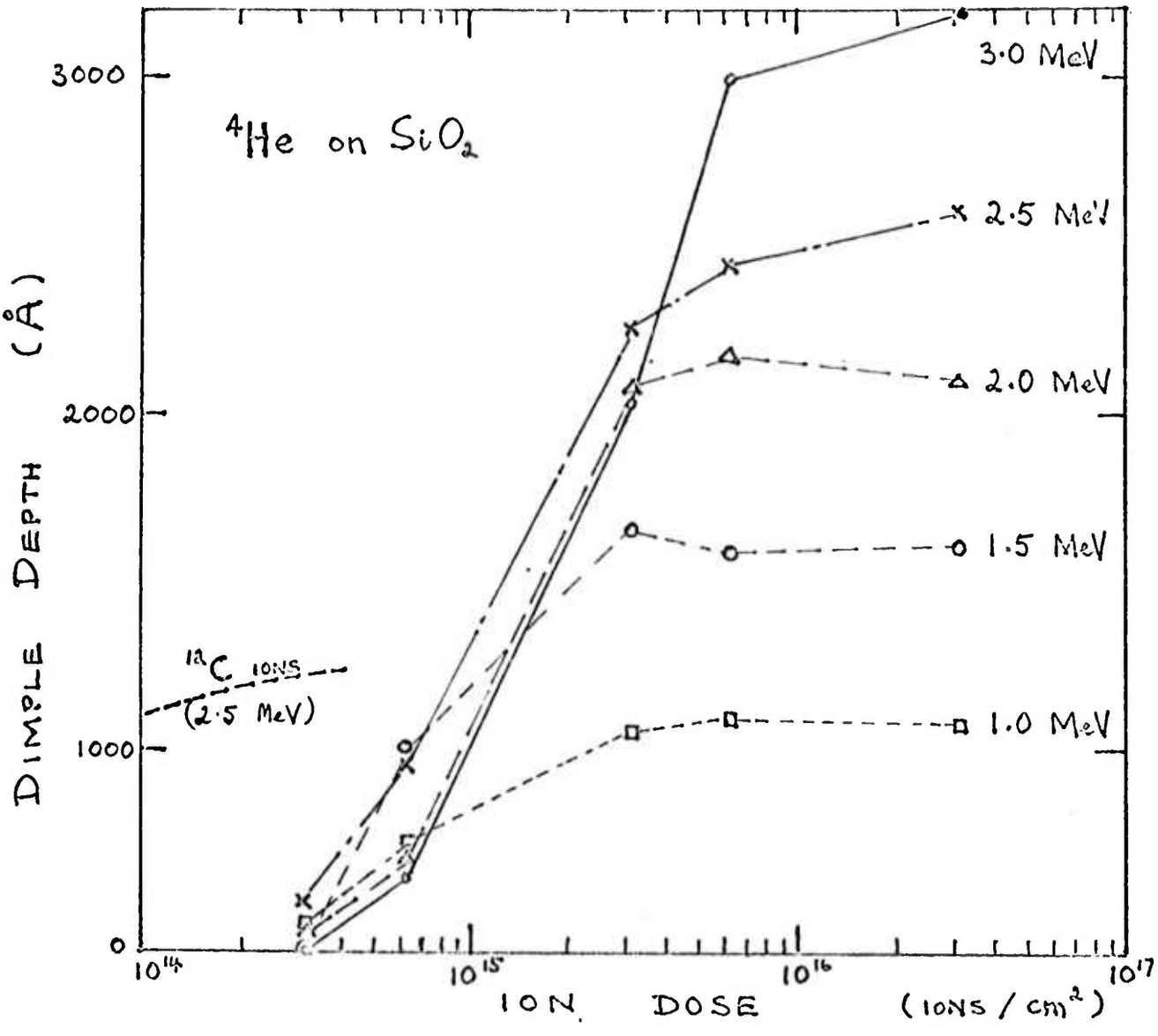

Fig. 3: Talystep measurement of depression depth vs ion dose and ion energy

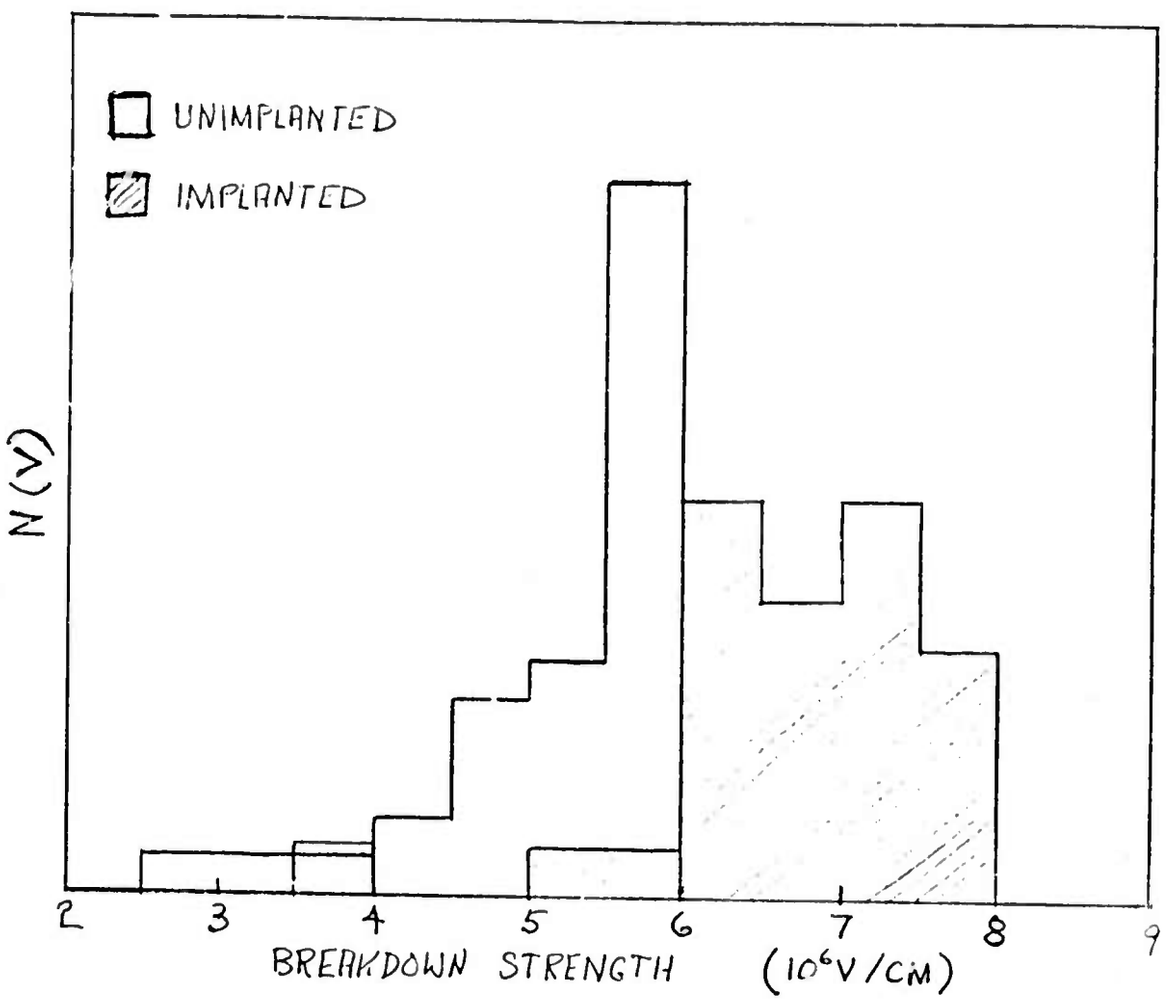

Fig. 4: Histogram of the distribution of breakdown voltage of an implanted and an unimplanted SiO_2 film sample.

C. EPITAXIAL GROWTH OF NICKEL SILICIDE $NiSi_2$ ON SILICON

by

K. N. Tu and E. I. Alessandrini
IBM Watson Research Center
Yorktown Heights, New York 10598

W. K. Chu, H. Kraütle and J. W. Mayer
California Institute of Technology
Pasadena, California 91109

ABSTRACT: The formation of structures of nickel silicides on Si have been studied by use of glancing-angle x-ray diffraction, MeV He^+ backscattering, reflection electron diffraction and replica electron microscopy. By reacting evaporated Ni films with Si wafers in the temperature range of 200 to 800°C, we have found three Ni silicides. The phase Ni_2Si starts to form at 200°C at the Si-Ni interface. Around 350°C, the phase NiSi grows from the Si-Ni_2Si interface. The NiSi is stable in the temperature range of 350 to 750°C and above that it transforms abruptly to $NiSi_2$. The disilicide grows epitaxially on (111), (110) and (100) surfaces of Si.

1.

Introduction

Metal silicides on silicon are commonly formed by direct reaction between evaporated metals and silicon. The formation temperature is about 1/3 to 1/2 of the melting point of the silicide.[1] Low melting point silicides, e.g. PtSi[2] and Pd_2Si,[3-4] which can be formed within the temperature limit of device fabrication have been widely studied. The use of these silicides as Ohmic contacts and Schottky barriers[5] on silicon devices requires that the silicide must have a uniform interface with the silicon and should be thermodynamically stable. Ideally a uniform interface in atomic scale could be obtained if we had an epitaxial layer of silicide on silicon.

The only silicide investigated to date that grows epitaxially on silicon is Pd_2Si on (111) Si.[6] The epitaxial nature of this silicide was studied by electron diffraction[4,5] and MeV - ^4He ion channeling techniques.[3] However, Pd_2Si which has a hexagonal structure does not grow epitaxially on crystallographic surfaces of silicon. For example, polycrystalline layers were formed on <100> oriented silicon.[5,6]

It was found that polycrystalline layers of Pd_2Si transform into PdSi at temperatures around 750°C while epitaxial layers transform at higher temperatures. This suggests that epitaxial silicides may have better stability than polycrystalline layers.

In this paper we report our investigations of silicide formation in the Ni - Si system. This system has six silicides, the Si rich phase, $NiSi_2$ has a low melting point ($T_m \simeq 990$°C.[7] This suggests that silicide formation would also occur at low temperatures.[7] The

phase $NiSi_2$ has a cubic structure the same as CaF_2 and a lattice parameter of 5.406 Å which we note is in excellent match to that of silicon (5.4282 Å). Thus we expect $NiSi_2$ to grow epitaxially on Si.

Experimental

We have used electron-beam evaporation to deposit Ni films on (111), (110) and (100) oriented Si wafers. Before deposition, the wafers were cleaned ultrasonically in detergents, rinsed in deionized water and ethyl alcohol and dried by Freon. The thickness of the Ni films ranged between 600 and 2000 Å. Annealing of these films in the temperature range of 200 to 800°C was carried out either in a vacuum of 2×10^{-6} Torr or in high purity He gas ambient. The control of the temperature was around $\pm$ 1°C.

After annealing, the samples were examined by MeV He ion backscattering, Seemann-Bohlin x-ray diffraction, reflection electron diffraction, and replica electron microscopy. The ion backscattering technique was used to detect the transition of one phase into another and the rate of transition.[8] Also this technique was used to find out the epitaxial relationship between the silicide and the silicon by use of channeling measurements.[3] The epitaxial relationship was confirmed by reflection electron diffraction. X-ray diffraction was used to identify phases in teh silicide layer and to obtain structural information.[9] Changes of surface topography were observed with replica electron microscopy.

3.

Results and Discussions

(1) Ni Films as Deposited

The structure of the Ni films as deposited was examined by x-ray diffraction. A nickel powder sample of grain size of 5 microns was used as a standard for analyzing the strain, grain size and preferred orientation of the film samples. The evaporated films were found to have a lattice parameter of 3.5316 Å $\pm$ 0.0006 Å and a grain size of 160 to 210 Å. The films were under tension with a tensile strain of 0.2% along the direction parallel to the film surface. Grains in the film randomly oriented as indicated by ratios of their integrated peak intensities. Replica micrographs showed the surface of the films was very smooth, no hillocks or holes, and the grain size measured directly from the micrographs was comparable to the x-ray result.

(2) Formation of Ni_2Si and NiSi

Ni Films start to react with the Si substrate forming Ni_2Si at the interface of Ni and Si at temperatures as low as 200°C. At low temperatures, the react ion rate is slow; e.g., after annealing for 48 hours at 200°C approximately 240 Å Ni are consumed. At 300°C and above, the reaction rate becomes appreciable. For 20 minutes at 350°C, a Ni film of 2000 Å thick will totally react with Si forming a uniform Ni_2Si layer.

Further anneal treatment will transform Ni_2Si into the phase NiSi. The reaction product is located at the interface of Si and $NiSi_2$. The formation of NiSi is very fast and the phase is stable up to 750°C.

Figure 1 shows 2 MeV $^4He^+$ backscattering spectra from a 2000 Å Ni

film on Si for the as-deposited case, for 20 minutes at 350°C and for two hours at 400°C. Composition ratio of Ni to Si in the product layer can be calculated from the spectra height ratio.[8] From the spectra in Fig. 1, the Ni to Si composition ratio is 2 to 1 for the 350°C anneal and 1 to 1 for the 400°C anneal.

Backscattering can only give the composition ratio of the silicide layer. Positive identification of Ni_2Si and NiSi are varified by Seeman-Bohlin x-ray diffraction.[9] Figure 2a and 2b show the x-ray diffraction patterns of samples annealed at 250°C for 24 hours and at 400°C for 2 hours. The patterns were obtained by scanning the sample at steps of 0.15° (40) increment and with a counting time of 60 sec/step. The peaks have been indexed as reflections of Ni and Ni_2Si for Fig. 2a and NiSi for Fig. 2b. Since there is no ASTM diffraction cards for both Ni_2Si and NiSi, their reflections were indexed as the same as those of $PbCl_2$ and MnP, respectively. This is because the phase Ni_2Si has an orthorhombic structure the same as that of $PbCl_2$, and NiSi the same as MnP. The lattice parameter of Ni_2Si were taken approximately to be a = 3.75 Å, b = 5 Å, and c = 7.04 Å, and NiSi to be a = 5.62 Å, b = 5.18 Å, and c = 3.34 Å.[7]

(3) Formation of Epitaxial $NiSi_2$

By reacting evaporated Ni films with Si at temperature higher than 750°C we found the epitaxial growth of $NiSi_2$ on Si. We note that the disilicide is the phase most rich in silicon. Structure of the disilicide, its composition ratio and the epitaxial relationship have even studied by backscattering and by reflection electron diffraction.

Figure 3 shows 2.0 MeV $^4He^+$ ion backscattering spectra of a 650 Å Ni film on Si before and after heat treatment. Formation of $NiSi_2$ is observed. The composition ratio of Ni to Si was found to be 1 to 2. The uniformity of the layer is poor as indicated by the lack of sharpness of the trailing edge of the Ni portion of the spectrum for the reacted layer.

The epitaxial nature of a film can be studied by backscattering along a channeled direction.(3) Channeling of $^4He^+$ ions at 2.0 MeV and 0.7 MeV were made for several samples annealed at 800°C or above. The substrates were Si of (111), (110) and (100) orientation. Epitaxial $NiSi_2$ layers have been observed in all cases. Figure 4 shows spectra of 0.7 MeV $^4He^+$ backscattered from a thick NiSi layer. This layer is formed by annealing a 3500 Å film on (100) Si at 800°C for 2 hours.

The aligned spectrum has a height about 30% of the randomed spectrum at the minimum yield of the $NiSi_2$ spectrum. For 2 MeV $^4He^+$ ion channeling on the same sample. The minimum yield is 50%. The data indicate(10) that about 70% of the silicide crystallites are aligned within 1 to 2° of the substrate crystallographic axis and that there is some spread in orientation.

(4) Reflection Electron Diffraction and Replica Electron Micrograph Study of the Silicides.

In addition to the channeling study, the epitaxial nature of the $NiSi_2$ films are reflection electron diffraction patterns. Figure 5(a) shows the indexed single crystal pattern for $NiSi_2$ epitaxial layer on (100) surface of Si diffracted along [110] direction.

6.

The epitaxial relationship, (100) [110] $NiSi_2$//(100) [110] Si, between the disilicide and the Si substrate was established by comparing the reflection electron diffraction pattern of the disilicide to that of the back side of the Si substrate taken along the same direction. The crystallographic orientation of the Si was first established with a x-ray lane picture. The epitaxial growth of the disilicide on Si can be expected since the phase $NiSi_2$ has the cubic CaF_2 structure with A_o = 5.406 Å and has 4 Ni atoms at 000; F. C. and 8 Si atoms at $\pm$ (1/4, 1/4, 1/4); F. C. This presents a good match with the diamond structure of Si with a_o = 5.4282 Å and 8 atoms at 000; 1/4, 1/4, 1/4; F. C. The lattice mismatch in this case is less than 0.5% of registry. In addition to the arrays of spots, there is a set of semi-circular rings in Fig. 5a. The "d" spacings determined from these rings were found to be those of the disilicide. Thus, besides the epitaxial layer, there were some randomly oriented polycrystals of $NiSi_2$ in the sample. This is in agreement with the channeling results shown in the last section.

Figure 5b is also a diffraction pattern of $NiSi_2$ except this epitaxial layer is on (111) surface of Si diffracted along its [211] direction. The set of rings in Fig. 5b was found to be those of NiSi. Thus, it indicates that the NiSi to $NiSi_2$ transformation was not complete in this sample. Figure 5c shows the reflection electron diffraction pattern of a polycrystalline NiSi on (111) surface of Si. There are rings and no spots. The rings can be indexed as thos of NiSi having a MnP type structure.

Replica electron micrograph of the epitaxial $NiSi_2$ layer on (100) Si wafer is given in Fig. 6. A latex plastic sphere of 5000 Å in diameter is used as a dimension calibration. The growth step follows the <110> directions of a cubic plane. The surface is not uniform in agreement with the backscattering spectrum given in Fig. 3.

Summary

The formation of nickel silicides has two distinctive features:

1) the phases Ni_2Si, NiSi, and Ni_2Si are formed at progressively higher anneal temperature. This represents the first observation of the formation of three phases in a thin film silicide system.

2) The disilicide, $NiSi_2$ grows epitaxially on (111), (110), and (100) Si. This undoubtedly reflects the close match incrystal structure and lattice spacing between the disilicide and underlying crystal substrate.

Other aspects of the silicide growth follow the general pattern found[1] in other silicides.

1) The formation temperature (200°C) of the first phase Ni_2Si is $\approx$ 1/3 the melting point (1318°C) in °K. Silicide formation in general is found between 1/2 and 1/2 of the melting point.

2) Similar to Pd and Pt silicides, a metal rich silicide forms first for Ni on Si. It should be noted, however, that the disilicide is usually formed first for other metals.

Acknowledgements

This work was supported at IBM Watson Research Center in part by ARPA Contract No. F19628-73-C-0006 administered by AFCRL, and at Caltech

by the Air Force Cambridge Research Center. We also are grateful to T. J. Dempsey at IBM for film preparation, K. Asai at IBM for assistance in x-ray diffraction, C. F. Aliotta at IBM for taking the replica micrograph and J. F. Ziegler at IBM for providing the (110) Si substrates.

9.

References

1. J. W. Mayer and K. N. Tu, J. Vac. Sci and Tech. (to be published).

2. H. Muta and D. Shinoda, J. Appl. Phys. 43, 2913 (1973).

3. R. W. Bower, R. E. Scott and D. Sigurd, Solid State Elect. (to be published).

4. G. A. Hutchins and A. Shepala, Thin Solid Films (to be published).

5. K. E. Sundström, S. Petersson, P.-A. Tove, Uppsala University Report, UPTEC F3-29R (to be published).

6. W. D. Buckley and S. C. Moss, Solid State Elect. 15, 1331 (1972).

7. M. Hansen, "Constitution of Binary Alloys" (McGraw-Hill, New York, 1958).

8. W. K. Chu, J. W. Mayer, M.-A. Nicolet, T. M. Buck, G. Ainsel and F. H. Eisen, Thin Solid Films 17, 1 (1973).

9. K. N. Tu and B. S. Berry, J. Appl. Phys. 43, 3283 (1972).

10. D. Sigurd, W. Van der Weg, R. Bower, and J. W. Mayer, Thin Solid Films (to be published).

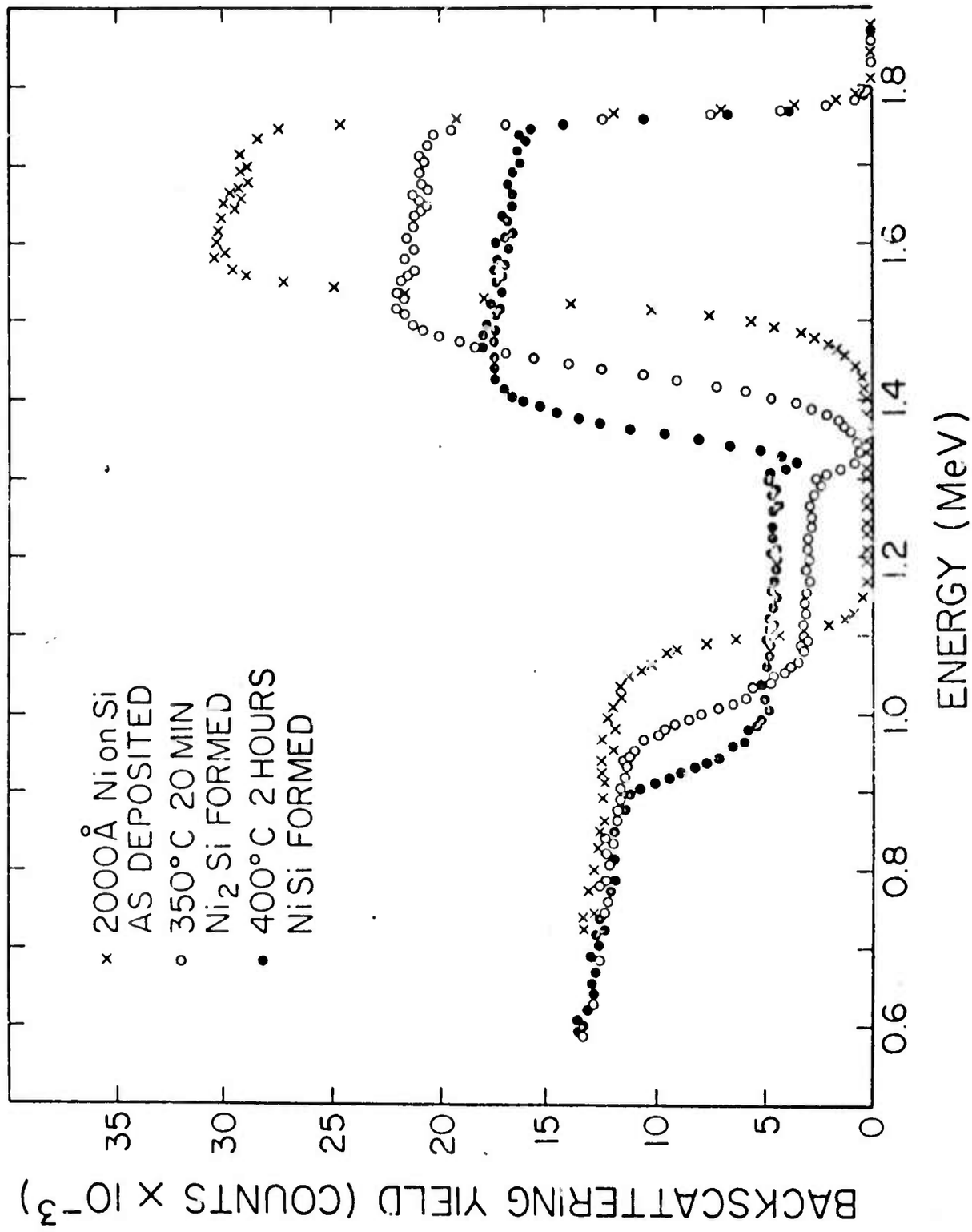

Figure 1: Energy spectra of 2 MeV $^4He^+$ ions backscattered from 2000 Å Ni on Si as deposited (x). Ni_2Si forms after annealing at 350°C for 20 minutes (0). NiSi forms after annealing at 400°C for 2 hours (0).

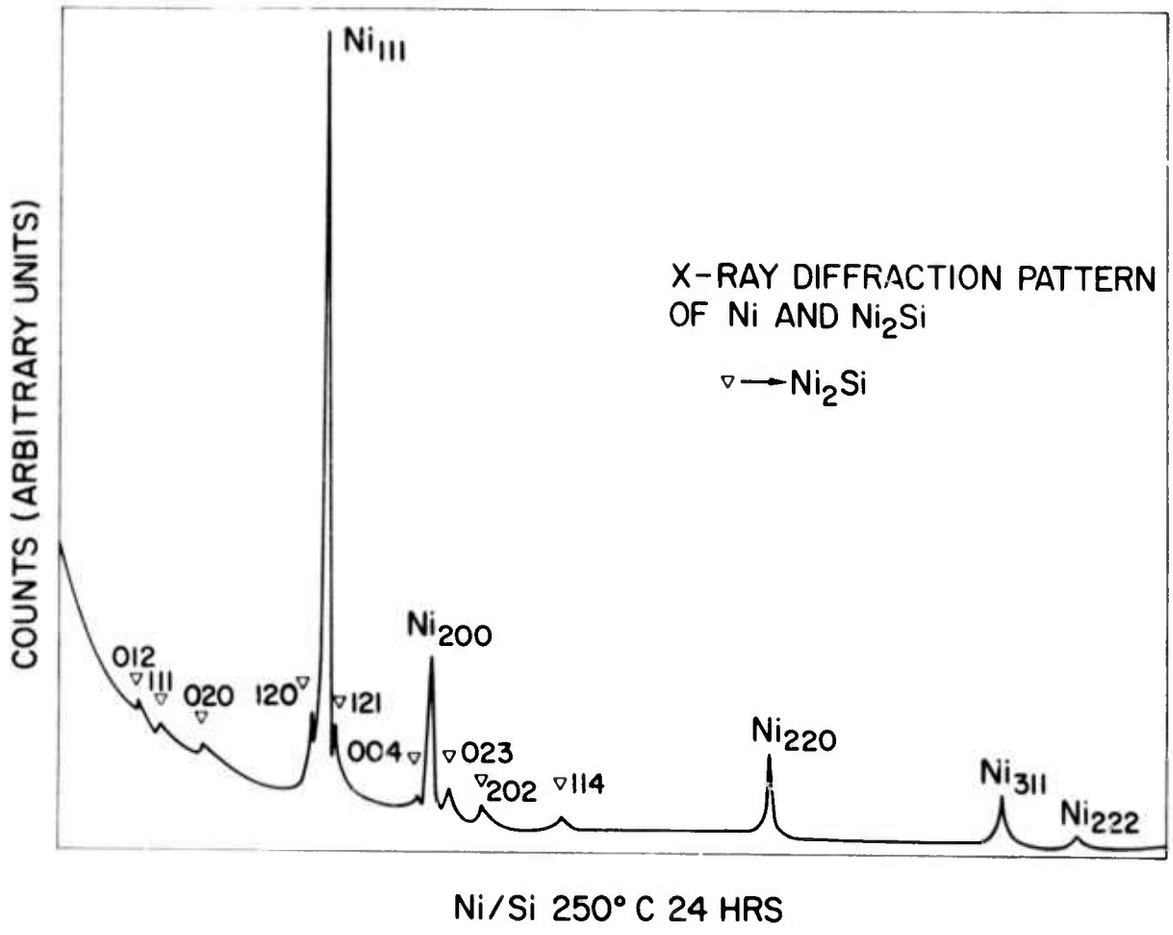

Figure 2: (a) X-ray diffraction pattern of a sample of 3500 Å Ni on Si that has been heat treated at 250°C for 24 hours. Reflections of Ni and Ni_2Si have been indexed.

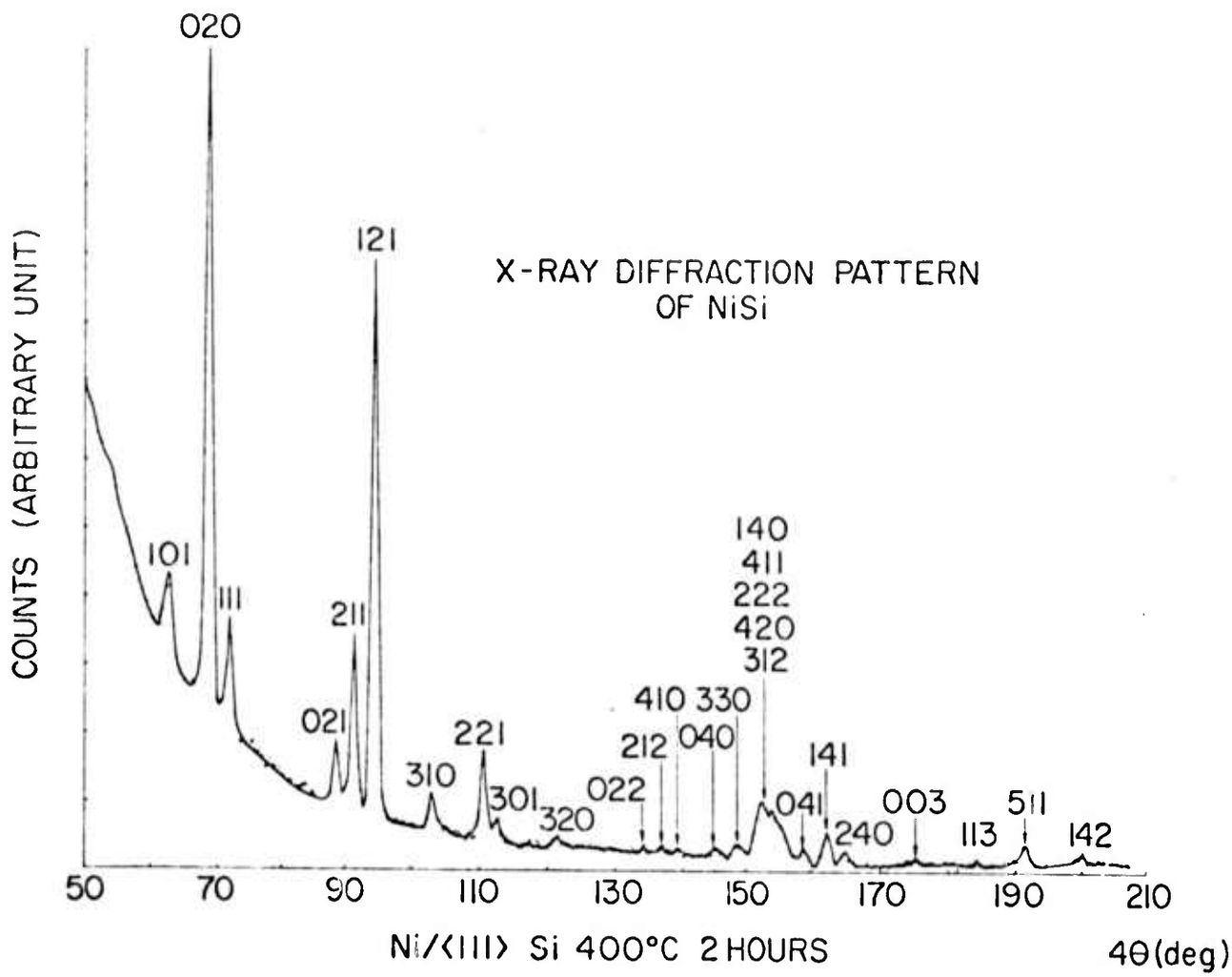

(b) X-ray diffraction pattern of NiSi phase formed by reacting 3500 Å Ni film on Si at 400°C for 2 hours.

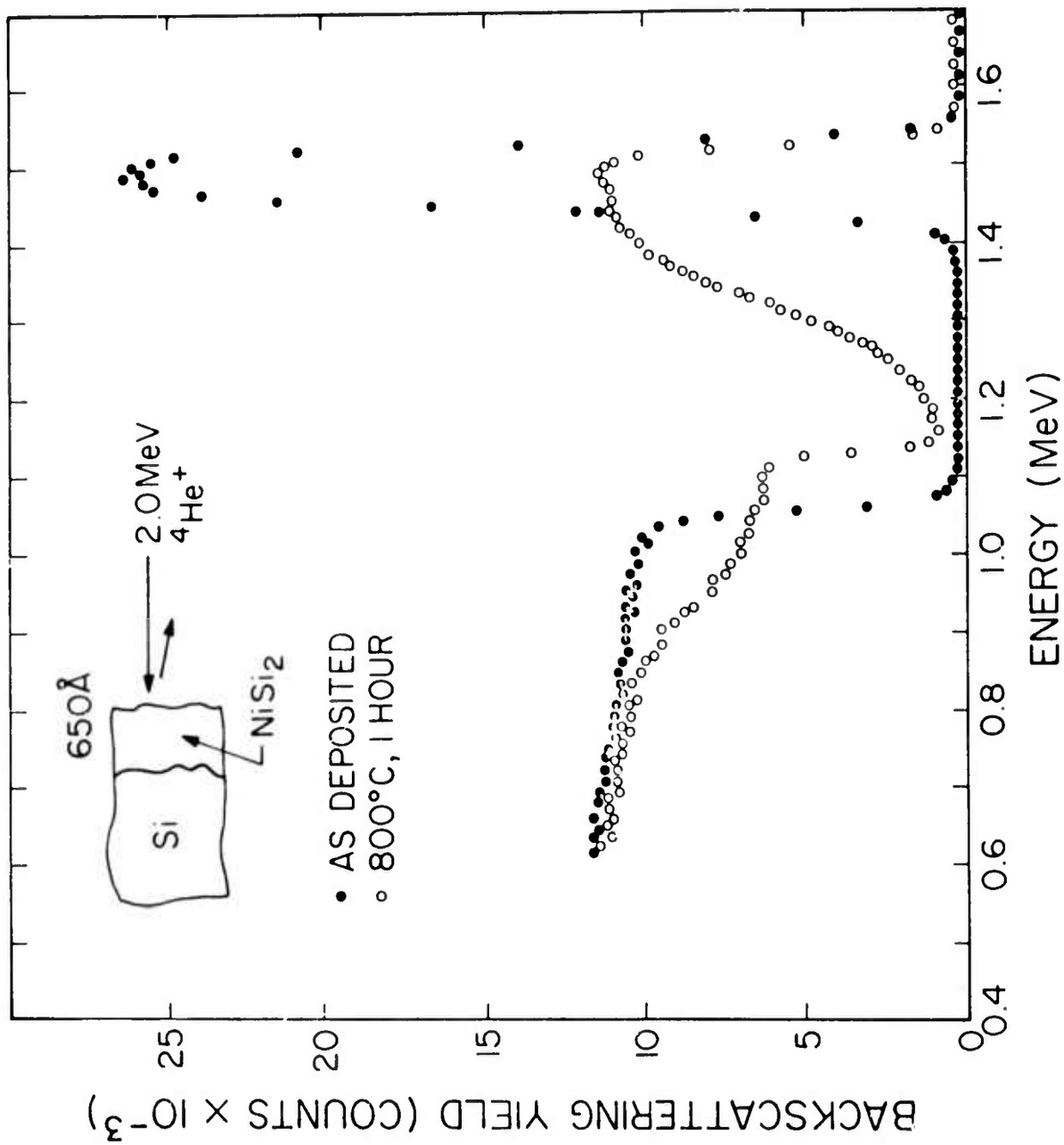

Figure 3: Energy spectra of 2 MeV $^4He^+$ ions backscattered from 650 Å Ni on Si as deposited (0). Nonuniform but epitaxial $NiSi_2$ forms after annealing at 800°C for 1 hour.

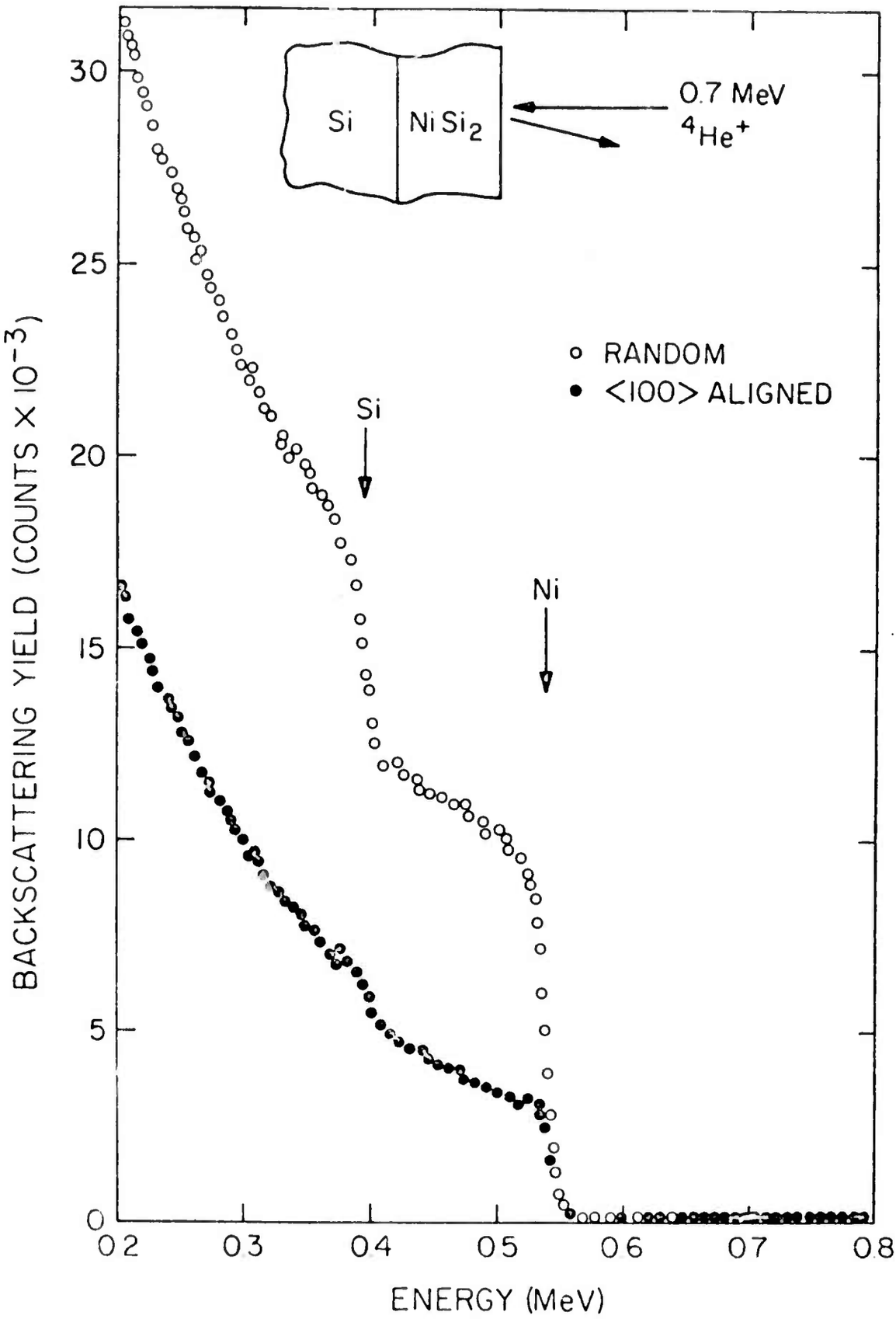

Figure 4: Energy spectra of 0.7 MeV $^4He^+$ backscattered from a thick $NiSi_2$ epitaxial layer on Si: Random spectrum (0) and channeled spectrum along <100> direction.

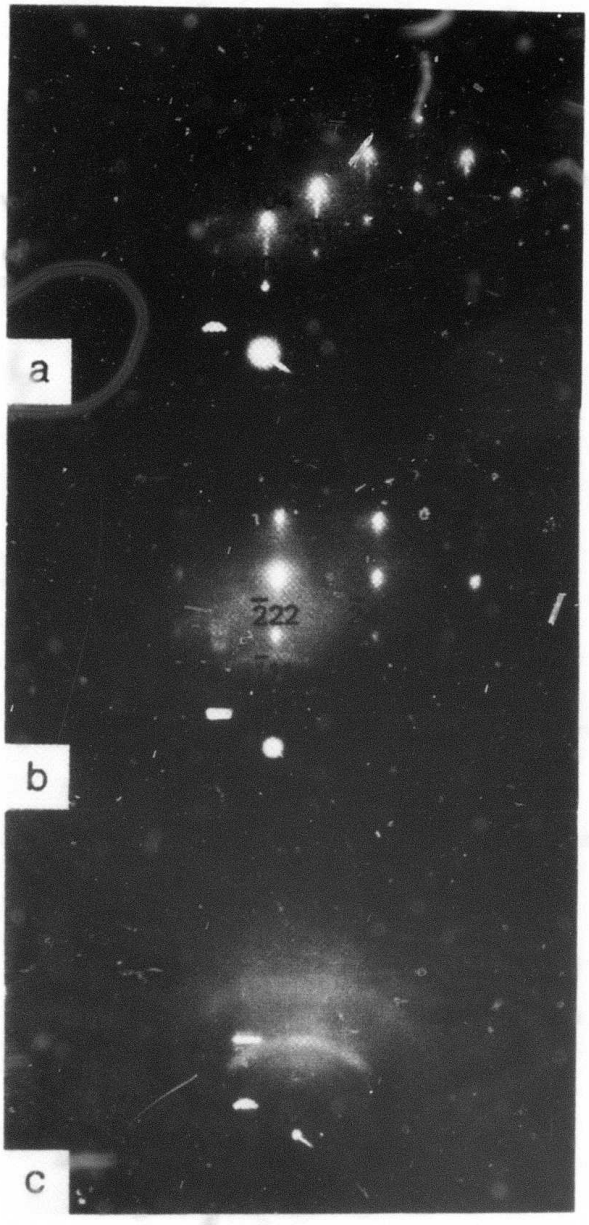

Figure 5: Reflection electron diffraction patterns of nickel silicides on single crystal silicon substrates of different orientations.

(a) Epitaxially grown $NiSi_2$ on (100) Si with (100) [110] $NiSi_2$//(100) [110] Si. The diffraction pattern was taken along the [1$\bar{1}$02 direction. Note the forbidden diffraction of 002. The rings have been identified to be polycrystalline $NiSi_2$.

(b) Epitaxially grown $NiSi_2$ on (111) Si with (111) [211] NiSi//(111) [211] Si. The diffraction pattern was taken along the [$\bar{2}$11] direction. Note the forbidden diffractions of $\bar{2}22$ and $\bar{2}40$. The rings have been identified to be polycrystalline NiSi.

(c) Polycrystalline NiSi grown on (111) Si.

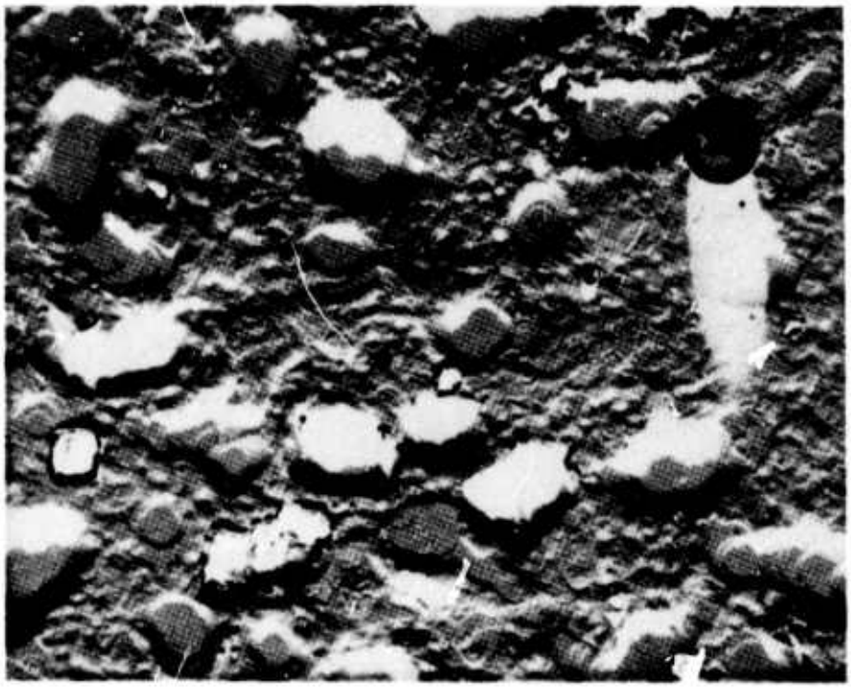

Figure 6: Replica electron micrograph of the epitaxially-grown $NiSi_2$ on (100) Si substrate. The growth step can be seen to follow the <110> major directions of a cubic plane. The latex plastic sphere has a diameter of 5000 Å.